

이학박사학위논문

유기 단분자 및 탄소 양자점에 기반한 유기 반도체의 에너지 수확에 대한 연구

**Energy Harvesting of Organic
Semiconductors Based on Push-Pull Type
Small Molecules and Carbon Dots**

2018 년 8 월

서울대학교 대학원

화학부 유기화학 전공

임 홍 철

유기 단분자 및 탄소 양자점에 기반한 유기 반도체의 에너지 수확에
대한 연구

**Energy Harvesting of Organic Semiconductors Based on
Push-Pull Type Small Molecules and Carbon Dots**

지도교수 홍종인

이 논문을 이학박사학위 논문으로 제출함.

2018년 06월

서울대학교 대학원 화학부

유기화학전공

임홍철

임홍철의 이학박사 학위논문을 인준함.

2018년 06월

위원장 최태립 (인)

부위원장 홍종인 (인)

위원 서정쌍 (인)

위원 손병혁 (인)

위원 신익수 (인)

Abstract

Energy Harvesting of Organic Semiconductors Based on Push-Pull Type Small Molecules and Carbon Dots

Hong Chul LIM

Major in Organic Chemistry

Department of Chemistry

Graduate School

Seoul National University

Organic semiconductors have received great attention in the past decades due to their flexible structure, low processing cost and unique physical properties. The organic semiconductors have been used for (opto)electronics such as organic photovoltaic devices (OPVs), organic photodetectors (OPDs), organic light-emitting diodes (OLEDs), electrochromic devices (ECDs) and secondary ion battery, *etc.* In particular, π -conjugated small organic molecules have attracted

considerable attention in relation to energy harvesting because there has been growing interest in an alternative energy harvesting system due to environmental consequences of global warming and the energy crisis. Furthermore, their photophysical and electrical properties can be controlled through the change of the molecular structure. In this thesis, we report on various methods to improve the efficiency of organic photovoltaics such as OPVs and OPDs based on the characteristics of push-pull-structure organic small molecules and nanocomposites. The (carbon-dots) M_x^+ as a new type of the supporting electrolyte is also described for energy harvesting of ECDs.

Part I provides a brief overview of organic semiconductors and organic photovoltaics. Electronic transitions associated with light absorption and emission and mechanisms for the generation and transport of excitons (carriers) are described. It also provides a brief history of development of OPVs and OPDs, push-pull organic small molecules, and device architectures along with working principles of organic photovoltaics.

Part II deals with the development of high performance organic photovoltaics using push-pull small molecules and hybrid materials such as carbon dot@PEDOT:PSS and colloidal quantum dot-silica composites.

The section I describes the effect of the π -linker on electrochemical, thermal and morphological properties of push-pull type D- π -A molecules (**3T** and **DTT**) as donor materials of the photoactive layer, and on the performance of OPV devices. **3T** with a terthiophene π -linker showed high electrochemical stability with a faster electrode reaction rate. The solution-processed bulk heterojunction (BHJ) OPV devices based on **3T**:PC₇₁BM active layer showed higher PCE values than **DTT**-based devices because of **3T**'s superior electrochemical properties. It appears that

the elaborate design of the π -linker is required for the development of high performance D- π -A structure-based OPV devices.

The section II presents a study on three push-pull-structure small molecules as OPD donor materials and the performance of OPD devices. It turned out that the π -linker structure of the small molecules affected the photophysical, thermal and morphological properties. **H3** with a short π -linker showed weaker intermolecular interactions and lower π - π packing density than other donor molecules. OPD devices based on **H3** exhibited high sensitivity and broadband EQE in both planar heterojunction (PHJ) OPDs and BHJ OPDs. Our results suggest that the π -linker structure of push-pull D- π -A molecules could affect the crystallinity of thin films, and the photoactive layer with amorphous-like domains could lead to high performance OPD devices compared to that with polycrystalline domains. These results provide a strategy for effective donor molecule design as well as for reducing the dark current density (J_d) to achieve high performance OPD devices.

The section III introduces a photocrosslinkable oligothiophene as a hole transport layer (HTL) in OPV devices. The oligothiophene (**5T-p**) consists of diacetylene as a photocrosslinker and quinquethiophene as a π -conjugated backbone. The **5T-p** thin films prepared by spin-casting were photopolymerized through irradiation of 254 nm UV hand lamp. Thin film characterization revealed that the intermolecular packing network in thin films significantly influenced the performance of OPV devices.

The section IV describes the self-assembly of poly(3,4-ethylene dioxythiophene):poly(styrenesulfonate) (PEDOT:PSS) organogel films incorporating carbon dots and their application to OPVs as a hole extraction layer (HEL). The carbon dots act as a physical linker among PEDOT chains through

electrostatic interactions, resulting in the formation of core-shell nanostructures. The nanostructures were interconnected to each other to form organogels. The carbon dots affected the reorientation of PEDOT chains and the formation of interconnected structure of PEDOT-rich domains in thin films, improving the electrical conductivity. The PEDOT:PSS thin films containing carbon dots were used as the HEL in a typical poly(3-hexythyophene) (P3HT):[6,6]-phenyl-C₆₁-butyric acid methyl ester (PCBM) BHJ OPV by solution processing. The power conversion efficiency (PCE) of the OPV devices using carbon dot@PEDOT:PSS thin films was enhanced by up to 26% in comparison to that of the OPV containing pristine PEDOT:PSS as the HEL.

The section V presents the development of gradient colloidal quantum dots (QDs)-silica composite as a luminescent down-shifting (LDS) material to improve light harvesting of the photoactive layer in OPV devices. The QDs were dispersed homogeneously in the silica matrix without aggregation and phase separation. The light harvesting of LDS layers was affected by the concentration of QDs and the thickness of the LDS layer. As a result, the PCE of OPV devices were enhanced by 8.9% compared to pristine OPV devices (without an LDS layer) due to increased incident visible light transmittance and ultraviolet light harvesting of the LDS layer.

Part III reports a study on the energy harvesting system of ECDs. Its introduction part briefly describes the characterization of ECD devices and the development of electrochromic materials.

The section I describes a study on a new type supporting electrolyte properties based on carbon dots and the performance of ECDs using carbon dots. The nano-sized carbon dots with high polarizability bear metal counter cations by electrostatic interactions and/or π -cation interactions. The (carbon-dot)⁻M_x⁺ (M

means metal cations such K^+ , Na^+ , and Li^+) was characterized by various analytical methods such as thermogravimetric analysis (TGA), Fourier-transform infrared (FT-IR), X-ray photoelectron spectroscopy (XPS), Raman, and electrochemical impedance spectroscopy (EIS). The (carbon-dot) $^nM_n^+$ electrolytes showed high thermal ($T_d = 655\text{ }^\circ\text{C}$) and chemical stability, high cation number ($n^+ \geq 24$), and good ion conductivity. In addition, the (carbon-dot) $^nM_n^+$ is nontoxic and environmentally friendly. The ECDs using (carbon-dot) $^nM_n^+$ as an electrolyte showed enhanced electrochromic performance with long cycling life, high coloration efficiency ($103.0\text{ cm}^2\text{C}^{-1}$), and optical density (0.89). These results suggest that (carbon-dot) $^nM_n^+$ exhibits prospective applications in electrochemical cells such as secondary ion battery, supercapacitor and electrochemical transistor based on superior thermal and electrochemical stability, and ion conductivity.

Keywords: Organic semiconductor, push-pull type small molecule, π -linker, carbon dots, supporting electrolyte, nanocomposite, energy harvesting, organic photovoltaic, organic photodetector, electrochromic device.

Student Number: 2012-30879

Contents

Abstract.....	ii
Part I. Introduction to Organic Semiconductors	1
1. Introduction	2
1.1 General Introduction	2
1.2 Molecular Orbital Theory	3
1.3 Optoelectronic Properties	6
1.3.1 Frank-Condon Principle	7
1.3.2 Aggregate Molecule	9
1.4 Exiton Diffusion	13
1.4.1 Förster Energy Transfer	17
1.4.2 Dexter Energy Transfer	19
1.5 Charge Carrier Transport.....	21
1.6 Charge Transfer State	24
1.7 P-N Junction Diode	27
2. Organic Photovoltaics	30
2.1 General Introduction	30
2.2 Charge Transfer and Separation	31
2.2.1 Marcus Theory.....	31
2.2.2 Onsager Theory	35
2.3 Working Principle of OPVs and OPDs	37
2.4 Introduction of Push-Pull Structure Based on Small Molecules for Organic Photovoltaics	42
2.5 Introduction of Device Architectures for Organic Photovoltaics	46

3. References and Notes	49
--------------------------------------	-----------

**Part II. Studies on Small Molecules and Carbon Dots on
Light Harvesting of Organic Photovoltaic Devices 55**

Section 1. Effect of π -linker on the Performance of Organic

Photovoltaic Devices Based on Push-Pull D- π -A Molecules 57

1. Introduction	57
2. Experimental Methods	58
3. Results and Discussion.....	67
4. Conclusion.....	75
5. References and Notes	77

Section 2. Effect of π -linker on Push-Pull D- π -A Molecules for Highly

Sensitivity Organic Photodetectors..... 81

1. Introduction	81
2. Experimental Methods	83
3. Results and Discussion.....	92
4. Conclusion.....	106
5. References and Notes	107

**Section 3 Photocrosslinkable Oigothiophene for Hole Transport Layer
in Organic Photovoltaic Devices 112**

1. Introduction	112
2. Experimental and Methods	113

3. Results and Discussion.....	115
4. Conclusion.....	119
5. References and Notes.....	120

Section 4 Self-Assembled Carbon Dot/Poly(3,4-ethylenedioxythiophene):Poly(styrene sulfonate) Organogels for Efficient Charge Transport in Photovoltaic Devices..... 123

1. Introduction	123
2. Experimental Methods	124
3. Results and discussion.....	126
4. Conclusion.....	133
5. References and Notes.....	134

Section 5 Quantum Dots-Silica Composite as an Efficient Spectral Converter in a Luminescent Down-Shifting Layer of Organic Photovoltaic Devices..... 138

1. Introduction	138
2. Experimental Methods	140
3. Results and discussion.....	142
4. Conclusion.....	148
5. References and Notes.....	149

Part III. Studies on Carbon Dots as a New Type of Supporting Electrolyte on Energy Harvesting of Electrochemical Devices	153
1. Introduction	153
1.1 General Introduction	153
1.2 Working Principle of ECDs	155
2. References and Notes	157
Section 1. Effect of (carbon dot)ⁿ⁻M_n⁺ as a New Type of Supporting Electrolyte for High-Performance Electrochromic Devices	161
1. Introduction	161
2. Experimental Methods	162
3. Results and discussion.....	165
4. Conclusion.....	176
5. References and Notes	177
국문초록	i
<u>감사의 글</u>	ii

Part I. Introduction to Organic Semiconductors

1. Introduction

1.1. General Introduction

Since the discovery of electrical conductivity has been discovered from aniline material in 1862,¹ organic semiconductors, including small molecules and conducting polymers, have been great attention in the past decades.²⁻⁷ The organic semiconductors are of interest because of flexible structure, low processing cost and unique physical properties, compared to inorganic semiconductors.^{8,9} The organic semiconductors have been used in the field of organic electronics such as organic photovoltaics (OPVs)^{9,10}, organic light-emitting diodes (OLEDs)^{11,12}, organic field effect transistors (OTFTs)^{13,14}, and organic thermoelectrics (OTEs).^{15,16} One of the great promise of organic semiconductors is that the optical and electrical properties are controlled by molecular structure.¹⁷⁻¹⁹ The molecular structures have delocalized π -electrons within conjugated π -bond such as aromatic and/or double and triple bond. That is hybridized sp^2 (or sp) orbital. It indicates that formed hybrid orbital contains strong σ -bond between s and s , or weak π -bond between s and p orbital.²⁰ These orbitals means the distribution probability of electrons in wavefunction. An s orbital is spherically symmetric around the nucleus of the atom. Three p orbital has three sub levels in a particular direction, like x , y , z . As a result, the hybrid orbital are possible sp^3 , sp^2 and sp^1 , related to involve in the hybridization. Organic semiconductors based on sp^2 hybridized are called conjugated molecule structure. The sp^2 orbital is formed by one s orbital and two of the p orbitals hybridized. The remaining one p orbital is employed to give the π -electrons in **Fig. 1.1**. Thus, the π -electrons can be distributed across in molecule through wavefunction overlap of neighboring atoms. The π -electron can move not

only optical transition on molecule but also from one molecule to adjacent molecules. The former means to generate exciton and the latter means energy transport of exciton or electron transport of free charge carrier. The physical mechanism of the transport is hopping due to weak coupling of wave function between disordered molecules at solid state.

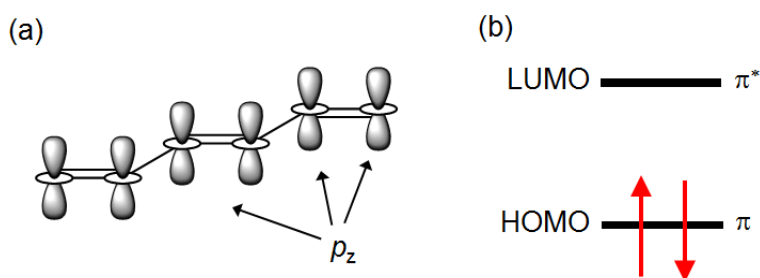


Fig. 1.1. (a) A conjugated backbone with overlapping p_z orbitals that point out of the molecular plane and (b) highest occupied and lowest unoccupied molecular orbitals (HOMO and LUMO). Arrows denote two electrons with different spins.

1.2. Molecular Orbital Theory

Molecular orbital (MO) theory is an effective way to describe the electronic and bonding state between molecules.^{21,22} The MO theory based on a *linear combination of the atomic orbitals (LCAO)* is related to the orbital states within molecules. The behavior of electrons in molecules with a number of atoms is described by a wave function (Ψ) in quantum mechanics. The wave function (Ψ) is a probability density function of electrons, related to find the spatial and distribution within an orbital in **Eq 1.1**;

$$|\psi|^2 = \psi^* \psi \quad (\text{Eq. 1.1})$$

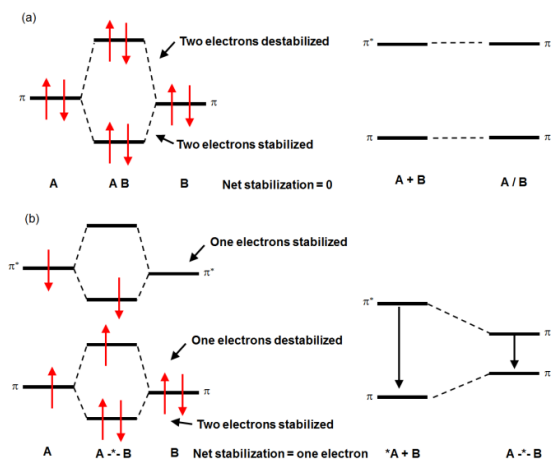


Fig. 1.2. (a) Orbital interactions of AB molecule collision pairs and (b) A^{-*}-B exciplex.

Ψ^* is complex conjugated of Ψ . **Fig. 1.2** exhibits electronic state of molecular orbitals of molecule A and B. If the electronic interactions occur between molecules, it will make their hybrid molecular orbital due to the overlap of wave function. The new molecular orbital having two electrons of opposite spin orientation can form two types of orbitals such as the bonding molecular orbital (Ψ) and the antibonding molecular orbital (Ψ^*) (the superscript “*” indicates an antibonding orbital). Two electrons in Ψ are more stable than that of the isolated molecule due to attraction between them, leading to create a force for holding the two nuclei together. Therefore, it is called bonding orbital. Two electrons in Ψ^* are located higher in energy than the original energy level in isolated molecule. The attractive force between the nuclei and these electrons pulls the two nuclei apart. Hence, it is called antibonding orbital, which is unstable. The interaction between bonding and antibonding is no gain in energy due to equal and cancel each other. Molecular orbitals of ethylene are consists of three sp^2 hybrid orbital ($2s$, $2p_x$, and $2p_y$) and a single p_z orbital each C atom in **Fig. 1.3**. And π -bond, sharing π -

electrons, is formed in p_z orbital, leading to double bond. When p_x and p_y in sp^2 hybrid orbital is overlap to same phase, the constructive wave interference increases the electron density. In opposite phase overlap, the destructive wave interference decreases electron density and creates nodes. The former creates stable σ orbital (bonding orbital) and the latter is destabilized σ^* orbital (antibonding orbital). The side-by-side overlap of two p_z orbitals gives rise to a π orbital at in-phase and a π^* orbital at out-of-phase. There are two nodal planes created. The σ orbital has a larger overlap between sp^2 hybrid orbital higher than that of π orbital, resulting in lower electronic state compared to π orbital. However, If the σ^* orbital do not overlap due to the repulsive between orbitals, σ^* orbital is in higher electronic state than that of π^* orbital. The level of electronic states are assumed $\pi^* < \sigma - \pi^* < \sigma - \sigma^*$.

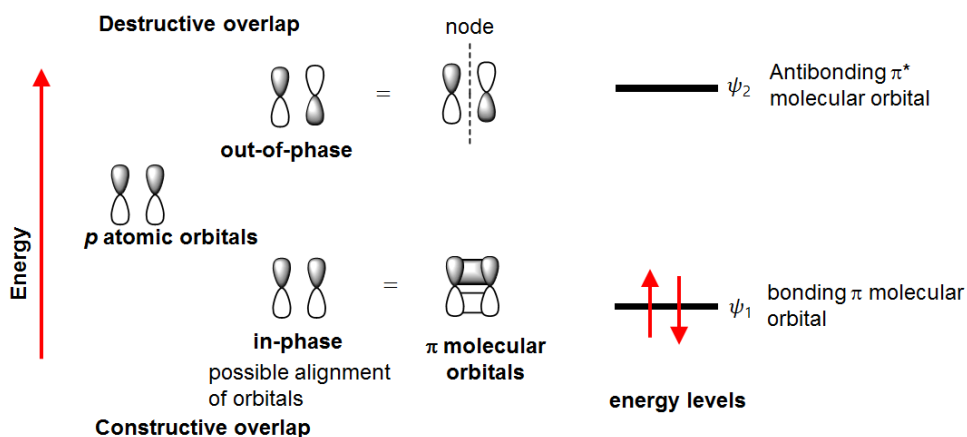


Fig. 1.3. p atomic orbitals in ethylene.

1.3. Optoelectronic Properties

The π -electron can be excited from ground state to excited state by optical transition in organic semiconductors. In this case, ground state and excited state are defined the highest occupied molecular orbital (HOMO) in the valence band and the lowest unoccupied molecular orbital (LUMO) in conduction band, respectively. The difference between HOMO and LUMO is energy gap (E_g). If the oscillating of the light wave can interact with the electrons of the molecules by oscillating dipole, the electrons in the lowest energy of the HOMO ($v=0$) are excited into a certain vibrational electronic (energy) level in an excited state. This process is the so-called transition dipole moment. It means that the probability of optical transition is represented by the wave function overlap of the initial and final state in **Eq 1.2**;

$$P(\psi \rightarrow \psi') = \langle \psi' | \mu | \psi \rangle = \int \psi' \mu \psi dr \quad (\text{Eq 1.2})$$

$$\psi = \psi_e \psi_v \psi_s \quad (\text{Eq 1.3})$$

$$P(\psi \rightarrow \psi') = \langle \psi'_e | \mu_e | \psi_e \rangle \langle \psi'_v | \psi_v \rangle \langle \psi'_s | \psi_s \rangle = \int \psi'_e^* \mu_e \psi_e dr_e \int \psi'_v^* \psi_v dr_n \int \psi'_s^* \psi_s dr_s \quad (\text{Eq 1.4})$$

$\int \psi'_e^* \mu_e \psi_e dr_e$ is transition dipole moment (electronic states overlap). $\int \psi'_v^* \psi_v dr_n$ is *Fransk-Condon* factor (vibrational states overlap). where ψ , ψ' are initial and final state, respectively. Molecule vibrates in a given electron state and has a constant of spin state Therefore, the wave function includes electronic (ψ_e), vibrational (ψ_v), and spin portion (ψ_s), neglecting the nuclear and rotational portion for approximation as shown **Eq 1.3**. The molecular dipole operator μ in **Eq 1.2** is the magnitude of a dipole moment of molecule as a function of the vibronic state. The cloud of the negatively charged electrons is around the positively charged nuclei in organic semiconductor. Thus, the dipole moment in the molecule

is related to the vibronic states of electrons to the nuclear center. Since the vibration mode in the excited state is different from that in the ground state, the excited electrons are relaxed to the lowest vibronic state in excited state through rearrangement process in order to minimize energy state with respect to the configuration of the molecule such as bond length, and angle. What is important in such a process is that it is different between the vibration wave function of the ground state and of the excited state, emission occurs from the lowest level of the excited state according to *Kasha's rule*. The electronic transition is based on vertical transitions by the *Frank-Condon transition* shown in **Fig. 1.4**.

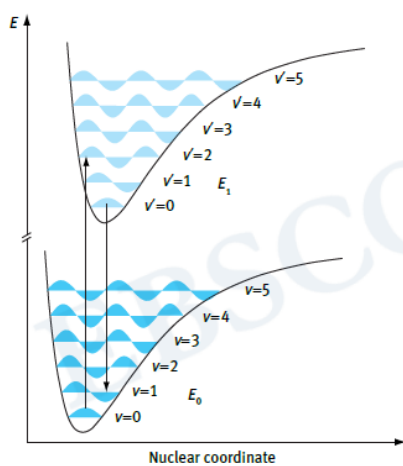


Fig. 1.4. Potential energy landscape for an optical transition between electronic states with vibrational sublevels in a conjugated molecule.

1.3.1. *Frank-Condon Principle*

The rate of electrical transitions such as absorption and emission is proportional to the overlap integral of wave function between ground state (Ψ) and

excited state (Ψ^*) in *Eq 1.2* and *Fig. 1.5*. The electronic transition, ($\Psi \rightarrow \Psi^*$, absorption) generally takes about $10^{-15} - 10^{-16}$ s, which is occurred without changes in nuclear and molecular vibration ($10^{-13} - 10^{-14}$). Because of nuclei are much more massive than electron (about 1,800 times). In such a situation, the molecule structure sustains in a ground state during the transition, resulted in vertical transition without changing any nuclear coordinate as shown blue arrow in *Fig. 1.5*. The molecule is constantly oscillated of vibrational and rotational motion. It means that the photons interact with various electronic states in ground state generating transition from $\Psi, \nu=0$ to $\Psi^*, \nu=0, 1, 2, 3, \dots$. The resulting absorption spectrum related to intensity and energy level of electronic transitions depend on the electronic distribution of the nuclei configuration initial states and the overlap of vibrational wave function ($\langle \psi | \psi^* \rangle$), respectively. After completion of the electronic transition, a certain electronic state is assumed to move to the lowest energy level in order to minimize its energy in Ψ^* . It is called reorganization process related to vibrational relaxation and thermalization in Ψ^* . The process is very faster than the rate of the electronic transition ($\Psi^* \rightarrow \Psi$, emission). At this point, the most emission process occurs vertically in the minimum electronic state in Ψ^* after changing the equilibrium geometry of Ψ^* . The electronic state minimum of Ψ^* is slightly displaced from that of Ψ depend on molecular structure. Similar to the absorption process, the transition from $\Psi^*, \nu=0$ to Ψ , various vibrational levels ($\nu=0, 1, 2, 3, \dots$) likely depends on the overlap integral maximal between wavefunctions ($\langle \psi | \psi^* \rangle$). The net result of the transition is observed different position of the energy maximum (λ_{\max}), between absorption and emission spectra, called *Stokes shift*, which means displacement of the potential energy (PE) curve in Ψ^* with respect to Ψ .

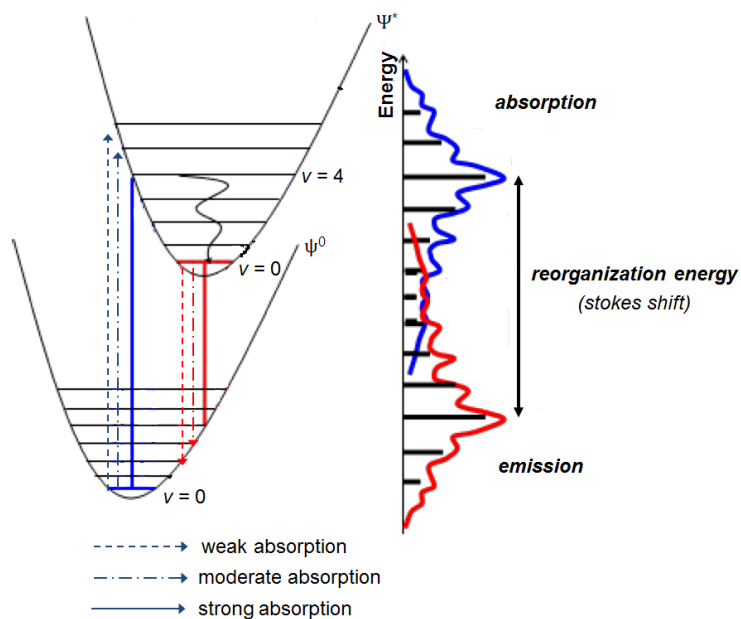


Fig. 1.5. Representation of the *Frank-Condon* interpretation of the absorption and emission of light.

1.3.2. Aggregation of Molecules

Organic semiconductors can interact by van der Waals force between these molecules at solid state which is composed of discrete molecules. Although, the properties of individual molecules are remained due to the weak intermolecular interaction, the intermolecular force influences the electronic state. Thus, the total Hamiltonian of the system (dimer) can be expressed in *Eq 1.5*;

$$H = H_1 + H_2 + V \quad (\text{Eq 1.5})$$

H_1 and H_2 are Hamiltonian for molecules 1 and 2, respectively. And V is interaction energy between molecules. The new system is not eigenfunction of

Hamiltonian (H). The electronic ground state wave function (Ψ_0) is approximated by the mixing of the two ground state wave functions $\Psi_{1,0}$ and $\Psi_{2,0}$ in **Eq 1.6**;

$$\psi_0 = \psi_{1,0} \psi_{2,0} \quad (\text{Eq 1.6})$$

It means that there have two different energy states in dimer system. As a result, the ground state energy (E_0) can be approximated in **Eq 1.7**;

$$E_0 = E_{1,0} + E_{2,0} + \langle \psi_{1,0} \psi_{2,0} | \mathbf{V} | \psi_{1,0} \psi_{2,0} \rangle \quad (\text{Eq 1.7})$$

$E_{1,0}$ and $E_{2,0}$ are ground state energy for molecules 1 and 2, respectively. And $\langle \psi_{1,0} \psi_{2,0} | \mathbf{V} | \psi_{1,0} \psi_{2,0} \rangle$ is the coulombic interaction energy (W_0) between the ground states of the dimer due to their electrical dipole moments. If one molecule is excited, this excitation can be in molecule 1 or 2. The wave function of its excited state is not identical each molecule but the energies for the combined state of dimer by interaction energy (V). Thus, the electronic excitation becomes delocalization over the entire dimer. The system oscillates between two states, in **Eq 1.8**;

$$W_1 = \langle \psi_{1,1} \psi_{2,0} | \mathbf{V} | \psi_{1,1} \psi_{2,0} \rangle = \langle \psi_{1,0} \psi_{2,1} | \mathbf{V} | \psi_{1,0} \psi_{2,1} \rangle \quad (\text{Eq 1.8})$$

It corresponds to the electronic state energy of the mixing of the two different energy states E^+ and E^- in **Eq 1.9**;

$$E^\pm = E_{1,1} + E_{2,0} + W_1 \pm \Delta E_1 \quad (\text{Eq 1.9})$$

ΔE_1 means that the energy states are increased by repulsion between electrons in the same orbital. If the attraction of electrons is occurred, the energy states are decreased. This corresponds to a splitting of the electronic states, referred to as *Davydov splitting* in **Fig. 1.6**. As shown in the *Davydov splitting* model, the different electronic states are generated by the interaction between molecules, compared to monomer. The excited singlet and triplet states are existed in two

states S_1^{m+} and S_1^{m-} , and T_1^{m+} and T_1^{m-} , respectively. As a result, the energy level difference between singlet and triplet energy level (ΔST) is reduced by the lower energy level of S_1^{m-} , and T_1^{m*} , compared to the electronic state in monomer. For systems with several molecules, the molecular orbital is adjusted. In other words, the ΔE become not only small by the divided into many energy levels but also shift by the coulomb interaction energy so that electronic states are effectively broadened. If there are many molecular orbitals in a certain finite space (unit cell) and very strong electronic coupling between them like a solid crystal structure, it is considered as a continuous band. When electrons are transited from ground state to excited state, charge is redistribution in a molecule and dipole moment is induced. This dipole is called the transition dipole moment. The strength of a dipole-dipole interaction depends on the size of both dipoles and on their orientation and proximity. The dipole moments are divided into two types as shown **Fig. 1.7**. Antiparallel end to end dipoles repel each other so that electronic states are increased to higher energy level than the original excited state. On the other hands, parallel end to end dipoles attract each other, the electronic states lies at lower energy. If the molecules are alignment on the direction of dipole moment of molecule with respect to each other, which is effect on exciton coupling depending

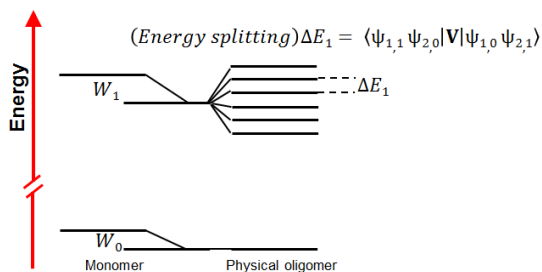


Fig. 1.6. Davydov splitting of energy levels for an ensemble of molecules.

on the type of exciton coupling, *H*- and *J*-aggregated are formed in **Fig. 1.7**.^{23,24} A *J*-aggregate is expected from head-to-tail arrangement. It is induced of the transition dipole moment with collinear pair. The lower energy exciton state is allowed due to the dipole with a length twice in parallel transition dipoles ($v \neq 0$). Another antiparallel has zero magnitude of the transition dipole vectors ($v = 0$), resulting in optically forbidden, so that the absorption is red-shifted with respect to the monomer. Therefore, *J*-aggregate is negative excitonic coupling ($J_0 < 0$). Whereas in an *H*-aggregate, the molecules are arrange in a side-by-side orientation. The transition is optically allowed to the higher lying excited state, which has a nonzero transition dipole ($v \neq 0$) and to the lower lying excited state is optically forbidden ($v = 0$). It means that the sign of the excitonic coupling of the *H*-aggregate is positive ($J_0 > 0$), resulting in blue-shift on absorption transition compared to monomer. According to the of *Frank-Condon principle and Kasha's rule*, the emission transition of *H*- and *J*-aggregate is red- and blue-shift, respectively.

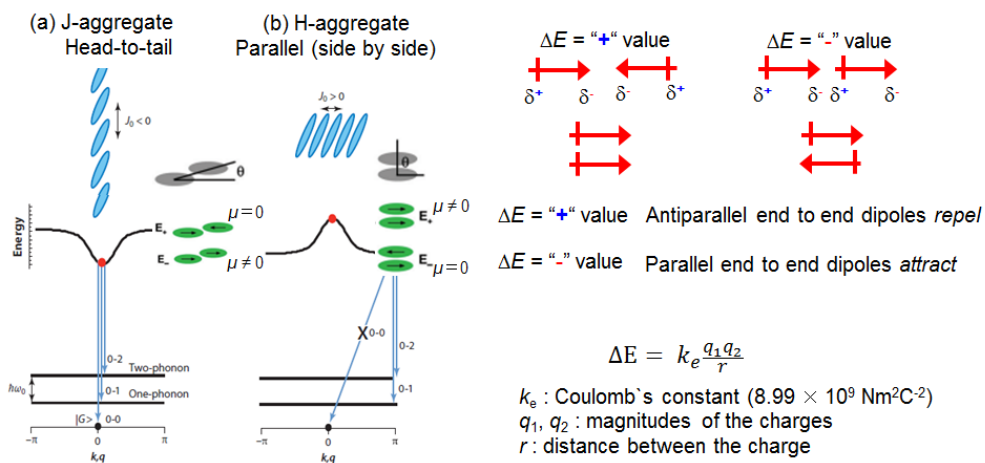


Fig. 1.7. Schematic of (a) *J*- and (b) *H*-aggregate.

1.4. Exciton Diffusion

Photoexcitation of organic semiconductors generates hole in ground state and electron in excited state. The hole and electron are strongly bound by a coulomb attraction. It is known as an exciton with electrical neutral due to the electron-hole pair. The excitons are classified three types such as *Frenkel*, *Mott-Wannier* and *charge transfer* excitons. The exciton has higher binding energy (E_B^{exc} , 0.1 – 1 eV) than that of thermal energy ($k_B T$, 29 meV) because of low dielectric constant of organic semiconductor ($\epsilon=3 - 4$). And the exciton radius (~ 10 Å) is limited by the excitonic wave function between molecules. This state is termed a *Frenkel* exciton as shown **Fig. 1.8**, and summarized in **Table 1.1**. In case of *Mott-Wannier* exciton, the excitons are delocalized over several unit cells (~ 100 Å) and have low binding energy on the order of tens of meV (0.001 – 0.1 eV) due to the high relative permittivities. Thus, the excitons can easily overcome their binding energy at room temperature so that spontaneously separate into free electron and hole polarons. The excitons generated commonly in inorganic semiconductors. *Charge transfer* (CT) excitons are found at interface of the different semiconductors such as donor (electron donating material, *p*-type) and acceptor (electron accepting material, *n*-type). The Coulombically bound excitons are comprised of partially charge separated states, where the negative polaron is in LUMO orbital of acceptor and the positive polaron is in HOMO orbital of donor. Although the binding energy (E_B^{CT}) is lower than that of *Frenkel* excitons, also should be overcome the Coulomb attraction of the interfacial CT exciton for dissociation into free charge carriers. These are intermediate in terms of charge separation between excitons and dissociated charges. The exciton binding energy can be written as **Eq 1.10**;

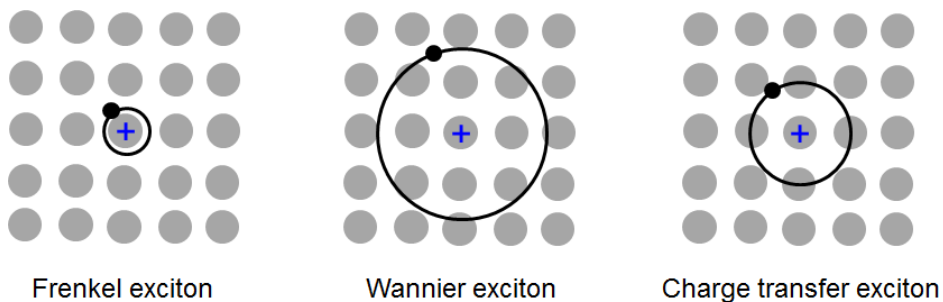


Fig. 1.8. Schematic representation of the three excitons calssifications.

Table 1.1 Exciton properties

Property	Organic	Inorganic
Bonding	Van der Waals	Covalent / Ionic
Energy level (Conduction level)	HOMO / LUMO (Molecular orbital)	Valence / Conduction band (Band)
Exciton species	Frenkel exciton	Wannier-Mott
Exciton binding energy (RT: 29 meV)	0.1 – 1.0 eV	0.001 – 0.1 eV
Exciton radius	~ 10 Å	~ 100 Å
Charge transport	Polaron hopping	Band-like

$$E_B^{ex} = \frac{ke^2}{4\pi\epsilon\epsilon_0r} \quad (Eq\ 1.10)$$

where ϵ , ϵ_0 are dielectric constant and permittivity of vacuum, respectively. r is average separation distance between the excited electron and hole. k is electrostatic constant (8.99×10^{-9}). The exciton binding energy (E_B^{ex}) is typically defined as the potential energy to produce free charge carriers, resulted from fully dissociated into electron and hole. The excited electron is going to relax with its lowest vibrational state for the minimization of energy, followed the process of recombination within $\sim \mu s$. It is referred to as exciton lifetime (τ). Within this time, the exciton can be diffused to neighboring molecules, called exciton diffusion length (L_D) in **Eq 1.11**;

$$L_D = \sqrt{D\tau} \quad (Eq\ 1.11)$$

where D is exciton diffusion coefficient. Therefore, both the local exciton generation and diffusion of exciton are accompanied by a local structural deformation in solid state. The disordered structures of the semiconductors by a different dipole direction, packing structure, and various defects affect the electronic states. It means that electronic states is disordered and become discontinuous in **Fig. 1.9(a)**. Which result in the variance of the density of states (DOS) having the delocalization degree in a Gaussian-distribution ($-\sigma/k_B T$) in **Fig. 1.9**. Therefore, the exciton diffusion moves within DOS before it recombines. At low temperature, the diffusion of excitons is mainly downhill to the low electronic states by hopping or tunneling so that localized at the bottom of electronic states or trap sites. There is a large spatial separation between the electronic states, which reduces the chance of exciton hopping. An energy loss will occur in this process. Consequently recombination process will be occurred, resulting in the low diffusion coefficient and length of exciton. This is reflected in the temperature-independent for hoppings to energetically lower sites. On the other hands, if the

excitons have enough energy to overcome the thermal energy ($k_B T$), the excitons can move to neighboring electronic states or higher electronic states by thermal fluctuations in *Fig. 1.9(c)*. This results from the higher average exciton energy (E_{ex}) by the contribution of phonons at high temperature. This leads to a larger exciton diffusion length (L_D) and coefficient in the presence of available electronic states at density of states. Thus, the exciton diffusion is strongly dependent on the properties of the organic semiconductor and the crystallinity. The mechanism of exciton diffusion is caused either Föster energy transfer or Dexter energy transfer. These systems of the energy transfer have different rate constant dependencies on factors, such as the distance separation and optical properties of molecules.

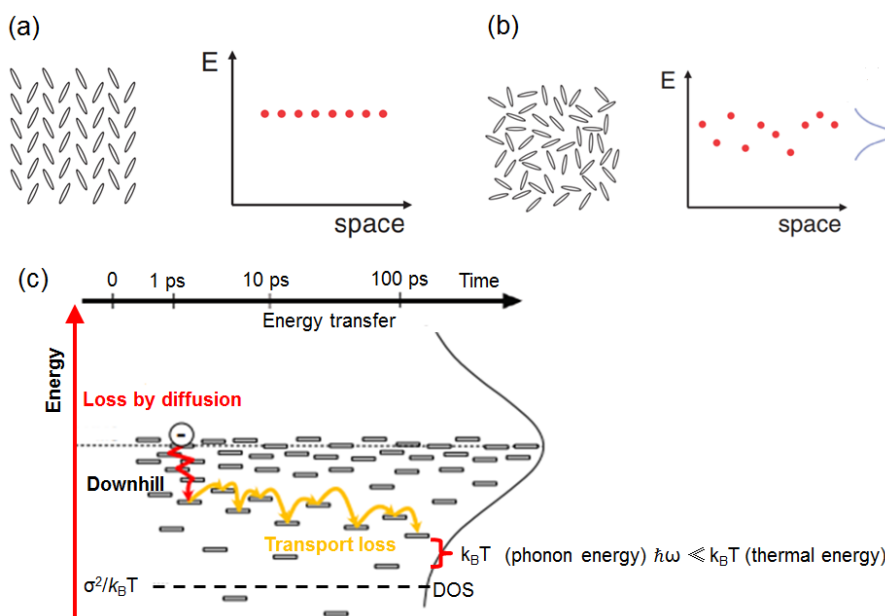


Fig. 1.9. Schematic of DOS distributions. (a) No site energy variations occur in a single crystal, (b) Gaussian disordered model for homogeneous disordered systems, and (c) Time scale of exciton energy transfer in a organic semiconductor

1.4.1.Föster Energy Transfer (Föster Resonance Energy Transfer, FRET)

Föster energy transfer is a singlet-singlet energy transfer, where the electrons of the excited state are transition to the ground state in one molecule as a *donor* (D) and the excited electron state also occurred in another molecule as an *acceptor* (A) at the same time as shown **Fig. 1.10**. Since energy transfer takes place by a resonance mechanism, i.e., dipole-dipole interaction, it doesn't require contact directly between the molecules, i.e., orbital overlap.^{26,27} The electrons in all the ground state do not oscillate (motionless). However, the absorption of photon induce the vibration of electrons, by removing electromagnetic field, so that the electrons in excited state can make an oscillating electric dipole along the molecular framework (**Fig. 1.11**). As a result, formed an oscillating electric field around the excited state of donor (D*) can trigger the creation of a coupled oscillating dipole filed to A and lead to the excited state of acceptor (A*). In the acceptor molecule, the D* is a virtual phonon. Due to the energy transfer occurs through the oscillating electronic filed generated by D*. Therefore, it is possible only in single-singlet energy transfer which have large oscillator strengths (f) and are associated with large transition dipoles (μ) in multiplicity-conserving transitions. To induce effectively for resonance between D* and A, several factors of FRET must be met in **Eq 1.12**;

$$k_f = \frac{1}{\tau} \left[\frac{R_f}{R_{DA}} \right]^6 \quad R_f^6 = \frac{9\phi_{PL}k^2}{128\pi^5 n^4} J \quad D(S) = \frac{R_f^6}{6\tau R_{DA}^4}$$

$$L_D(S) = \sqrt{D\tau_f} = \frac{1}{d^2\sqrt{6}} \sqrt{\frac{9\phi_{PL}k^2}{128\pi^5 n^4} \frac{\tau_f}{\tau_0}} \quad (\text{Eq 1.12})$$

where R_f is Föster radius, R_{DA} is donor and acceptor separation distance, τ is lifetime of exciton, τ_f is PL lifetime, ϕ_{PL} is photoluminescence (PL) quantum yield,

k^2 is dipole orientation factor, n is refractive index, and J is spectral overlap ($(\int_0^\infty F_D(\lambda)\epsilon_A(\lambda)\lambda^4 d\nu)$).^{28,29} 1). The oscillating electric field of D^* is of sufficient strength, 2). The distance between D^* and A (R_{DA}) is closed, 3). Dipole strength and spectral overlap is large for increasing energy transfer efficiency. Dipole orientation factor (k^2) is the magnitude of donor dipole (μ_D) and acceptor dipole (μ_A), and means that the interaction between oscillating dipole vector of donor and acceptor depends on the relative orientation of the donor emission and acceptor absorption dipole moment.^{28,29} This is because the dipole orientation is important for the oscillation induced by the dipole-dipole interaction. Spectral overlap (J) is overlap integral of the donor's emission spectrum and the acceptor's absorption spectrum, meaning that since the energy transfer occurs by resonance, the higher of extinction coefficient of acceptor and PL quantum yield of donor, a greater excited state of acceptor is formed. The efficiency of FRET decreases with the distance between donor and acceptor by the 6th power law (r^{-6}). Significant FRET can be generally observed in the range of 2 – 5 nm.

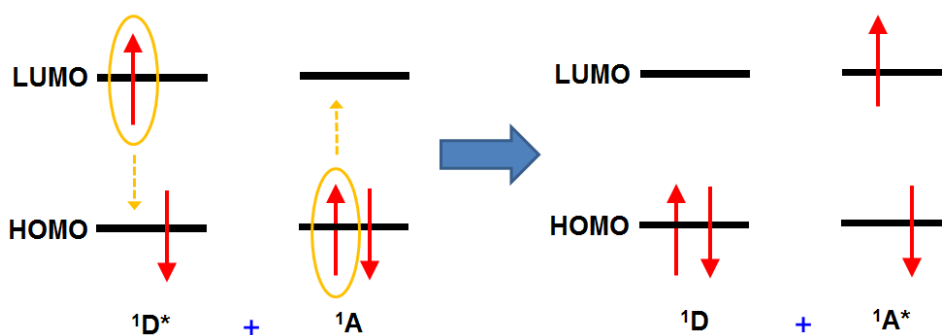


Fig. 1.10. Singlet-singlet *Förster* energy transfer. (*Dipole-dipole* interaction (long range), (don't need orbital overlap))

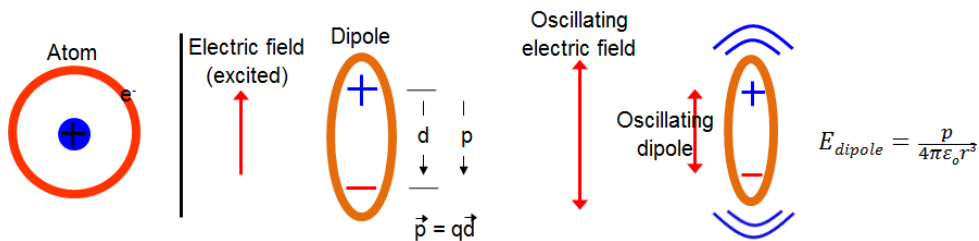


Fig. 1.11. Schematic of induced dipole moment. (The transitions $(D^* \rightarrow D$ and $A \rightarrow A^*)$ occur simultaneously as resonance by which the oscillating dipole field of D^* triggers the creation of a coupled oscillating dipole field about A and leads to A^*)

1.4.2. Dexter Energy Transfer (Electron Exchange Mechanism, FRET)

Dexter energy transfer is (DET) an exchange process in which donor donor and acceptor bilaterally exchange their electrons.^{30,31} These bimolecular interactions occur as a result of orbital overlap of excited state donor and ground state acceptor. It means that the distance between donor and acceptor must be close enough so that electrons can exchange sufficiently. In contrast to FRET, DET proceeds through the overlap of the molecular orbital function so that spin state must be preserved for DET process. Therefore, DET is possible for single-single as well as triplet-triplet energy transfer in **Fig. 1.12**. The transfer rate of DET (k_d) is affected on several factors in **Eq 1.13**;

$$k_d = \frac{1}{\tau} \exp\left[\frac{2R_d}{L}\left[1 - \frac{R_{da}}{R_d}\right]\right] \approx k_d = KJ \exp\left(-\frac{2r}{L}\right) \quad D(T) = \frac{R_d^2}{6\tau} \exp\left[\frac{2R_d}{L}\left[1 - \frac{R_{da}}{R_d}\right]\right] \quad D(S) = \frac{R_f^6}{6\tau R_{da}^4}$$

$$L_D(T) = \sqrt{D\tau} = \frac{R_{da}}{\sqrt{6}} \exp\left[\frac{R_d}{L}\left[1 - \frac{R_{da}}{R_d}\right]\right] \frac{\tau p}{\tau_0} = \left(\frac{R_{da}}{R_f}\right)^3 \exp\left[\frac{R_d}{L}\left[1 - \frac{R_{da}}{R_d}\right]\right] L_D(S) \quad (\text{Eq 1.13})$$

where R_d is Dexter radius, L is van der Waals radius, τ_d is PL lifetime, and the others factors are the same as mentioned FRET. Considering factors in *Eq 1.13*, the efficiency of DET exponentially decreases with the distance between donor and acceptor. And diffusion length of exciton is dependent on short range process due to the overlap of the wave function of two molecules. Therefore, the highest efficiency of DET is most likely to occur in π - π staking, since this is the direction of greater intermolecular electronic overlap. As a result of, The DET has an anisotropic characteristic. Compared to singlet and triplet exciton, there are the following differences. 1). The lifetime of singlet exciton has 6 order lower than that of triplet exciton which has a different spin multiplicity between excitonic states, and 2). Singlet exciton has lower binding energy and larger Bohr radius than that of triplet exciton as shown *Table 1.2*.³²

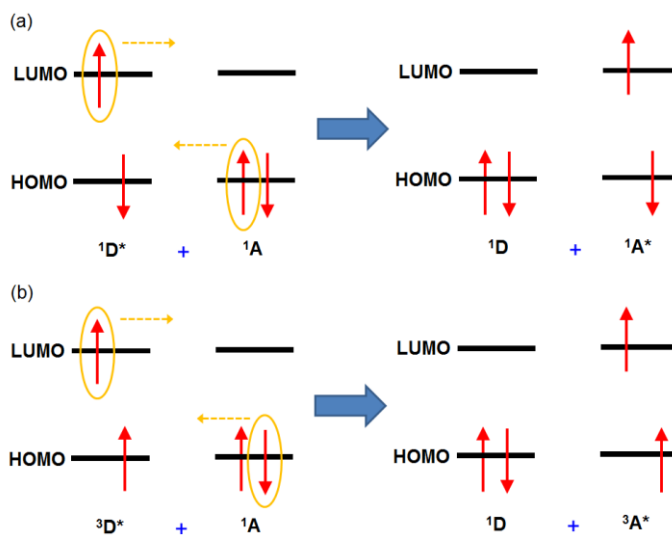


Fig. 1.12. Dexter emerge transfer (a) single-singlet dexter energy transfer, and (b) triplet-triplet dexter energy transfer. (Molecular orbital overlap (short range))

Table 1.2. Binding energy and excitonic Bohr radius for single and triplet in organic solids

Property	Singlet (S = 0)	Triplet (S = 1)
Binding energy (E_g , eV)	0.059	0.759
Excitonic Bohr radius (a_x , nm)	4.352	0.317

1.5. Charge Carrier Transport

The charge carrier transport of organic semiconductors is classified roughly three types.^{17,33,34} 1). Band-like transport in single crystalline system, 2). Polaronic transport by the coupling of charge carrier with the lattice, and 3). Disorder-based transport by uncorrelated hops in a broad density of states. It is expressed by the following *Eq 1.14*;

$$H = H_0 + H_1 + H_2 + H_3 + H_4 \quad (\text{Eq 1.14})$$

where H is a one-electron Hamiltonian formalism containing transport of hopping as well as band-like *in Eq 1.15*. This Hamiltonian assumes a low carrier density. H_1 denotes a strong wave function overlap between molecules, where relatively different coupling constants are ignored. In this case, it means a single crystalline structure in *Eq 1.15*;

$$H_1 = \sum_n V_{mn} a_n^\dagger a_m \quad J_{mn} = \langle m | H_0 | n \rangle \quad (\text{Eq 1.15})$$

a_n^\dagger (a_m) is the creation (annihilation) operator for an excited electron in an orbital of energy at the molecular site n (m). V_{mn} is the electronic interaction between site m and n . H_1 denotes that charge carriers (electrons) are highly delocalized over

lattice (several molecules) and the transfer of an electron (hole) from site m to n . H_2 and H_3 refer to the polaronic effect caused by the interaction between the electronic excitation and inter- or intramolecular vibration (electron-phonon coupling) in **Eq 1.16 – 1.17**;

$$H_2 = \sum_n \sum_l g_{nl}^2 \hbar \omega_l a_n^\dagger a_m (b_{-l}^\dagger + b_l) \quad (\text{Eq 1.16})$$

$$H_3 = \sum_{n,m} \sum_l f_{nml}^2 \hbar \omega_l a_n^\dagger a_m (b_{-l}^\dagger + b_l) \quad (\text{Eq 1.17})$$

where l, m, n are site for electron transfer. b_{-l}^\dagger (b_l) is the creation (annihilation) operator for an vibrational mode of energy $\hbar \omega_\lambda$. g_{nl}^2 and f_{nml}^2 are dimensionless coupling constant for electron-phonon vibrations. Carrier transport typically occurs via a hopping mechanism rather than via delocalized band transport. The interactions considered in the H_2 and H_3 introduce “*dynamic*” disorder, since they are based on coupling of the electronic excitation to lattice vibrations.³⁵ Which arise from oscillating of a lattice of atoms or molecules. It is called phonon having wave-like phenomena in classical mechanics as well as particle-like properties too. The phonon is a unit of lattice vibration energy ($E = \hbar \omega_k / \lambda$), analogous to a photon ($E = \hbar \omega_\lambda / \lambda$). where ω_k, ω_λ are wavenumber, and frequency, respectively. In the situation of H_2 and H_3 , when the electrons (holes) are placed into a lattice, the electrons can interact with the surrounding positive ions (negative ion).^{36,37} As a result, the lattice strain is caused by polarization locally centered on the electrons and the electrons are localized in Coulomb potential well. This is called polaron with binding energy of $E_{\text{pol}} = \lambda/2$. where λ is reorganization energy. The reorganization energy accounts for the change in the geometries of the molecules involved in charge transfer and the change in the polarization of the surrounding medium.³⁸ When the localized electrons can couple with wave-like of

phonon, the electrons can be hopped to the neighboring molecules in **Fig. 1.13**. The electron-phonon coupling, as a polaronic transport, limits on the charge carrier transport in H₂ and H₃. This is expressed in the following **Eq 1.18**;

$$\mu_{hop} = \frac{e}{k_B T} \frac{a^2}{6} k_{ET} \sim T^{-3/2} \exp\left(\frac{-E_{pol}}{2k_B T}\right) \quad (Eq 1.18)$$

where μ_{hop} is hopping rate, a is distance between lattice sites (from m to n), k_{ET} is electron transfer rate, and E_{pol} is polaronic binding energy. In contrast, H₄ describes *static disorder* from high variations of energetic (diagonal) and morphological (off-diagonal) disorder **in Eq 1.19**;

$$H_4 = \sum_n \Delta E_n a_n^\dagger a_n + \sum_{n,m} \Delta V_{mn} a_n^\dagger a_m \quad (Eq 1.19)$$

where ΔE_n , ΔV_{mn} are variation of electronic energy and interaction, respectively due to static disorder. H₄ in amorphous and mixed-phase materials is generally dominant charge carrier transport, which requires to thermal activation ($> k_B T$) for overcome the vibronic state difference between them. It is attributed to relative molecular orientation and purity of molecules, impurity and grain boundary. Therefore, this is reflected in the temperature-independent rate for hoppings to energetically lower sites at low temperature. It is responsible for the distinct differences in behavior band-like, polaronic, and static disordered transport. Electronic coupling causes the carrier to move to the neighboring molecules. The exciton or carrier migration is increased in going from a solution to a solid state due to the emergence of channels that promote hopping between the intermolecular in close distance. Polaron also has an electronic state. Therefore, the larger of the polaron binding energy, the more the carriers are localized in the polaron state. In many organic semiconductors employed in organic (opto) electronics, charge

carrier transport should be mainly determined by H_1 , H_2 , and H_3 more than that of H_4 .

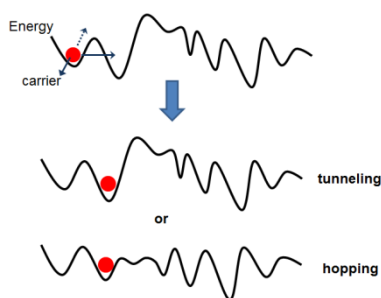
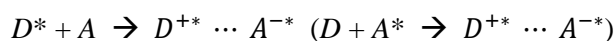


Fig. 1.13. Schematic image of carrier tunneling and hopping

1.6. Charge Transfer State

The purpose of organic optoelectronic devices such as OPV and OPD is to convert light energy into electrical energy. As shown **Fig. 1.14**, the understanding of charge transfer (CT) state is very important since the state plays a key role associated with the free charge carrier generation. When the excitons with finite lifetime diffuse to the low concentration region in photoactive layer, generally composed of donor and acceptor molecules. The excitation energy of donor is accessible energetically to form the CT state at interface so that the CT state is populated through electronic coupling according to the molecular orientation between donor and acceptor at interface. It means that electronic states of the CT state are obtained by mixing the HOMO of the donor and the LUMO of the acceptor, leading to the different electronic states to the bulk layer. If the HOMO level of donor is lower than that of acceptor, electron transfer from acceptor to

donor is occurred. As a result, the charge is partially separated by a polaron pair with the negative polaron (electron) residing in the acceptor and the positive polaron (hole) in the donor so that lowered Coulombic attraction. The generally used nomenclatures for the CT state are diverse such as polaron pair, geminate pair, intermolecular radical pair, interfacial charge pair, charge transfer complex, and exciplex. This can be expressed as;



The CT state can alternatively be populated by a direct excitation into a weak absorption band of CT state. The polaron pair as a CT state is likely to convert into a

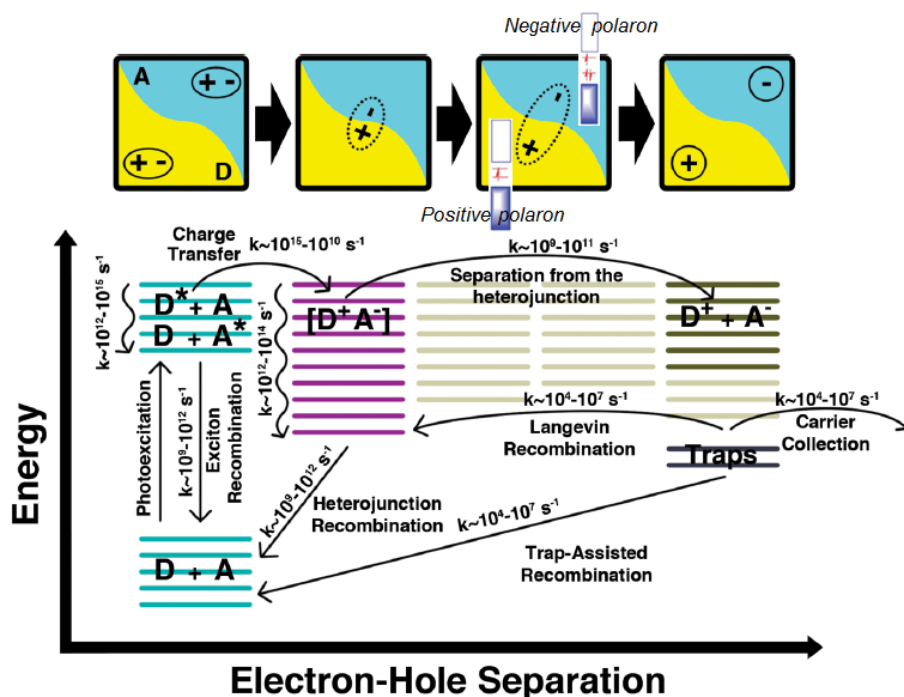


Fig. 1.14. Energy level diagram summarizing the main processes involved in charge photogeneration. Reproduced with permission from ref 8. Copyright 2009 American Chemistry Society.

free charge carrier but may not convert for the following reasons. If charge separation is not complete within the lifetime of the CT state, geminate recombination occurs. Which occur the orbital overlap between electron of LUMO in acceptor and hole of HOMO in donor due to the strong Coulombic interaction exceeding $k_B T$. Another reason is back electron transfer from the CT state to the lower locally-excited (LE) state of donor so that charge separation is impossible. The excitons eventually recombine to the ground state of donor. The electronic coupling can be expressed as **Eq 1.20**;

$$\langle \psi_{CT} | \mathbf{H} | \psi_{LE} \rangle \quad (\text{Eq 1.20})$$

Thus, the electronic wave function overlap occurs between locally-excited (LE) state of donor and of the charge transfer state for the charge separation (CS) state or the CT state and ground state donor (acceptor), resulting in a charge recombination process. As a result, the excitons should be electronic coupling between donor and acceptor and have high excess energy for the generation of free charge carriers. The CT state dissociation efficiency depends on the driving force (Gibbs free energy, ΔG_0) for electron transfer from the donor to the acceptor as well as on the initial thermalization length and the critical radius (r_c). The driving force (ΔG_0) is correlated with the LUMO level offset between the donor and acceptor, related to *Marcus* theory.^{8,39,40} And the factors with r_a and r_c are according to *Onsager* theory.^{41,42} Although there is still controversy about the formation of polaron pair, which occurs on greater than picosecond timescales (~ 100 fs) for charge separation, interfacial CT states are generally observed by time-resolved photoluminescence (PL) and transient absorption spectroscopy. When the CT state is formed at interface of donor/acceptor, the excess energy generated is used to dissociate to the charge separation (CS) state before thermalization. These excitons are called “Hot exciton”, means higher excited CT state.^{43,44} Although the cold exciton can form CS state by photon absorption or external energy such as

thermal, electrical energy, the cold exciton is less to be dissociated into the CS state relative to the hot exciton. The polaron pair with larger thermalization length (r_a) between the electron and hole is more likely to be converted to the CS state by the following factors. 1). The influence of the energetically disordered electronic states at the interface, 2). Local electric field of interfacial by dipole moment of molecules, 3). The delocalization effect of exciton and polaron pair on molecules near interface, 4). The excess energetic of exciton at interface, and 5). Entropy effect reducing the Coulomb binding energy.

1.7. P-N Junction Diode (Donor-Acceptor Junction Diode)

Most of the photoactive semiconductor in organic photovoltaic devices consists of the donor as a p-type and acceptor as an n-type semiconductor. When p- and n-type are brought into contact, forming p-n junction, the Fermi-level alignment is occurred and there is a band bending. Free electrons move from the p-type to the n-type, and negative ions are present in the p-type by electrostatic potential.^{46,47} In the n-type, the opposite phenomenon occurs. This is possible since electrostatic potential is generated across in the p-n junction. The electrostatic potential leads to the formation of space charge region which is depleted of free charge carriers. There is referred to as a depletion region with an equilibrium built-in potential (V_{bi}). The free charge carrier is polaron because positive (negative) ions in the lattice interact with electrons (holes), resulting in moved toward n-type region (p-type region). Far away from the junction, electrostatic potential is disappeared due to the equilibrium density between electrons and holes, resulting in flat band. A schematic of the p-n junction diode according to the external electric field is shown in *Fig. 1.15*. The charge density of organic semiconductors is very low due to the high exciton binding energy. Thus, the depletion region is

not well formed because charge flow at the interface of donor and acceptor is difficult to occur compared to inorganic p-n junctions. However, if the exciton can diffuse toward at interface, it can convert a positive polaron in the donor and a negative polaron in the acceptor such as a polaron pair. In other words, positive radical ion in p-type semiconductor and negative radical in n-type semiconductor are formed, leading to the polarization effect. As a result, built-in potential is generated by the dipole moment of these radical ions. Carriers separated at the interface move to each electrode depending on the degree of external bias, and eventually current is generated. The current density is sum of the drift and diffusion current. When the forward bias is applied in the device, the external electric field is opposite to the built in potential so that the electrostatic potential is lowered. It is expressed in **Eq 1.21**;

$$V_{\text{junction}} = V_{\text{bi}} - V_{\text{ext}} \quad (\text{Eq 1.21})$$

where V_{junction} , V_{bi} , and V_{ext} are the voltage drop across the junction, built-in potential, and externally applied potential, respectively. Fermi level of the equilibrium state is also changed at that time. E_{Fn} exists higher than E_{Fp} by V_{F} . E_{Fp} , and E_{Fn} are the *Fermil* level of donor, acceptor, respectively, and V_{F} means applied forward bias. This means that current is generated by electrons in the n-type that diffuse to the p-type beyond the electrostatic potential barrier, and holes in the p-type toward the n-type. This is called the diffusion current through which current is transported due to local difference in the concentration of the charge. The diffusion current is dramatically increased by majority carriers at forward bias in **Eq 1.22**;

$$J_{\text{diffusion}} = -qD \frac{dn}{dx} \quad (\text{Eq 1.22})$$

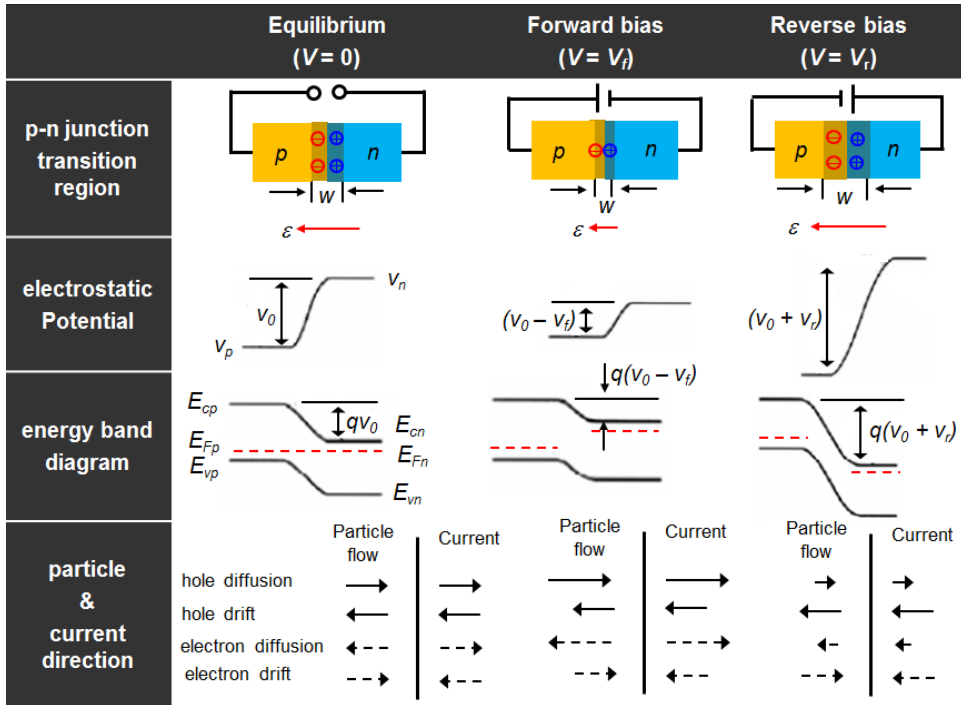


Fig. 1.15. A schematic of the p-n junction diode (*p*: p-type region, *n*: n-type region, *w*: depletion region)

$$J_{diffusion} = -qD \frac{dn}{dx} \quad (Eq 1.22)$$

where q (1.6×10^{-19} C) is electron charge, D (cm^2/s) is the diffusion coefficient for the carrier (electron or hole), and n is the concentration of carrier (electron or hole). The majority carriers are injected through each electrode (anode and cathode). On the other hand, the drift current is the flow of minority carriers by the built-in potential in the space charge region. The electrons and holes are minority charge carrier in the p-type and n-type region, respectively at this time. The drift current always flows in the direction of electric field, regardless of the electrostatic potential barrier. The holes are in the same direction as the electric field, whereas

the electrons move in the opposite direction to the electric field. The amount of drift current depends on how many minority carriers (free charge carriers) are generated at space charge region. In terms of OPVs and OPDs, the space charge region is the interface between the donor and acceptor semiconductor. Therefore, generated minority carriers are determined by the dissociation of the charge transfer exciton. The drift current is expressed in **Eq 1.23**;

$$J_{drift} = q\rho\mu E \quad (Eq 1.23)$$

where μ (cm^2/Vs) is carrier (electron or hole) mobility, E (V/cm) is electric field ($\frac{d\phi}{dx}$). Applying a reverse bias to the p-n junction increase the electrostatic potential barrier so that the free charge carrier density are increased due to the increasing width of the space charge region. As result of, the drift current is dominantly generated, compared to diffusion current. For forward bias, the space charge region becomes smaller with the reduced electrostatic potential barrier. A higher diffusion current is flow through the device since charges are injected into the junction.

2. Organic Photovoltaics (Organic Optoelectronics)

2.1. General Introduction

The interesting of renewable energy, alternative, and eco-friendly sources is increasing due to the environmental problems represented by global warming and environmental disease of human. Among them, the infinite solar energy is emerging as a next-generation energy source since the sun delivers a constant energy of around $1,360 \text{ Wm}^{-2}$ above earth`s atmosphere. It can cover all the energy that mankind needs with just 0.1 % of solar energy. In addition to, the energy of the

sun can also be used in various fields such as photovoltaics (PVs), and photocatalysis, and solar thermal energy. Since the photovoltaic effect was observed in the 1930s by Alexandre Edmond Becquerel, PVs are expected to have the largest renewable energy source. The PVs are environmentally friendly devices that convert light energy from the sun into electrical energy. As can be seen from the spectrum of sunlight, most of the ultraviolet rays are blocked, and the photon of visible and infrared regions enter the Earth's atmosphere. At this point, if the solar energy of visible region (400~700 nm) is converted into 100 % electrical energy, the power conversion efficiency (PCE, η) of a 30.7 % can be obtained. As a result, organic optoelectronic devices such as OPVs and OPDs based on organic semiconductors have drawn much attention as potential next-generation renewable energy sources on account of low production costs and solution processability, which becomes possible of mass production of organic electronics viable.

2.2. Charge Transfer and Separation

2.2.1. Marcus Theory

Since Marcus theory is developed by Rudolph Marcus in 1956, its variation is widely used in the study of charge transfer and separation in organic photovoltaics.⁴⁰ Marcus theory describes electron transfer process from an orbital on donor molecule to an orbital on acceptor molecule. In *Fig. 2.1*, the potential energy surface (PES) of donor and acceptor is exhibited by the parabola on the left and right, respectively. The x-axis implies reaction coordinate which represents the change in the geometry of the donor and the surrounding medium. Electron transfer is occurred by harmonic oscillating of the vibronic states between the donor and acceptor at the intersecting point in order to satisfy both the *Frank-Condon*

principle and energy conservation requirement. This is because the vertical transition arises from *Frank-Condon* principle, and the horizontal transition is generated by the energy conservation requirement as show **Fig. 2.1**. The electron transfer rate (k_{et}) by the Marcus theory is determined as **Eq 2.1**;

$$k_{et} = \frac{2\pi}{\hbar} [V_{DA}]^2 \frac{1}{\sqrt{4\pi\lambda k_B T}} \exp\left(-\frac{(\lambda + \Delta G_0)^2}{4\pi\lambda k_B T}\right) \approx \Delta G^\ddagger = \frac{(\lambda + \Delta G_0)^2}{4\lambda} \quad (\text{Eq 2.1})$$

where V_{DA} is electronic coupling of the donor and acceptor molecules, ΔG^\ddagger is energy activation barrier, ΔG_0 is Gibbs free energy, and λ is reorganization energy. The ΔG^\ddagger is related to the activation energy required to reach the transition state (TS[‡]) from the lowest PES of the donor to acceptor for electron transfer. Thus, driving force needs for overcoming the energy barrier (ΔG^\ddagger) at the TS[‡] of the two PES curves. The excited donor molecules have to reorganize their nuclei and electrons to stabilize through relaxation. The reorganization energy λ divided into inner (λ_{in}) and outer sphere (λ_{out}). The λ_{in} refers to the required energy due to the geometry changes of the donor and acceptor such as charge redistribution, bond lengths and angles, relating to the gain or loss of electronic charge upon electron transfer. The λ_{out} contributes from changes in polarization of the surrounding medium. In fact, λ_{out} means that solvent reorganization energy which may have to undergo considerable reorganization of solvent molecule is accompanied by the change in free energy for electron transfer process. The solvent reorganization energy, from this perspective, is related to lattice distortion by polaron hopping in solid state.^{48,49} As a result, the λ is associated with the activation energy, considering the fact that might require a significant amount of energy for an electron transfer reaction. The excited donor molecules and the surrounding medium are accompanied by reorientation to obtain the lowest energy pathway along the reaction coordinate for electron transfer. It is for an electron transfer

reaction transfer reaction occurred at the crossing point for the intersection of the PES for donor and acceptor molecules, referred to the transition state. That means electron transfer between donor and acceptor molecules may or may not occur at this point.^{50,51} If weak electronic coupling by the small overlap of electronic wave function between them is generated at this intersection point, electron transfer occurs by non-adiabatic process. On the other hands, the adiabatic process arises from the strong electronic coupling between them. The ΔG_0 represents the difference in free energy between the donor and acceptor molecules, referred to the driving force for electron transfer reaction. Based on the correlation of these parameters values (ΔG_0 , ΔG^\ddagger , and λ) which provides a quantitative relationship for the k_{et} in **Eq 2.1**. the energy relationship for electron transfer reaction can be explained. The electron transfer is hardly to occur at endothermic ($\Delta G_0 > 0$, a positive value) due to high value of ΔG^\ddagger . As ΔG_0 becomes more exothermic, however, the TS^\ddagger moves closer and closer to the minimum of the PES curve of the excited donor molecule so that the energy barrier (ΔG^\ddagger) continuously decreases, leading to the increasing k_{et} in **Fig. 2.2(a)**. Eventually, the value of ΔG^\ddagger will be zero and the k_{et} will be at a maximum when the ΔG_0 matches λ in **Fig. 2.2(b)**. According to the reaction becomes more and more exothermic beyond $\Delta G_0 > \lambda$, the

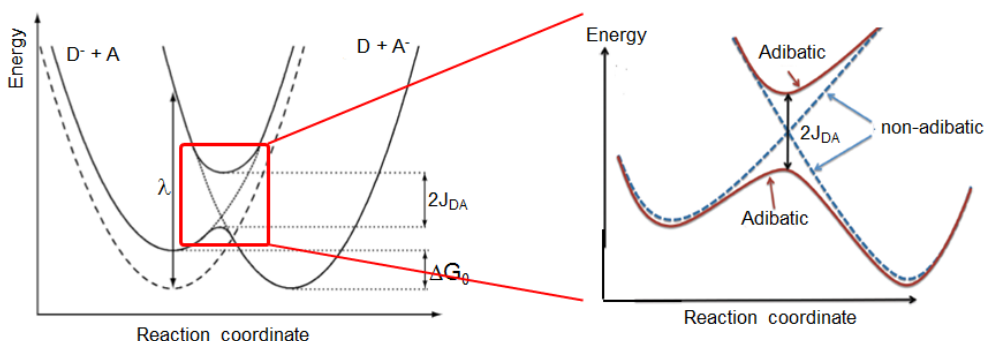


Fig. 2.1. Energy diagram for an electron transfer process from donor molecule (D) to acceptor molecule (A).

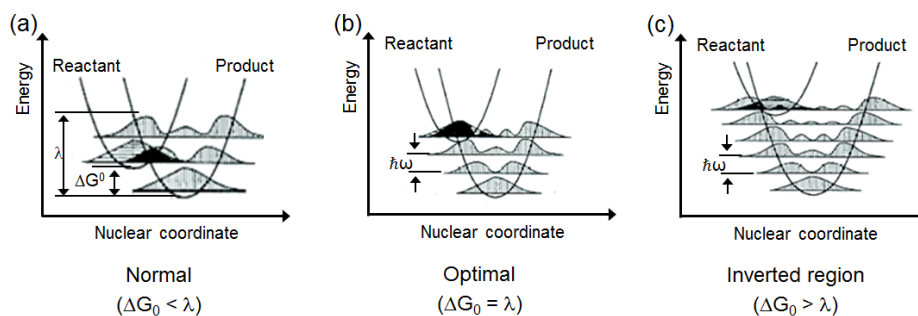


Fig. 2.2. Schematic diagram of Marcus regions

PES curve of acceptor molecule intersects above the minimum of the PEC curve of the excited donor molecules, meaning the value of ΔG^\ddagger is increased again. As a result, the k_{et} will be decreased again in **Fig. 2.2(c)**. By Marcus theory, as long as $\Delta G_0 < \lambda$, the region for which the rate of electron transfer (k_{et}) increases with increasing negative value of ΔG_0 is termed the normal region ($\Delta G_0 < \lambda$). In this region ($\Delta G_0 = -\lambda$) is termed optimal region, the value of ΔG^\ddagger is zero according to the **Eq 2.1**. This result corresponds to the maximum k_{et} . In inverted region from $\Delta G_0 = -\lambda$ to any value of $\Delta G_0 > -\lambda$, the increasing the negative value of ΔG_0 makes the term $(\Delta G_0 + \lambda)^2$ of **Eq 2.1** increasingly positive so that the value of k_{et} decreases. When approaching the Marcus theory to the perspective of organic photovoltaic, the excited donor molecule by optical transition relax to the lowest electronic state similar to the lowest PES curve within 100 fs.⁵² If the activation energy is required to form the CT state by electron transfer to the LUMO of acceptor from the LUMO of donor, thermal energy is used for overcoming the energy barrier at the TS. The thermal energy is related to the intramolecular reorganization energy, λ_i , which is the difference between the absorption λ_{max} of the donor and the emission λ_{max} of the CT state. It means that the electron transfer is affected by the overlap of wave

function between the LUMO of donor and acceptor. The electronic wave function can be expressed as;

$$\langle \psi_{CT} | \mathbf{H} | \psi_{LE} \rangle \text{ or } \langle \psi_{donor} | \mathbf{H} | \psi_{CT} \rangle$$

It is, therefore, related to the overlap of electronic wave function between the LE state of donor and the CT state, or between the CT state and the ground state of donor. The former relates to the charge separation (CS), the latter to the charge recombination (CR) process. The vibronic oscillation of the donor can help to couple to the acceptor, and the reaction in the direction of decreasing Gibbs free energy is beneficial for the energetically undesirable electron transfer path. For instance, when the curve crossing between the exciton and charge transfer states (driving force) occurs at the minimum potential energy point of the exciton state and the energy of charge transfer state is low enough, the rate of the exciton dissociation predicted by Marcus theory is increased. However, a low energy of the charge transfer state loses the efficiency of the solar cell because this driving force is directly related to the open circuit voltage and dark current of the photovoltaics.

2.2.2. Onsager Theory

Onsager theory, proposed by Lars Onsager in 1938 year, has been applied to charge separation of exciton in CT state into electron and hole.⁴¹ As shown **Eq 2.2**, Coulombic radius (r_c) means of Coulomb attraction between the electron and hole, referred to the thermal energy in equilibrium ($k_B T$). Due to the $k_B T$, the electrons can be travel some distance away from the hole. This is called a thermalization length (a). And ϵ_r , ϵ_0 are dielectric constant of the material and vacuum permittivity (8.85×10^{-12} F/m), respectively.

$$r_c = \frac{e^2}{4\pi\epsilon_r\epsilon_0k_B T} \quad (\text{Eq 2.2})$$

The probability of charge separation (P) can be expressed as **Eq 2.3**;

$$P(E) = \exp\left(\frac{-r_c}{a}\right) \left(1 + \frac{er_c}{2k_B T}(E)\right) \quad (\text{Eq 2.3})$$

where E is the strength of the electric field, which is formed by an external bias and/or a built-in potential due to the dipole moment at the interface of the donor and acceptor. The electron and hole can be separated when $a > r_c$. According to Onsager theory, high thermalization length with the delocalized exciton, high temperature, and high electric field promote separation of exciton. If the exciton forms a CT state with little initial energy loss when reaching the interface through energy transfer, the polaron pair in CT state can be thermally relaxed beyond the Coulombic radius due to the polaron pair has excess thermal energy, such as hot exciton. It means that hot exciton in a high-energy state in the Gaussian-distributed density of states (DOS, σ) can be separated over a series of several hopping to lower energies and thermally induced hoppings to higher energies before the approaching at the lower end of the DOS.⁵³⁻⁵⁵ As shown **Fig. 2.3**, a high-energy state in the DOS has many local hopping sites with less energy offset between sites as distribution of energies available for a transported charge carrier, leading to the increasing the probability of charge separation. It should be taken into account the fact that in case of OPVs. Although these partial dipoles from the dipole moment of donor and acceptor at the interface generate a repulsive electrostatic potential barrier, the external bias is not strong enough to have a significant effect for charge separation. The OPDs, however, have a large external reverse bias so that the electric field plays a significant role in charge separation.

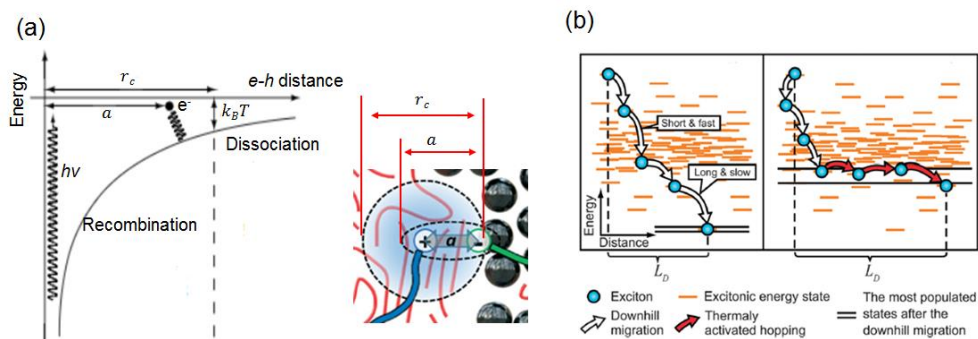


Fig. 2.3. (a) Potential energy diagram summarizing Onsager theory for autoionization. It a is less than the Coulomb capture radius, r_c , then the electron-hole pair can either undergo geminate recombination or dissociate into free charges. (b) Illustration of the exciton diffusion process. The Gaussian density of states is represented by the distribution of the energies of excitonic states.

2.3. Working Principle of OPVs and OPDs

To convert photon energy into electric energy or signal, it involves the following series of processes. 1). Organic semiconductors should absorb photon from light and generate excitons by optical transition from ground state to excited state in organic semiconductors, 2). The excitons diffuse toward the interface between the donor and acceptor phase through *Föster* or *Dexter* energy transfer within 100 fs usually, 3). The excitons of the CT state with an intermediate nature are formed at the interface, 4). The excitons are separated by free charge carriers (electrons and holes) due to the driving force, (i.e., local electric field, energetically disordered electronic states, and Entropy effect, etc), 5). The separated electrons and holes move to the cathode and anode, respectively.⁵⁶⁻⁶⁰ A successful charge

generation and collection event in a bulk heterojunction is schematically depicted in **Fig. 1.14**. In order to quantify the efficiency to the conversion of photons, one defines the so-called *external quantum efficiency* (EQE) or *incident photo-to-current efficiency* (IPCE).

$$\text{EQE} = \frac{\text{number of photogenerated electrons per second}}{\text{number of incident photons per second}}$$

This EQE can be expressed as **Eq 2.4**;

$$\eta_{\text{EQE}} = \eta_A \times \eta_{\text{IQE}} = \eta_A \times \eta_{\text{ED}} \times \eta_{\text{CS}} \times \eta_{\text{CC}} \quad (\text{Eq 2.4})$$

where η_A is exciton generation efficiency, η_{ED} is exciton diffusion efficiency, η_{CS} is charge separation efficiency, and η_{CC} is carrier collection efficiency. As can be understood from the above equation, the EQE includes the *internal quantum efficiency* (IQE) depending on the photon energy. The defined IQE means that how efficiently the excited states are separated into free charge carriers and subsequently collected at the each electrode per number of absorbed photons.

$$\text{IQE} = \frac{\text{number of photogenerated electrons per second}}{\text{number of absorbed photons per second}}$$

In case of OPVs, light energy converts into electrical energy. That is, *power conversion efficiency* (PCE) is important. The PCE of the OPVs is defined as the ratio of out power to incident light power as follows;

$$\text{PCE} = \frac{P_{\text{out}}}{P_{\text{in}}} \quad (\text{Eq 2.5})$$

Where P_{out} of the OPVs is given as

$$P_{\text{out}} = V \cdot J \quad (\text{Eq 2.6})$$

where V and J are voltage and current density through the device, respectively. The parameters determined the PCE of the OPVs can be derived from current-voltage (J - V) curve. As shown **Fig. 2.4**, the open circuit voltage (V_{oc}), short-circuit current density (J_{sc}), and fill factor (FF) are defined under illumination. These figure of merits are expressed by **Eq 2.7**.

$$\text{PCE} = FF \times \frac{V_{oc} \times J_{sc}}{P_{in}}, \quad FF = \frac{V_0 \times I_0}{V_{oc} \times J_{sc}} \quad (\text{Eq 2.7})$$

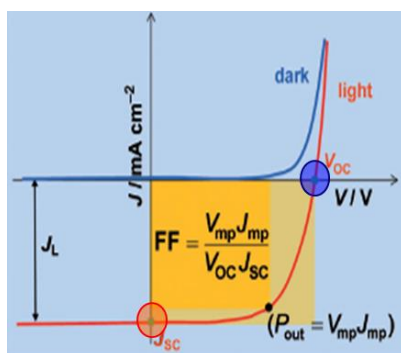


Fig. 2.3. J - V curve of OPV device plotted current density, highlighting the short-circuit current density (J_{sc}), open-circuit voltage (V_{oc}), current and voltage at maximum power output (FF , Fill factor)

V_{oc} mainly depends on the difference of offset between the HOMO of donor and the LUMO of acceptor. The V_{oc} means that no current is flow through the device at the point because the magnitude of drift and diffusion current are equal. J_{sc} represents the maximum of photogenerated current density when the voltage across the device is zero. FF describe for how the shape rectangular the J - V curve meaning the maximum power output of the OPVs. The value of these parameters is reflected the properties of organic semiconductor and device structure. In fact, the rate of charge separation (k_{CS}) competes with two recombination pathway. One is the rate of geminate recombination (k_{GR}) and another is non-geminate recombination (k_{GR} , bimolecular recombination). The geminate recombination is

occurred by the excitons recombine at the interface without being separated into free charge carriers.⁶¹⁻⁶³ The non-geminate recombination is generated recombination of separated charges. Separated opposite charges are to encounter each other at the isolated domains either donor or acceptor before collected at each electrode. Thus, the excitons in the CT state are formed again, and eventually the recombination process can occur.^{61,64} Or additional surface recombination of free charge carriers can be caused if either the holes in donor domain (the electrons in acceptor domain) are in directly contact with cathode (anode). The competitive recombination rate (k_{CS} , k_{GR}) to the charge separation rate is represented by two parasitic resistances in the equivalent circuit, involving a series resistance (R_s), and a shunt resistance (R_{sh}) parallel to the device as shown in **Fig. 2.5**. The R_{sh} is related to defects and pinholes in the photoactive layer. The phenomenon can be approximated from the inverse slope of the J - V curve at reverse bias, resulting in reducing FF and V_{oc} values. The R_s is caused by the electrostatic potential barrier in the device. The electrostatic potential barrier is associated with grain boundary where intermolecular interactions are different from each other. The external connections (i.e., cable, contact resistance, etc.) and the transparent conductive oxide metal (i.e., indium tin oxide, ITO) also cause R_s . As a result, the transport of carriers is interrupted by these barriers. The inverse slope of the J - V curve in forward bias is increased, resulting in increasing FF and J_{sc} values.

One type of photovoltaics, OPDs is distinguished from OPVs in that converts a light energy into electrical signal such as current or voltage so that the magnitude of current generated by light is important. A key parameter for OPDs is the dark current (J_d), and photogenerated current (J_{ph}) not relevant of FF , V_{oc} . The following figure of merits determines the characteristics of OPDs in **Eq 2.8**. The specific detectivity (D^* , $\text{cmHz}^{1/2}/\text{W}$) considered a key parameter is expressed as;

$$D^* = \frac{R}{(2qJ_d)^{1/2}} = \left(\frac{J_{ph}}{P_{light}} \right) (2qJ_d)^{1/2} \quad (\text{Eq 2.8})$$

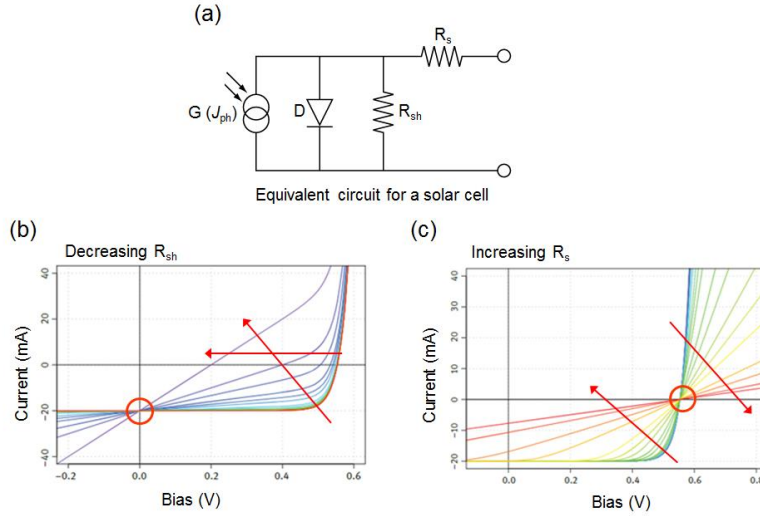


Fig. 2.5. (a) Equivalent circuits for OPVs, impact of (b) decreasing shunt resistance (R_{sh}), and (c) increasing series resistance (R_s) on the shape of the J-V curve

$$D^* = \frac{R}{(2qJ_d)^{1/2}} = \left(\frac{J_{ph}}{P_{light}} \right) (2qJ_d)^{1/2} \quad (Eq 2.8)$$

where responsivity (R , A/W) is the ratio between the output photogenerated current and the incident light power. q is electron charge (1.6×10^{-19} C), J_d and J_{ph} are dark current density and photogenerated current (A/cm^2), respectively. Thus, D^* is the ability to detection a small photo signal and R is the magnitude of current that can be generated from the incident light per area. A high frequency response is also critical factor corresponding to the response time taken to generate and extract the generated carriers (electrons and holes). The frequency response is related the -3 dB bandwidth, which is limited by the signal from 10% to 90% of the final value (rise time (t_r , or transit time)) or from 90% to 10% of the final value (decay time (t_d , or RC delay time)). The -3 dB is derived that power is expressed by current (I) \times voltage (V). When the power is reduced by half and is given by $\frac{P}{2} = \frac{V \times I}{2}$, then the

current and voltage are reduced at the same rate, $\frac{P}{2} = \sqrt{\frac{V \times I}{2}}$. Therefore, it can be expressed as $\frac{P}{2} = 10 \times \log(1/2) = -3.01$ at half the power. The rise time is $t_r = \frac{d^2}{\mu V}$, where d is active layer thickness, μ is carrier mobility, and V is applied voltage. It means that the rise time depends on the carrier mobility and the dielectric constant of organic semiconductors. Although decreasing the thickness of active layer can decrease the rise time, the delay time is determined from the sum of the diode resistance (R) and capacitance (C) so that decay time is increased. It is because the capacitance is the inverse of the thickness. The OPDs are usually operated in the strongly reverse bias, leading to the following benefits; 1). Reducing rise time by the increasing drift velocity of the carriers with increasing strong electric field, 2). Increasing the width of the space charge region, expressed by $(V_0 - V)^{1/2}$ (where V_0 is initial volage, and V is applied voltage), 3). Reducing the junction capacitance ($C = \frac{\epsilon A}{l}$) and decreasing the response time (where C is capacitance, ϵ is dielectric constant of organic semiconductor in active layer, A is area of space charge region, and l is thickness of space charge region), 4). Increasing photosensitive area (p-n junction).

2.4. Introduction of Push-Pull Structure Based on Small Molecules for Organic Photovoltaics

A variety of organic semiconductor materials with chemical versatility have been reported in organic semiconductors.⁶⁵⁻⁶⁸ The general structures are push-pull dyes consisted with electron donating (D) and electron withdrawing (A) substituted π -

conjugated systems in **Fig. 2.6**. Generally π -electrons are counted differently depending on the carrier type: for hole transfer, only π -electrons on carbon atoms are considered whereas two π -electrons per sulfur (or nitrogen) atom are also added for electron donation. This type of molecular architecture is very effective for the development materials include with appropriate band gaps and energy levels in order to prompt light harvesting. Phthalocyanine, benzothiadiazole, malononitrile, indanedione, squaraine, diketopyrrolopyrrole, and julolidine are the typical materials used in electron withdrawing units. Electron donating units include triphenylamine, fluorene, benzodithiophene, thienodioxine, and dithinothiophene as dye molecules. Among them, triphenylamine (TPA) with three-dimensional propeller structure and their derivatives are become a suitable component unit for electron donating moiety. Although upon protonation on the nitrogen atom, the structure changes from the nearly planar geometry to a near-tetrahedral configuration, they have high hole-transporting abilities and electron donating capabilities due to the easily oxidized to form stable radical cation by the delocalized electrons.^{69,70} However, the low molecular weight compounds of TPA derivatives have problems such as the lack of the thermal stability and the mechanical strength. Diketopyrrolopyrrole (DPP) is also an attractive building block in terms of facile synthetic modification on 2,5-positions. For instance, by adding oligothiophenes of increasing length on the DPP core, the absorption is broadened while the band gap is decreased. The first DPP-based oligothiophene materials with PCBM achieved PCE of 2.3%.⁷¹ The OPV device performance of DPP-based materials was further improved by replacing terminal bithiophene with benzofuran.⁷² The benzofuran substituent increases intermolecular interaction through the high conjugation and stabilizes the molecules HOMO due to the

electronegative oxygen atom. When blended with PC₇₁BM, an optimized device efficiency of 4.4%.

A variety of other dye molecules have demonstrated to be a successful approach to donor materials. Merocyanine (MC) class of chromophore offer high absorption coefficients and sufficiently large variability in the position of the HOMO and LUMO levels.^{73,74} In case of developed MC-based material, the optimized OPV device showed a PCE of 4.5% due to the forms *in situ* driven by dipolar intermolecular forces when mixing two merocyanine dyes with complementary absorption as double-donors with C₆₀ acceptor.⁷⁵ Squaraine (SQ) dye-based molecules have been used to OPVs based on the advantages of high absorption coefficient, good photochemical and thermal stability.^{76,77} By optimizing morphology and molecular ordering of the modified SQ dye-based material:PC₇₁BM, a peak PCE of 5.5% has been achieved when the exciton diffusion length is approximately equal to the crystallite size.⁷⁷ Typical used push-pull structures have summarized in **Table 2.1**, including the structure shape, optoelectronic properties, and figure of merits of OPV. The general strategy of push-pull structure is that 1). Increasing the number of π -conjugation length, 2). Increasing (or strong) the number of electron withdrawing groups (or electron donating groups) in this series of compounds caused a decrease in the band gap. In 2007, D-A-D dyes based on carbazole or phenothiazine as a push unit and malononitrile as pull moiety were reported. Stronger electron-donating ability was observed from phenothiazine, evidenced by red-shifted intramolecular charge transfer absorption band and the OPV device showed a PCE value of 0.9%.⁷⁸ A star-shaped materials based on benzothiadiazole (BT) with triphenylamine (TPA) were further improved to 4.9% better PCE value in OPV devices.⁷⁹ An interesting phenomenon is that breaking the symmetry of the donor structure can lead to a

significant increase of V_{oc} , which may be attributed to the intermolecular interactions and molecular orientation. In 2015, seven thiophene unit as a π -linker, and rhodanine at its both ends as electron withdrawing moiety was achieved PCE of 9.3% due to the an optimized nanoscale interpenetrating donor/acceptor molecules network and the use of an efficient electron transport layer.⁶⁵ As a general trend with most of the push-pull structure, the V_{oc} tends to be higher than that observed in analogous polymer devices, while the FF and J_{sc} are usually lower. Examining the light versus dark current curves for most of the devices shows that the photocurrent becomes significantly larger at reverse bias. These points seem to imply that carrier extraction and recombination limit current generation in terms of the morphology of molecular heterojunction in thin film. Therefore, in the case of push-pull dyes, it appears that relatively high efficiencies can be obtained using a simple architecture but structurally induced recombination losses must be minimized through morphology control to realize highly efficient OPV devices.

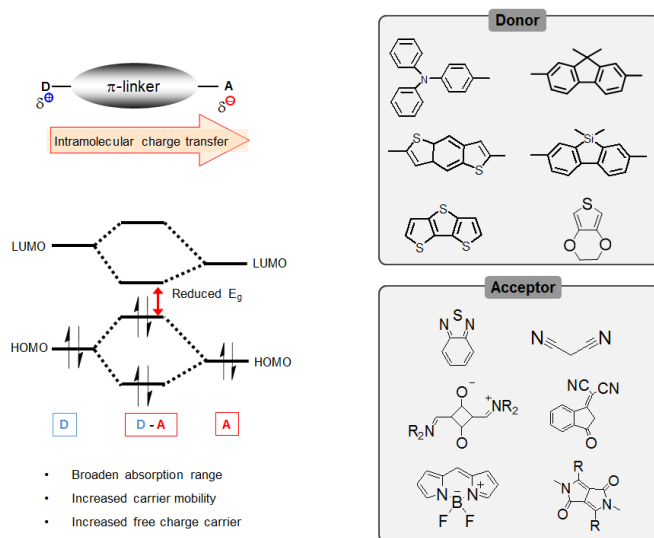


Fig. 2.6. A variety of push-pull structure of small molecules moieties

Table 2.1. Push-pull structures of small molecules

Architecture	Push moiety	π -linker	Pull moiety	HOMO (eV)	LUMO (eV)	$\lambda_{\text{max_abs}}$ Flim (nm)	V_{oc} (V)	J_{sc} (mA/cm ²)	PCE (%)	Ref
	triphenyl amine	Thienovinyl thiophene	indanedione	-	-	680 419	0.66	4.10	0.81	<i>J. Am. Chem. Soc.</i> , 2006, 128, 3459
	carbazole	diene	dicyano-vinyl	-5.47	-3.42	600 475	0.72	2.2	0.51	<i>Synth Met.</i> 2007, 157, 502
	triphenyl amine	divinyl-benzene	malonitrile	-5.14	-2.76	620 498	0.90	2.14	0.79	<i>J. Phys. Chem. C</i> , 2007, 111, 8661
	triphenyl amine	vinyl	benzothiadiazole	-5.28	-3.45	610 500	0.98	4.16	1.5	<i>J. Phys. Chem. C</i> , 2009, 113, 12911
	triphenyl amine	vinyl	benzothiadiazole	-5.19	-3.08	630 529	0.85	8.58	2.69	<i>Macromolecules</i> , 2009, 42, 7619
	triphenyl amine	thiophene	benzothiadiazole	-5.4	-3.3	590 508	0.92	4.9	1.8	<i>Chem. Mater.</i> , 2009, 21, 5327
	aminothiophene	-	malonitrile	-5.69	-3.54	640 595	1.0	10.2	4.5	<i>Angew. Chem. Int. Ed.</i> , 2011, 50, 11628
	benzofuran	thiophene	diketopyrrolopyrrole	-5.2	-5.2	710 595	0.92	10.0	4.4	<i>Adv. Funct. Mater.</i> , 2009, 19, 3063

2.5. Introduction of Device Architectures for Organic Photovoltaics

Since excitons of organic semiconductors are the Frenkel exciton, large driving force is required an energetic offset to dissociate excitons into free charge carriers. The generation of free charge carriers were primarily limited by the exciton diffusion length, and generated at the donor/acceptor interface.^{39,52} To overcome this limitation, Tang introduced the *planar heterojunction* (PHJ) type in 1986.⁸⁰ A thin donor layer is deposited on hole transport layer (HTL) by spin casting or blade coating or evaporation of organic semiconductors. On top of this layer a thin film of acceptor layer is formed, resulting in a layered structure with a well-defined planar interface. Finally a metal with a low work function like aluminum or calcium is deposited in order to extract of electrons form the LUMO of the acceptor molecule in **Fig. 2.7(a)**. The PHJ type showed impressive

photocurrent density and high PCE compared single layer device, owing to the much more efficient free charge generation process. However, photoactive layer must be thin within several tens of nanometers due to the low exciton diffusion lengths of organic semiconductors, which are on the order of a few nanometers. Excitons generated far from donor/acceptor interface (junction) cannot diffuse to reach the junction so that they are lost for charge generation owing to recombination process. For the reason, the main limitation of simple PHJ type is insufficient light harvesting due to only a fraction of the incident photons can be converted to charge carriers. The *bulk heterojunction* (BHJ) type was reported by Yu *et al.* in 1995 for the increasing donor/acceptor interfacial area in **Fig. 2.7(b)**.⁸¹ The BHJ type means mixed films with donor and acceptor molecules in photoactive layer by co-evaporation of donor and acceptor molecules or by deposition of a mixed thin film from a blended solution that contains donor and acceptor molecules. Typically BHJ thin layer have a thickness on the order of 100–200 nm, i.e. a factor of 10 or higher than the typical exciton diffusion lengths. Exciton dissociation is highly efficient since a large fraction of excitons encounters a donor/acceptor interface during their lifetime due to the smaller domains of donor (or acceptor) molecules than exciton diffusion length. Therefore, morphology of photoactive layer is very important because photocurrent generation relies on a balance between charge generation and transport, limited by phase separation between donor and acceptor. Although phase separation with small domain guarantee efficient charge generation, the charge carriers can cause bimolecular recombination by regeneration CT state at interface before being to collect at electrode.

This dissertation is expected to contribute to enhance the efficiency of organic optoelectronic devices based on the experimental results on the characteristics of organic semiconductors and organic photovoltaic devices.

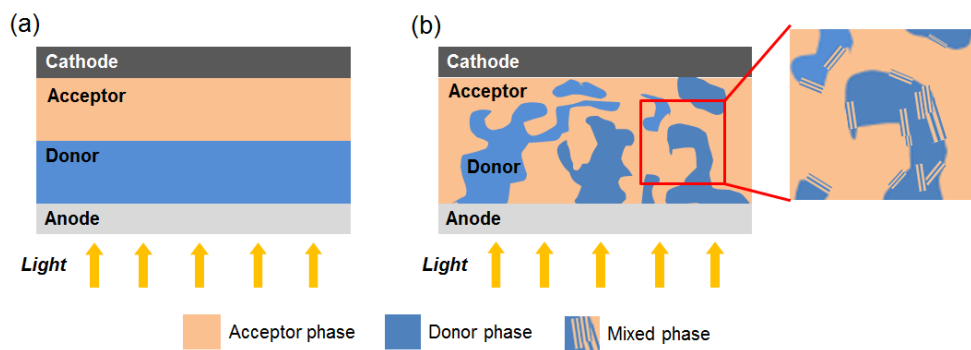


Fig. 2.7. Schematic side view of (a) an organic planar heterojunction structure and (b) bulk heterojunction structure

3. References and Notes

- 1). W. P. Su, J. R. Schrieffer and A. J. Heeger, *Phys. Rev. Lett.* **1979**, *42*, 1698.
- 2). J. L. Bredas and G. B Street, *Acc. Chem. Res.* **1985**, *18*, 309.
- 3). J. Zaumseil and H Sirringhaus, *Chem. Rev.* **2007**, *107*, 1296.
- 4). O. D. Jurchescu, J. Baas and T. T. M. Palstra, *Appl. Phys. Lett.* **2004**, *84*, 3061.
- 5). W. Warta and N. Karl, *Phys. Rev. B*, **1985**, *32*, 1172.
- 6). D. Fichou, *J. Mater. Chem.*, **2000**, *10*, 571.
- 7). E. Frankevich, Y. Maruyama, H. Ogata, Y. Achiba and K. Kikuchi, *Solid State Commun.*, **1993**, *88*, 177.
- 8). T. M. Clarke and J. R. Durrant. *Chem. Rev.*, **2010**, *110*, 6736.
- 9). J. Y. Kim, K. Lee, N. E. Coates, D. Moses, T.-Q. Nguyen, M. Dante and A. J. Heeger, *Science*, **2007**, *317*, 222.
- 10). C. W. Tang, *Appl. Phys. Lett.*, **1986**, *48*, 183.
- 11). A. Bernanose, M. Comte and P. Vouaux, *J. Chim. Phys.*, **1953**, *50*, 64.
- 12). H. Kallmann and M. Pope, *Nature*, **1960**, *186*, 31.
- 13). H. Koezuka, A. Tsumura and T. Ando, *Synthetic Metals.*, **1987**, *18*, 699.
- 14). H. Klauk, *Chem. Soc. Rev.*, **2010**, *39*, 264.
- 15). Q. Zhang, Y. Sun, W. Xu, and D. Zhu, *Energy&Environmental Science*, **2012**, *5*, 9639.
- 16). M. Scholdt, H. Do, J. Lang, A. Gall, A. Colsmann, U. Lemmer, J. D. Koenig, M. Winkler and H. Boettner, *J. Electro. Mater.*, **2010**, *39*, 1589.
- 17). O. Ostroverkhova. *Chem. Rev.* **2016**, *116*, 13279.
- 18). C. J. Bardeen, *Annu. Rev. Phys. Chem.*, **2014**, *65*, 127.
- 19). N. J. Hestand, R. Tempelaar, J. Knoester, T. L. C. Jansen and F. C Spano, *Phys. Rev. B: Condens. Matter Mater. Phys.* **2015**, *91*. 195315.

- 20). K. P. C. Vollhardt and N. E. Schore, *Organic Chemistry*, W. H. Freeman, **2010**.
- 21). G. G. Hall, *Advances in Quantum Chemistry*. **1929**, 22.
- 22). R. S. Mulliken, (1972) *Spectroscopy, Molecular Orbitals, and Chemical Bonding*, Nobel Lectures, Chemistry 1963–1970. Amsterdam: Elsevier *Publishing Company*.
- 23). F. C. Spano, *Acc. Chem. Res.*, **2010**, 43, 429.
- 24). F. C. Spano, C. Silva, *Annu. Rev. Phys. Chem.*, **2014**, 65, 47.
- 25). F. C. Spano, *Acc. Chem. Res.*, 43, 429.
- 26). G. D. Scholes, *Annu. Rev. Phys. Chem.*, **2003**, 54, 57.
- 27). A. P. Demchenko. *Introduction to Fluorescence Sensing*, volume 1. Springer, **2009**
- 28). J.-S. Huang, T. G. X. Li, M. Y. Sfeir, E. A. Bielinski, S. Tomasulo, M. L. Lee, N. Hazari and A. D. Taylor, *Nature Photonics*, **2013**, 7, 479.
- 29). G. K. Mor, J. Basham, M. Paulose, S. Kim, O. K. Varghese, A. Vaish, S. Yoriya and C. A. Grimes, *ACS Nano Lett.*, **2010**, 10, 2387.
- 30). D. L. Dexter, *J. Chem. Phys.*, **2004**, 21, 836.
- 31). N. J. Turro, *Modern Molecular Photochemistry* (University Science Books, Mill Valley, CA, 1991).
- 32). M. R. Narayan and J. Singh, *Phys. Status Solidi C*, **2012**, 1.
- 33). H. Bässler and A. Köhler, *Charge transport in organic semiconductors. In Unimolecular and Supramolecular Electronics I*, 1–65. Springer, Berlin-Heidelberg, **2012**.
- 34). M. Pope and C. E. Swenberg, *Electronic Processes in Organic Crystals and Polymers*. Oxford, 2 edition, 1999.

- 35). E. A. Silinsh and V. Čápec, *Organic Molecular Crystals: Interaction, Localization and Transport Phenomena; American Institute of Physics*, New York, 1994.
- 36). T. Holstein, *Ann. Phys.* **1959**, 8, 325.
- 37). T. Holstein, *Ann. Phys.* **1959**, 8, 343.
- 38). V. Coropceanu, J. Cornil, D. A. da S. Filho, Y. Oliver, R. Silbey and J.-L. Brédas, *Chem. Rev.*, **2007**, 107, 926.
- 39). K. M. Pelzer and S. B. Darling, *Mol. Syst. Des. Eng.*, **2016**, 1, 10.
- 40). R. A. Marcus, *Rev. Mod. Phys.*, **1993**, 65, 599.
- 41). L. Onsager, *Phys. Rev.*, **1938**, 54, 554.
- 42). V. D. Mihailetschi, L. J. A. Koster, J. C. Hummelen and P. W. M. Blom, *Phys. Rev. Lett.*, **2004**, 93, 216601.
- 43). G. Nan, X. Zhang and G. Lu, *J. Phys. Chem. C*, **2015**, 119, 15028.
- 44). X.-Y. Zhu, Q. Yang and M. Muntwiler, *Acc. Chem. Res.*, **2009**, 42, 1779.
- 45). H. Bässler and A. Köhler, *Phys.Chem.Chem.Phys.*, **2015**, 17, 28451.
- 46). J. Nelson. *The Physics of Solar Cells*. Imperial College Press, **2007**
- 47). J. X. Tang, C. S. Lee and S. T. Lee, *J. Appl. Phys.*, **2007**, 101, 064504.
- 48). R. A. Marcus, *Rev. Mod. Phys.*, **1993**, 65, 599.
- 49). Y. Zhao and W.-Z. Liang, *Chem. Soc. Rev.*, **2012**, 41, 1075.
- 50). C. LEng, H. Qin, Y. Si and Y. Zhao, *J. Phys. Chem. C*, **2014**, 118, 1843.
- 51). J.-I. Fujisawa, *Phys.Chem.Chem.Phys.*, **2015**, 17, 12228.
- 52). A. A. Bakulin, A. Rao, V. G. Pavelyev, P. H. M. van Loosdrecht, M. S. Pshenichnikov, D. Niedzialek, J. Cornil, D. Beljonne and R. H. Friend, *Science*, **2012**, 335, 1340.
- 53). G. F. Burkhard, E. T. Hoke, Z. M. Beiley and M. D. McGehee, *J. Phys. Chem. C*, **2012**, 116, 26674.

- 54). C. L. Braun, *J. Chem. Phys.*, **1984**, *80*, 4157.
- 55). T. Offermans, S. C. J. Meskers and R. A. J. Janssen, *Chem. Phys.*, **2005**, *125*, 3684.
- 56). A. W. Kohn, D. P. McMahon, S. Wen and T. V. Voorhis, *J. Phys. Chem. C*, **2017**, *121*, 26629.
- 57). A. A. Bakulin, S. D. Dimitrov, A. Rao, P. C. Y. Cjow, C. B. Nielsen, B. C. Schroeder, I. McCulloch, H. J. Bakker, J. R. Durrant and R. H. Friend, *J. Phys. Chem. Lett.*, **2013**, *4*, 209.
- 58). K. R. Graham, G. O. Ndjawa, S. M. Conron, R. Munir, K. Vandewal, J. J. Chen, S. Sweetnam, M. E. Thompson, A. Salleo, M. D. McGehee and A. Amassian, *Adv. Energu. Mater.*, **2016**, *6*, 1601211.
- 59). S. D. Dimitrov, A. A. Bakulin, C. B. Nielsen, B. C. Schroeder, J. Du, H. Bronstein, I. McCulloch, R. H. Friend and J. R. Durrant, *J. Am. Chem. Soc.*, **2012**, *134*, 18189.
- 60). P. Peumans, S. R. Forrest, *Chem. Phys. Lett.*, **2004**, *398*, 27.
- 61). N. Cho, C. W. Schlenker, K. M. Knesting, P. Koelsch, H-L. Yip, D. S. Ginger and A. K.-Y. Jen, *Adv. Energu. Mater.*, **2014**, *4*, 1301857.
- 62). S. Verlaak, D. Beljonne, D. Cheyns, C. Rolin, M, Linares, F. Castet, J. Cornil and P. Heremans, *Adv. Funct. Mater.*, **2009**, *19*, 3809.
- 63). A. J. Kupijai, K. M. Behringer, M. Corazza, S. A. Gevorgyan, F. C. Krebs, M. Stutzmann and M. S. Brandt, *Phys. Rev. B*, **2015**, *92*, 1.
- 64). F. Etzold, I. A. Howard, N. Forler, A. Melnyk, D. Andrienko, M. R. Hansen and F. Laquai, *Energy. Environ. Sci.*, **2015**, *8*, 1511.
- 65). Q. Zhang, B. Kan, F. Liu, G. Long, X. Wan, X. Chen, Y. Zuo, W. Ni, H. Zhang, M. Li, Z. Hu, F. Huang, Y. Cao, Z. Liang, M. Zhang, T. P. Russell and Y. Chen, *Nature Photon.*, **2015**, *9*, 35.

- 66). Y. Rout, R. Misra, R. Singhal, S. Biswas and G. D. Sharma, *Phys. Chem. Chem. Phys.*, **2018**, *20*, 6321.
- 67). Y. Sun, G. C. Welch, W. L. Leong, C. J. Takacs, G. C. Bazan and A. J. Heeger, *Nature Mater.*, **2012**, *11*, 44.
- 68). Y. Liu, C.-C. Chen, Z. Hong, J. Gao, Y. Yang, H. Zhou, L. Dou, G. Li and Y. Yang, *Sci. Rep.*, **2013**, *3*, 3356.
- 69). Y. Shirota and H. Kageyama, *Chem. Rev.*, **2007**, *107*, 953.
- 70). Z. Ning and H. Tian, *Chem. Commun.*, **2009**, *0*, 5483.
- 71). A. B. Tamayo, B. Walker and T.-Q. Nguyen, *J. Phys. Chem. C*, **2008**, *2*, 11545.
- 72). B. Walker, A. B. Tamayo, X. D. Dang, P. Zalar, J. H. Seo, A. Garcoa, M. Tantiwivat and T.-Q. Nguyen, *Adv. Funct. Mater.*, **2009**, *19*, 3063.
- 73). N. M. Kronenberg, M. Deppisch, F. Würthner, H. W. A. Lademann, K. Deing and K. Meerholz, *Chem. Commun.*, **2008**, 6489.
- 74). H. Bückstümmer, N. M. Kronenberg, M. Gsänger, M. Stolte, K. Meerholz and F. Würthner, *J. Mater. Chem.*, **2010**, *20*, 240.
- 75). H. Bückstümmer, E. V. Tulyakova, M. Deppisch, M. R. Lenze, N. M. Kronenberg, M. Gsänger, M. Stolte, K. Meerholz and F. Würthner, *Angew. Chem., Int. Ed.*, **2011**, *50*, 11628.
- 76). G. Wei, S. Wang, K. Sun, M. E. Thompson and S. R. Forrest, *Adv. Energy Mater.*, **2011**, *1*, 184.
- 77). U. Mayerhöffer, K. Deing, K. Größ, H. Braunschweig, K. Meerholz and F. Würthner *Angew. Chem., Int. Ed.*, **2009**, *48*, 8776.
- 78). C. He, Q. He, X. Yang, G. Wu, C. Yang, F. Bai, Z. Shuai, L. Wang and Y. Li, *J. Phys. Chem. C*, **2007**, *111*, 8661.

- 79). W. Li, C. Du, F. Li, Y. Zhou, M. Fahlman, Z. Bo and F. Zhang, *Chem. Mater.*, **2009**, *21*, 5327.
- 80). C. W. Tang, *Appl. Phys. Lett.*, **1986**, *48*, 183.
- 81). J. J. M. Halls, C. A. Walsh, N. C. Greenham, E. A. Marseqlia, R. H. Friend, S. C. Moratti and A. B. Holmes, *Nature*, **1995**, *376*, 498.

**Part II. Studies on Small Molecules and Carbon Dots
on Light Harvesting of Organic Photovoltaic Devices**

Section 1. Effect of π -Linker on the Performance of Organic Photovoltaic Devices Based on Push-Pull D- π -A Molecules

Abstract

Two push-pull D- π -A molecules, **3T** and **DTT** as donor materials, were synthesized and characterized for solution-processed bulk heterojunction (BHJ) organic photovoltaic (OPV) devices. The π -linker plays a vital role not only in electrochemical and thermal properties but also affects the thin film morphology of **3T** and **DTT**. **3T** showed the high electrochemical stability with a faster electrode reaction rate. The solution-processed OPV devices based on **3T** showed higher power conversion efficiencies than **DTT**-based devices because of its superior electrochemical properties.

Keywords: push-pull structure, bulk heterojunction, organic photovoltaic, electrochemical stability, photo conversion efficiency

1 Introduction

Solution-processed organic photovoltaic (OPV) devices have drawn much attention because of their simplicity and low cost in large area fabrication process.¹⁻³ Although the power conversion efficiency (PCE) of OPV devices is lower than that of inorganic solar cells, small molecule-based OPV materials have great potential in terms of their versatility of structural variations and tunable optical and electrical properties.^{1,4} A key feature of OPV materials mainly depends on the π -conjugated structure. Push-pull D- π -A molecules end-capped with an electron donor and an electron acceptor can have a low-energy band gap as well as a broad absorption range resulting from intramolecular charge transfer.⁵⁻⁸ In fact, the structure of the π -linker has considerable effect on the optical and electronic properties of donor-acceptor push-pull molecules with a π -linker.^{9,10} However, relatively little attention has been paid to the relationship between the π -linker and OPV device performance.

Herein, we report the effect of the π -linker on electrochemical, thermal and morphological properties of push-pull-type D- π -A molecules incorporating different π -linkers, where triphenylamine is employed as a donor moiety, and dicyanomethylene-appended indanone as an acceptor moiety, and terthiophene or dithienothiophene with two thiophene moieties at its both ends as a π -linker. Alkyl chains are introduced to the π -linker for solution-processed bulk heterojunction (BHJ) OPV devices. We also investigate the effect of the π -linker on the device performance of OPVs fabricated by blending the donor material with [6,6]-phenyl-C₇₁-butyric acid

methyl ester (PC₇₁BM) as the acceptor for the BHJ structure based active layer.

2 Experimental Methods

2.1 Reagents and Materials

All the chemical agents were used without further purification. Tetrakis(triphenylphosphine)palladium(0) (Pd(PPh₃)₄), Tris(dibenzylideneacetone)dipalladium(0) (Pd(dba)₃), 2,5-dibromothiophene, 2-(3-hexylthiophen-2-yl)-4,4,5,5-tetramethyl-1,3,2-dioxaborolane, 2-(3-oxo-2,3-dihydro-1H-inden-1-ylidene)malononitrile were purchased from Toyko Chemical Industry (TCI). N-bromosuccinimide (NBS), tetrabutylammonium hexafluorophosphate (TBAPF₆), Phosphorus(V) oxychloride (POCl₃), 4-bromo-N,N-diphenylaniline, potassium carbonate (K₂CO₃), sodium bicarbonate (NaHCO₃) and N,N'-dimethylformamide (DMF) were purchased from Sigma-Aldrich and SAMCHUN. Poly(3,4-ethylenedioxythiophene)-poly(styrenesulfonate) (PEDOT:PSS, P) was purchased from Baytron.

2.2 Synthetic procedure

2,6-Dibromodithieno[3,2-b:2',3'-d]thiophene (compound 3) was prepared according to the literature procedure.¹¹

2,6-bis(3-hexylthiophene-2-yl)dithieno[3,2-b:2',3'-d]thiophene (compound 4). A mixture of compound 3 (2 g, 5.65 mmol), 2-(3-hexylthiophene-2-yl)-4,4,5,5-tetramethyl-1,3,2-dioxaborolane (3.5 ml, 11.9 mmol), tris(dibenzylideneacetone)dipalladium(0) (Pd₂(dba)₃, 0.175 g, 0.17 mmol), tri-*tert*-

butylphosphonium tetrafluoroborate ($[(t\text{-Bu})_3\text{P}]\text{BF}_4$, 0.098 g, 0.34 mmol) and K_2CO_3 (20 ml, 2M) in THF (55 ml) was heated at 100 °C for 48 h. The reaction mixture was cooled to room temperature (RT) and NH_4Cl (10 ml) was added. The reaction mixture was concentrated under vacuum and was extracted with ethyl acetate. The organic phase was washed with water and brine, and dried over anhydrous MgSO_4 . Volatiles were evaporated and the resulting crude product was purified by column chromatography on silica gel using hexane as eluent to give orange oil product (yield: 1.30 g, 65%). ^1H NMR (300 MHz, CDCl_3 , ppm) δ : 7.32 (s, 2H), 7.25 (d, 2H, 5.4 Hz), 7.00 (d, 2H, 5.4 Hz), 2.84 (t, 4H, 7.5 Hz), 1.70 (m, 4H), 1.36 (m, 14 H), 0.92 (t, 4H, 6.6 Hz).

4-hexyl-5-(6-(3-hexylthiophene-2-yl)dithieno[3,2-b:2'3'-d]thiophen-2-yl)thiophene-2-carbaldehyde (compound 5). DMF (0.41 ml, 5.3 mmol) and POCl_3 (0.23 ml, 2.5 mmol) were added to a solution of compound **4** (1.11g, 2.1 mmol) in distilled 1,2-dichloroethane (40 ml) cooled in an ice bath. The reaction mixture was stirred at RT for 10 h. Precipitates formed were filtered using a Büchner funnel, washed with hexane to give the orange solid. The crude product was purified by column chromatography on silica gel using dichloromethane and hexane (0.4:1 v/v) to give orange solid product (yield: 0.68 g, 61%). ^1H NMR (300 MHz, CDCl_3 , ppm) δ : 9.87 (s, 1H), 7.65 (s, 1H), 7.49 (s, 1H), 7.33 (s, 1H), 7.27 (d, 1H, 5.4 Hz), 7.00 (d, 1H, 5.1 Hz), 2.86 (m, 4H), 1.69 (m, 4H), 1.35 (m, 12H), 0.92 (m, 6H).

5-(6-(5-bromo-3-hexylthiophene-2-yl)dithieno[3,2-b:2'3'-d]thiophen-2-yl)-4-hexylthiophene-2-carbaldehyde (compound 6). To a solution of compound **5** (0.457 g, 0.73 mmol) in CHCl_3 (25 ml) cooled in an ice bath was slowly added AcOH (25 ml). The reaction mixture was treated with NBS (0.285 g, 1.6 mmol)

and stirred for 7 h. The reaction mixture was treated with aqueous solution of NaOH (25 ml, 1 M), stirred in an ice bath for 1 h, then concentrated under vacuum, and extracted with dichloromethane. The organic phase was washed with water and brine, and dried over anhydrous MgSO₄. Volatiles were evaporated and the crude product was purified by column chromatography on silica gel using dichloromethane to give reddish solid product (yield: 0.320 g, 70%). ¹H NMR (300 MHz, CDCl₃, ppm) δ: 9.87 (s, 1H), 7.64 (s, 1H), 7.48 (s, 1H), 7.28 (s, 1H), 6.95 (s, 1H), 2.87 (t, 2H, 15.3 Hz), 2.76 (t, 2H, 14.7 Hz), 1.68 (m, 4H), 1.34 (m, 12 H), 0.92 (m, 6H).

***N,N*-diphenyl-4-(4,4,5,5-tetramethyl-1,3,2-dioxaborolan-2-yl)aniline (compound 7).** *n*-Butyllithium (8.5 ml, 1.6 M in hexanes) was slowly added to a solution of 4-bromo-*N,N*-diphenylaniline (2g, 6.17 mmol) in distilled THF (40 ml) under a nitrogen atmosphere cooled at -70 °C (dry ice/isopropanol). After 90 min, 2-isopropoxy-4,4,5,5-tetramethyl-1,3,2-dioxaborolane (2.53 g, 13.57 mmol) was added dropwise via syringe. The reaction mixture was stirred overnight and then treated with water (20 ml). The resulting mixture was extracted with dichloromethane. The organic phase was washed with water and brine, and dried over anhydrous MgSO₄. Volatiles were evaporated and the resulting residue was purified by column chromatography on silica gel using dichloromethane and hexane (1:5 v/v) to give white solid product (yield: 1.57 g, 79 %). ¹H NMR (300 MHz, acetone-d₆, ppm) δ: 7.63 (d, 2H, 8.4 Hz), 7.34 (t, 4H, 15.6 Hz), 7.11 (m, 6H), 6.98 (d, 2H, 8.4 Hz), 1.33 (s, 12H).

5-(6-(5-(4-(diphenylamino)phenyl)-3-hexylthiophene-2yl)dithieno[3,2-b:2'3'-d]thiophen-2-yl)-4-hexylthiophene-2-carbaldehyde (compound 8).

A mixture of compound **7** (0.192 g, 0.52 mmol), compound **6** (0.3 g, 0.47 mmol), Pd(PPh₃)₄ (0.033 g, 0.028 mmol) and NaHCO₃ (0.593 g, 7.06 mmol) in THF and H₂O (24 ml/8 ml, 3:1 v/v) was refluxed for 24 h. The reaction mixture was concentrated under vacuum and was extracted with dichloromethane. The organic phase was washed with water and brine, and dried over anhydrous MgSO₄. Volatiles were evaporated and the residue was purified by column chromatography on silica gel using dichloromethane and hexane (1:3 v/v) to give orange yellow solid product (yield: 0.132 g, 69 %). ¹H NMR (300 MHz, acetone-d₆, ppm) δ: 9.92 (s, 1H), 7.92 (s, 1H), 7.62 (d, 2H, 2.9 Hz), 7.44 (d, 1H, 3.9 Hz), 7.33 (m, 6H), 7.13 (d, 5H, 8.1 Hz), 7.06 (d, 3H, 8.7 Hz), 2.85 (t, 2H, 11.7 Hz), 2.81 (t, 2H, 11.7 Hz), 1.76 (m, 4H), 1.33 (m, 12H), 0.90 (m, 6H).

(Z)-2-(2-((5-(6-(5-(4-(diphenylamino)phenyl)-3-hexylthiophen-2-yl)dithieno[3,2-b:2',3'-d]thiophen-2-yl)-4-hexylthiophen-2-yl)methylene)-3-oxo-2,3-dihydro-1H-inden-1-ylidene)malononitrile

(DTT). To a solution of compound **8** (0.230 g, 0.29 mmol) in EtOH (25 ml) at 60 °C was added dropwise 2-(3-oxo-2,3-dihydro-1H-inden-1-ylidene)malononitrile (0.089 g, 0.46 mmol) in THF (3 ml). The reaction mixture was stirred overnight at the same temperature, cooled to RT, concentrated under vacuum, and the residue was treated with dichloromethane and ethanol to isolate the crude product as precipitates, which was further purified by column chromatography on silica gel using dichloromethane to give dark green solid product (yield: 0.15 g, 53%). ¹H NMR (300 MHz, CDCl₃, ppm) δ: 8.57 (s, 1H), 8.51 (d, 1H, 7.0 Hz), 7.86 (d, 1H, 6.3 Hz), 7.66 (m, 2H), 7.48 (s, 2H), 7.33 (m, 6H), 7.17 (d, 5H, 6.9 Hz),

7.07 (m, 5H), 6.96 (s, 1H), 2.78 (t, 2H, 15.6 Hz), 2.70 (t, 2H, 15.5 Hz), 1.66 (m, 4H), 1.40 (m, 12H), 0.96 (m, 6H). ^{13}C NMR (75 MHz, CDCl_3 , ppm) δ : 160.17, 148.54, 147.39, 141.76, 141.47, 140.75, 139.94, 139.23, 136.83, 135.38, 134.99, 134.53, 134.35, 129.36, 127.51, 126.33, 125.33, 125.21, 124.68, 123.40, 123.28, 122.27, 121.22, 118.23, 114.62, 69.20, 31.73, 31.65, 30.45, 29.96, 29.82, 29.52, 29.39, 29.36, 22.65, 14.13. HRMS (FAB) m/z : calcd $\text{C}_{59}\text{H}_{49}\text{N}_3\text{OS}_5$ 975.2479, $[\text{M}+\text{H}]^+$: observed 976.2549. Elemental analysis calc.: C, 72.58; H, 5.09; N, 4.30; O, 1.64; S, 16.42; found: C, 72.60; H, 4.85; N, 4.08, O, 1.92; S, 16.54.

3,3''-dihexyl-2,2':5',2''-terthiophene (compound 9). A mixture of 2,5-dibromothiophene (1 g, 4.13 mmol), 2-(3-hexylthiophen-2-yl)-4,4,5,5-tetramethyl-1,3,2-dioxaborolane (2.58 ml, 8.67 mmol), $\text{Pd}(\text{PPh}_3)_4$ (0.3 mg, 0.26 mmol), and K_2CO_3 (16.5 ml, 2M) in THF (30 ml) was heated at 100 °C for 48 h. The reaction mixture was cooled to RT and treated with NH_4Cl (10 ml). The solvent was evaporated under vacuum and the resulting mixture was extracted with ethyl acetate. The organic phase was washed with water and brine, and dried over anhydrous MgSO_4 . Volatiles were evaporated and the crude product was purified by column chromatography on silica gel using hexane to give orange oil product (yield: 0.78 g, 78%). ^1H NMR (300 MHz, CDCl_3 , ppm) δ : 7.16 (d, 1H, 1.4 Hz), 7.04 (s, 1H). 6.93 (d, 1H, 1.3 Hz), 2.77 (t, 2H, 3.7 Hz), 1.63 (m, 2H), 1.30 (m, 6H), 0.87 (t, 3H, 3.5 Hz).

5-bromo-3,3''-dihexyl-2,2':5',2''-terthiophene (compound 10). To a solution of compound 9 (0.65 g, 2.1 mmol) in CHCl_3 (20 ml) cooled in an ice bath was slowly added AcOH (20 ml). The reaction mixture was treated with NBS (0.412 g, 2.3 mmol) and stirred for 5 h. The reaction mixture was

treated with aqueous solution of NaOH (25 ml, 1 M), stirred in an ice bath for 1 h, then concentrated under vacuum, and extracted with dichloromethane. The organic phase was washed with water and brine, and dried over anhydrous MgSO₄. All volatiles were evaporated and the crude product was purified by column chromatography on silica gel using dichloromethane to give orange oil product (yield: 0.335 g, 52%). ¹H NMR (400 MHz, DMSO-d₆, ppm) δ: 7.45 (d, 1H, 5.2 Hz), 7.15 (s, 1H), 7.12 (q, 2H, 16.4 Hz), 7.00 (d, 1H, 5.2 Hz), 2.68 (m, 4H), 1.52 (m, 4H), 1.23 (m, 12 H), 0.80 (t, 6H, 13.6 Hz).

5''-bromo-3,3''-dihexyl-[2,2':5,2''-terthiophene]-5-carbaldehyde (compound 11). DMF (0.15 ml, 2.0 mmol) and POCl₃ (0.09 ml, 0.9 mmol) were added to a solution of compound **10** (0.39g, 0.79 mmol) in distilled dichloromethane (25 ml) cooled in an ice bath. The reaction mixture was stirred at RT for 2 h and then heated at 60°C for 10 h. The reaction mixture was cooled to RT, treated with NaOAc (7.9 ml, 2 M), and stirred for 2 h. Volatiles were evaporated under vacuum and the resulting residue was extracted with dichloromethane. The organic phase was washed with water and brine, and dried over anhydrous Na₂SO₄. The crude product was purified by column chromatography on silica gel using dichloromethane and hexane (1:1 v/v) to give orange red solid product (yield: 0.29 g, 74 %). ¹H NMR (300 MHz, acetone-d₆, ppm) δ: 9.92 (s, 1H), 7.91 (s, 1H), 7.42 (d, 1H, 1.3 Hz), 7.26 (d, 1H, 1.3 Hz), 7.16 (s, 1H), 2.93 (t, 2H, 3.1 Hz), 2.73 (t, 2H, 3.1 Hz), 1.70 (m, 2H), 1.63 (m, 2H), 1.37 (m, 14H), 0.89 (t, 6H, 6.8 Hz).

5''-(4-(diphenylamino)phenyl)-3,3''-dihexyl-[2,2':5,2''-terthiophene]-5-carbaldehyde (compound 12). A mixture of compound **7** (0.28 g, 0.75

mmol), compound **11** (0.22 g, 0.42 mmol), Pd(PPh₃)₄ (0.03 g, 0.025 mmol) and NaHCO₃ (0.53 g, 6.32 mmol) in THF and H₂O (21 ml/7 ml, 3:1 v/v) was refluxed for 24 h. The reaction mixture was cooled to RT and concentrated under vacuum and was extracted with dichloromethane. The organic phase was washed with water and brine, and dried over anhydrous MgSO₄. Volatiles were evaporated and the residue was purified by column chromatography on silica gel using ethyl acetate and hexane (1:35 v/v) to give orange yellow solid product (yield: 0.197 g, 70%). ¹H NMR (400 MHz, DMSO-d₆, ppm) δ: 9.8 (s, 1H), 7.9 (s, 1H), 7.55 (s, 1H), 7.53 (s, 1H), 7.42 (d, 1H, 4 Hz), 7.35 (s, 1H), 7.31 (m, 4H), 7.24 (d, 1H, 4Hz), 7.05 (m, 6H), 6.95 (d, 2H, 12.1 Hz), 2.80 (t, 2H, 15.6 Hz), 2.74 (t, 2H, 15.6 Hz), 1.62 (m, 12 H), 0.82 (t, 6H, 6.4 Hz).

(Z)-2-(2-((5''-(4-(diphenylamino)phenyl)-3,3''-dihexyl-[2,2':5,2''-terthiophene]-5-yl)methylene)-3-oxo-2,3-dihydro-1H-inden-1-ylidene)malonitrile (3T). To a solution of compound **12** (0.42 g, 0.61 mmol) in EtOH (15 ml) at 60 °C was added dropwise 2-(3-oxo-2,3-dihydro-1H-inden-1-ylidene)malononitrile (0.118 g, 0.61 mmol) in THF (10 ml). The reaction mixture was stirred overnight at the same temperature, cooled to RT, concentrated under vacuum, and the residue was treated with dichloromethane and ethanol to isolate the crude product as precipitates, which was further purified by column chromatography on silica gel using dichloromethane to give dark blue solid product (yield: 0.315 g, 60%). ¹H NMR (400 MHz, CDCl₃, ppm) δ: 8.77 (s, 1H), 8.66 (d, 1H, 7.6 Hz), 7.91 (d, 1H, 6.4 Hz), 7.73 (m, 2H), 7.64 (s, 1H), 7.45 (m, 3H), 7.27 (m, 4H), 7.16 (d, 1H, 0.9 Hz), 7.13 (m, 4H), 7.04 (m, 5H), 2.83 (m, 4H), 1.71 (m, 4H), 1.32 (m,

12 H), 0.90 (m, 6H). ^{13}C NMR (100 MHz, CDCl_3 , ppm) δ : 188.23, 180.97, 164.53, 160.74, 160.47, 159.08, 148.85, 148.12, 147.61, 147.34, 142.94, 141.68, 140.74, 140.35, 139.99, 137.40, 136.87, 135.04, 134.42, 134.27, 134.10, 134.02, 131.81, 131.43, 129.33, 128.87, 128.48, 128.18, 127.54, 126.63, 126.36, 126.02, 125.51, 125.25, 124.64, 123.70, 123.50, 123.37, 123.26, 122.13, 118.02, 114.66, 69.14, 31.70, 31.59, 30.40, 30.00, 29.88, 29.45, 29.30, 22.62, 22.59, 14.73, 14.09, 14.06. HRMS (FAB) m/z : calcd $\text{C}_{55}\text{H}_{49}\text{N}_3\text{OS}_3$ 863.3038, $[\text{M}+\text{H}]^+$: observed 864.3113. Elemental analysis calc.: C, 76.44; H, 5.72; N, 4.86; O, 1.85; S, 11.13; found: C, 76.45; H, 5.63; N, 4.81, O, 1.94; S, 11.16

2.3 Instrumentms

^1H and ^{13}C NMR spectra were recorded in CDCl_3 , acetone- d_6 or DMSO- d_6 using Avance 300 and 400 MHz Bruker spectrometer. Mass spectra were obtained using a GC-MS spectrometer (JEOL, JMS-700). The optical properties were characterized by absorption (Beckman, DU650) and photoluminescence (PL) spectra (Jasco, FP-7500 spectrophotometer). The electrochemical properties were obtained using the cyclic voltammetry (CV) (CH instruments, 650B electrochemical analyzer). The electrochemical cell consists of three electrodes (a reference electrode, Ag/Ag^+ 0.01 M, a counter electrode (Pt) and a working electrode (Pt)) in dichloromethane containing 0.1 mM **3T** or **DTT** as a redox material and tetrabutylammonium hexafluorophosphate (0.1 M TBAPF $_6$) as a supporting electrolyte. All potentials were calibrated using a ferrocene/ferrocenium (Fc/Fc^+) redox couple.¹² Density functional theory (DFT) calculations were performed to obtain HOMO/LUMO energy levels of **3T** and **DTT** using the Gaussian

B3LYP/6-31G (Gaussian 09 Rev. B01). Tapping mode atomic force microscopy (AFM) (Veeco, NanoScope IV) images were acquired using a scan rate of 1 Hz under ambient atmosphere. All the samples were prepared by spin-casting onto ITO/glass substrate. The film thickness of organic layers was measured using alpha-step (KLA Tencor). Thermal properties of the synthesized materials were obtained using a thermal gravimetric analyzer (TGA) (TA instruments, Q-5000 IR) and differential scanning calorimeter (DSC) (TA instrument, DSC-Q1000). Elemental analysis was performed (Thermo Fisher Scientific, Flash2000)

2.4 Organic Photovoltaic Devices Preparation

Device configuration of ITO/PEDOT:PSS/donor (**3T** or **DTT**):PC₇₁BM/LiF/Al was used to investigate the OPV device performance. Pre-patterned indium tin oxide (ITO, 13 ohm/sq) on glass was cleaned by carrying out sequential ultrasonication in deionized water (10 min), isopropyl alcohol (IPA) (10 min), followed by UV ozone treatment for 5 min. PEDOT:PSS (P) was spin-coated onto ITO to prepare the hole transport layer (HTL). Post-annealing process was conducted at 120 °C for 20 min. Photoactive layers were spin-coated from a mixture of chlorobenzene and chloroform (1:0.2 v/v) containing various weight ratios (1:1, 1:1.5, 1:1.75, 1:2 and 1:3) of each donor and PC₇₁BM in a glove box. Thermal annealing treatment was conducted for the photoactive layer thin films of **DTT**:PC₇₁BM (120 °C to 200 °C) Finally, LiF (1 nm) and Al (100 nm) were thermally evaporated under 10⁻⁶ torr as cathode electrode. The active area is 4 mm². A reference device was fabricated using 2.0 wt% of P3HT:PC₆₁BM (1:0.8 w/w) active layer in chlorobenzene solution in a glove box under the same conditions. PEDOT:PSS organogels with carbon dots (0.19 wt% @IPA) were prepared

shown in Scheme 1. To confirm electronic structures of **DTT** and **3T**, density functional theory (DFT) calculations were performed using the Gaussian B3LYP/6-31G (*Fig. 1*). The degree of overlap of **3T** between the highest occupied molecular orbital (HOMO) and the lowest unoccupied molecular orbital (LUMO) was more than that of **DTT**. This implies that **3T** has stronger intramolecular interaction than **DTT** due to better electronic coupling.^{14,15}

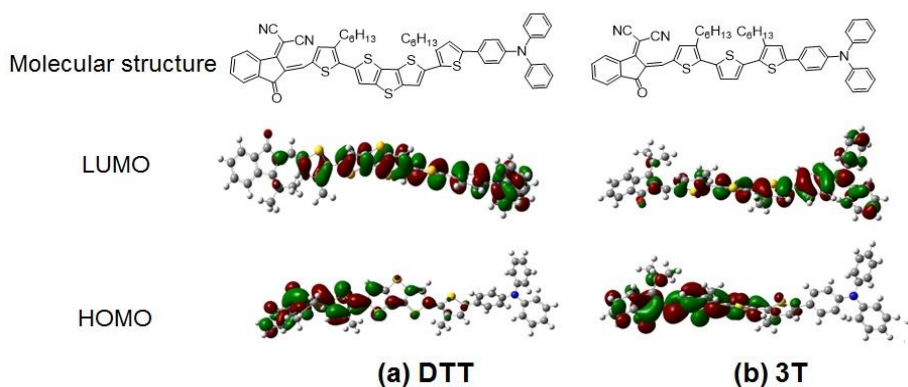


Fig. 1. HOMO and LUMO orbital density of (a) **DTT** and (b) **3T** from DFT calculations

3.2 Photophysical Properties

Optical properties of **3T** and **DTT** were investigated by UV/vis absorption spectroscopy in dichloromethane solution and in spin-cast thin film as shown in *Fig. 2(a)* and *Table 1*. The UV/vis spectra of both molecules in solution state exhibited almost the same absorption range and shape. The absorption peak at 300 nm was from $n-\pi^*$ electronic transition bands of the triphenylamine moiety. The

absorption peak at 380 nm was from π - π^* transition bands of the π -linker.¹⁶ The long wavelength region of the absorption peak around 605 nm would originate from intramolecular charge transfer between the donor and acceptor moieties. Compared to the solution state, the broad band and red-shifted absorption spectra were observed in spin-cast thin films due to stronger intermolecular interactions in the solid state. As expected, the thin film of **DTT** with a rigid dithienothiophene moiety showed stronger π - π interaction than the **3T** thin film, resulting in red shift of the π - π^* transition band from 393 nm to 462 nm. Atomic force microscopy (AFM) images revealed that the **DTT** thin film showed well-ordered nanostructure morphology, while the **3T** thin film showed less-ordered surface morphology (*Fig. 4(a)*). This means that the π -linker can affect the packing of D- π -A molecules in the thin films and the electronic transitions. As shown in *Fig. 2(b)*, the maximum absorption peak in the long wavelength region of **3T** was red-shifted (from 587 to 620 nm) with increasing solvent.¹⁷ The solvatochromic effect indicates that **3T** has higher dipole moments in the excited state.

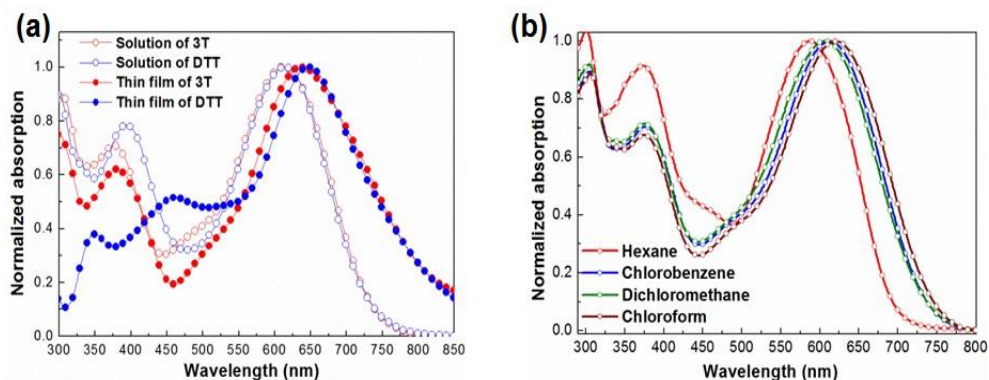


Fig. 2. Normalized UV/vis absorption spectra of (a) **3T** and **DTT** (open circle: solution state in CH_2Cl_2 , closed circle: thin film), and (b) **3T** in various solvents

3.3 Thermal Propertie

Thermal properties of **3T** and **DTT** were examined by differential scanning calorimetry (DSC) and thermogravimetric analysis (TGA) as shown in Table 1. **DTT** exhibited higher thermal stability than **3T**. The higher melting temperature (T_m) of **DTT** would suppress its degradation during thermal annealing processing of OPV devices. This result implies that the rigid dithienothiophene moiety in the π -linker of **DTT** can contribute to the thermal stability.¹⁸

Table 1 UV/vis spectral data, energy levels and thermal properties of **3T** and **DTT**

Molecules	Solution		Thin films	E_g^c	HOMO/LUMO ^d	TGA ^d (°C)	T_m^e (°C)
	λ_{max} (nm) ^a	λ_{abs} (max, nm) $Lmol^{-1}cm^{-1}$	λ_{max} (nm) ^b				
3T	607	3.9×10^4	637	1.68	5.14/3.46	309	170
DTT	607	1.7×10^4	647	1.65	5.08/3.43	305	208

^a Measured in dichloromethane solution. ^b Spin-cast thin film in dichloromethane. ^c Band gaps and ^d energy levels estimated from CV and absorption spectra. ^e temperature at 5% weight loss under nitrogen. ^e determined by DSC under nitrogen.

3.4 Electrochemical Properties

In order to investigate the electrode reaction rate and stability of redox couples of **3T** and **DTT**, electrochemical experiments were performed. Cyclic voltammetry (CV) showed two quasi-reversible oxidative potentials in both molecules in tetrabutylammonium hexafluorophosphate (0.1 M TBAPF₆) as a supporting electrolyte in dichloromethane solution at a scan rate of 0.05 V/s. The electrochemical data were presented in Table 2. Their HOMO and LUMO levels

were calculated from CV measurements and absorption spectra. The first oxidation potentials (E_{ox}°) of **3T** and **DTT**, estimated by the onset potential, were 0.34 and 0.28 eV, respectively versus the ferrocene/ferrocenium redox couple (Fc/Fc⁺).¹² The HOMO and LUMO energy levels of **3T** and **DTT** were almost identical. Redox reactions showed that the peak current ratio (i_{pc}/i_{pa}) and peak-to-peak separation (ΔE_{pp}) for **3T** were 0.86 and 0.09 V, whereas those for **DTT** were 0.54 and 0.09 V, respectively. This means that **3T** is more electrochemically stable than **DTT** during the oxidative process. Diffusion coefficient (D_o) and electrode reaction rate (k°) of **3T** and **DTT** were measured according to eq 1 by chronocoulometry.¹⁹

$$Q = \frac{2FAD_o^{1/2}C_o^*t^{1/2}}{\pi^{1/2}} \quad (1)$$

where Q is charge of an electrochemical reaction of the redox material, F is the Faraday constant, A is the electrode surface area, D_o and C_o^* are the diffusion coefficient and the concentration of the redox materials, respectively. The surface area (A) of the Pt disk electrode was determined using the known value of D_o , $2.4 \times 10^{-5} \text{ cm}^2 \text{ s}^{-1}$ of ferrocene and eq 1.¹⁹ The k° , related to electron transfer between the redox species and the electrode, was calculated from eq 2.²⁰

$$\psi = \frac{k^{\circ}}{\sqrt{\pi D_o v \left(\frac{F}{RT} \right)}} = f(\Delta E_p) \quad (2)$$

The parameters of mass transfer D_o and k° were summarized in Table 2. The D_o values of **3T** and **DTT** were similar, but the k° value of **3T** ($1.0 \times 10^{-1} \text{ cm}^{-1}$) was higher than that of **DTT** ($0.7 \times 10^{-1} \text{ cm}^{-1}$). This indicates that **3T** has faster electron transfer rate than **DTT**. These results support that the designed π -

linker do not affect the energy band gap (E_g , Table 1), but affect morphology properties in the solid state as well as electrochemical properties in the solution state. **3T** with a more stable redox state and faster k^0 is expected to improve the efficiency of OPV devices compared to **DTT**.²¹⁻²⁵

Table 2 Electrochemical data of **3T** and **DTT**^a

Molecules	oxidative process						D_o (cm^2s^{-1})	k^0 (cms^{-1})
	E_{ox}^0 (V)	$i_{\text{pc}}/i_{\text{pa}}$	ΔE_{pp} (V)	E_{ox}^0 (V)	$i_{\text{pc}}/i_{\text{pa}}$	ΔE_{pp} (V)		
3T	0.42	0.86	0.09	0.69	0.80	0.09	3.1×10^3	1.0×10^{-1}
DTT	0.37	0.54	0.09	0.59	0.95	0.09	2.9×10^3	0.7×10^{-1}

^a All electrochemical data were measured at RT in CH_2Cl_2 containing 0.1 M TBAPF₆. All potentials were calibrated using the Fc/Fc⁺ redox couple.

3.5 Photovoltaic Device Performance of BHJ structures.

3T and **DTT** were applied as donor materials in the active layer of BHJ OPV devices. The active layers comprising **3T** or **DTT** and PC₇₁BM with 1:1, 1:1.5, 1:1.75 and 1:2 weight ratios (donor:PC₇₁BM w/w) were made by spin-cast method. Performance characteristics of the OPV devices are summarized in **Table 3**. The PCE increased with increasing the PC₇₁BM weight ratio up to 1:1.75 weight ratio in the active layer. The optimal weight ratio for the best device performance was 1:1.75. These results suggest that the concentration of PC₇₁BM in the active layer is responsible for sufficient phase separation to generate percolation pathways of carriers.²⁶ If phase separation is insufficiently formed, the OPV devices would result in bad

performance owing to the geminated and nongeminate recombination.²⁷⁻²⁹ In general, an increase in series resistance (R_s) and a decrease in shunt resistance (R_{sh}) can reduce the FF value of OPV device.³⁰⁻³¹ Push-pull D- π -A molecules tends to aggregate and be stabilized in thin films leading to the small donor-acceptor interfacial area.^{7,32} As a result, the FF was decreased by geminate recombination.³³ Although the photogenerated excitons from donor molecules decreased when using high weight ratio of PC₇₁BM in the active layer, the blended PC₇₁BM prevented agglomeration of donor molecules (see **Fig. 4(b)** and **(d)**), leading to increased J_{sc} , V_{oc} and FF values as shown in **Table 3**. Thus, the morphology of thin films based on 3T and DTT depended on the concentration of PC₇₁BM, leading to vary V_{oc} value with PC₇₁BM concentration. To further understand why the V_{oc} variation of 3T and DTT-based OPV devices show a large dependence on the little change of donor/acceptor ratios, the performance of BHJ devices based on DTT was investigated as function of active layer thickness. The thickness of active layer was controlled by varying the spin casting speed from 700 to 3000 rpm and

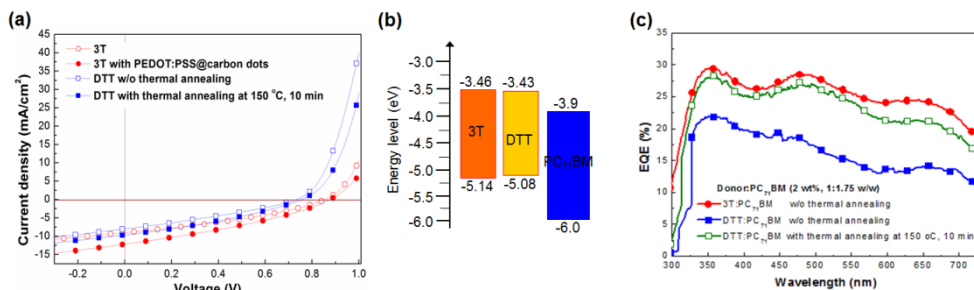


Fig. 3. (a) Current density-voltage (J - V) characteristics of OPVs from 3T and DTT under AM 1.5G illumination at 100 mWcm^{-2} , (b) HOMO and LUMO energy levels of 3T, DTT and PC₇₁BM, and (c) EQE data for BHJ devices

measured by profilometry. The resulting J - V curves for the different thickness of active layers were displayed (see **Fig. 4(a)**). The observed V_{oc} , J_{sc} , and PCE were declined with decreasing active layer thickness (see **Table 3**). It means that both thickness and morphology of active layer should be considered for the optimized performance of OPV device. We carried out thermal annealing treatment to understand about how the π -linker affects the morphology of the thin film. Interestingly, the device performance of **DTT** was improved with thermal annealing treatment of the active layer (see **Table 3**). As shown in **Fig. 4**, the surface roughness of the **DTT** thin film decreased from 0.448 to 0.235 nm with thermal annealing treatment. The PCE of the **DTT**-derived OPV device increased from 1.81% to 2.38% after thermal annealing treatment at 150 °C for 10 min (**Fig. 3(a)**), while that of the OPV device using **3T** slightly decreased with thermal annealing treatment. The J - V

Table 3 Photovoltaic performances of bulk heterojunction OPV devices

Molecule of active layer	Ratio (w/w)	V_{oc} (V)	J_{sc} (mAcm ⁻²)	FF (%)	PCE (%)	Thickness (nm)
P3HT:PC ₆₁ BM ^a	0:0.8	0.58	10.3	53	3.17	180
	1:1	0.85	6.76	31	1.78	158
3T :PC ₇₁ BM ^b	1:1.75	0.85	9.19	33	2.58	160
	1:2	0.77	9.90	32	2.44	162
3T :PC ₇₁ BM ^c	1:1.75	0.86	11.9	34	3.47	164
DTT :PC ₇₁ BM ^b	1:1.75	0.72	8.11	31	1.81	137
	1:2	0.72	7.79	30	1.68	135
DTT :PC ₇₁ BM ^d	1:1.75	0.76	9.50	33	2.38	134

Device configuration of ITO/PEDOT:PSS/donor:acceptor (2 wt%)/LiF/Al was used in all cases. ^aActive layers spin-cast in chlorobenzene. ^bActive layers spin-cast in chlorobenzene and chloroform (1:0.2 v/v). ^cPEDOT:PSS organogels were used instead of PEDOT:PSS. ^dThermal annealing treatment at 150 °C for 10 min.

curves of the 3T-based devices were shown in **Fig. 4(b)**. Although a higher J_{sc} yields after annealing treatment at 120 °C for 10 min compared to others conditions, the PCE of the device was decreased due to the low V_{oc} value. The reason for the increased of J_{sc} was considered to be improved morphology effect of active layer.³⁴ However, the V_{oc} of the device was dropped from 0.72 V to 0.64 V with annealing temperature due to the phase separation between donor and acceptor. These results were consistent with the result of DTT-based OPV devices with varying thickness of active layers (see in **Fig. 4(a)**). The as-cast condition without thermal annealing treatment exhibited the best PCE of the device. These results indicate that the thin film morphology of **DTT** has significant influence on the device performance compared to **3T**. Interestingly, when the PEDOT:PSS organogels incorporating carbon dots were introduced as the HTL of 3:PC₇₁BM (1:1.75 w/w) OPV devices, the device performance showed 34% (from 2.58% to 3.47%) increase in the PCE presumably because the organogel thin film induced the formation of interconnected structure into the PEDOT-rich domains, improving the electrical conductivity (**Fig. 3(a)** and **Table 3**).¹³

4 Conclusion

In conclusion, we designed and synthesized two push-pull donor molecules incorporating different π -linker structures for efficient OPVs. Two donor molecules have similar HOMO, LUMO energy levels and band gaps **DTT** with a rigid dithienothiophene moiety in the π -linker showed high thermal stability and well-ordered nanostructure morphology in the solid state, while **3T** with a terthiophene

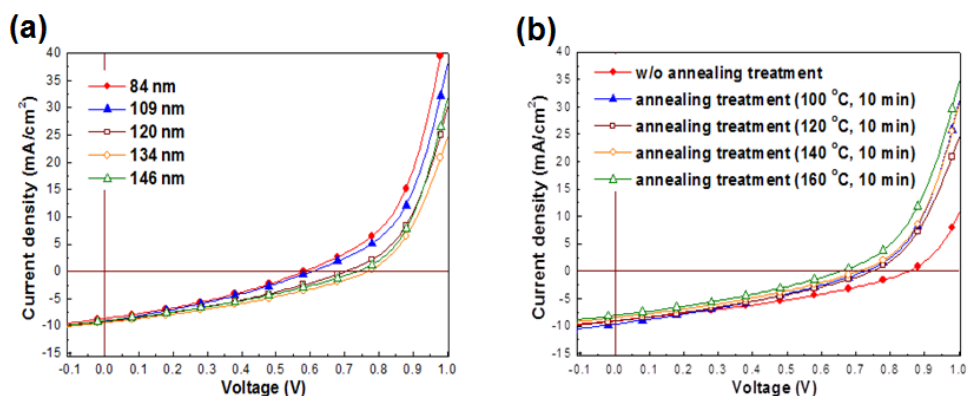


Fig 4. Current density-voltage ($J-V$) characteristics of OPVs from (a) **DTT**:PC₇₁BM active layer as function of active layer thickness and (b) **3T**:PC₇₁BM active layer as function of thermal annealing treatment conditions

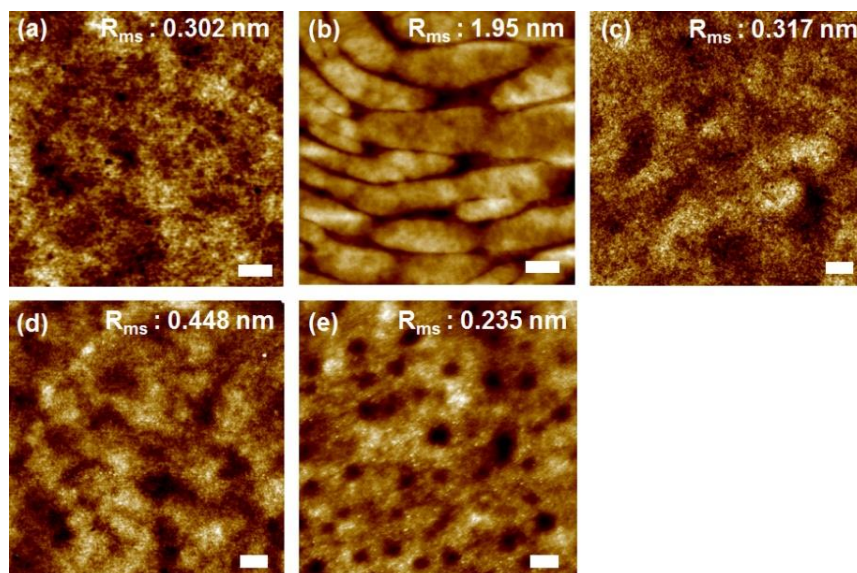


Fig 4. AFM topographic images of (a) **3T**, (b) **DTT** thin film, donor:PC₇₁BM (1:1.75 w/w) thin films of (c) **3T**:PC₇₁BM, (d) **DTT**:PC₇₁BM w/o and (e) with thermal annealing treatment at 150 °C for 10 min. All scale bars are 200 nm

π -linker showed the high electrochemical stability with a faster electrode reaction rate (k^0). The solution-processed BHJ OPV devices based on **3T** exhibited higher PCEs than **DTT**-based devices because of its superior electrochemical properties. It appears that the elaborate design of the π -linker should be considered for the development of high performance push-pull structure-based OPV devices.

5 References and Notes

- 1). Q. Zhang, B. Kan, F. Liu, G. Long, X. Wan, X. Chen, Y. Zuo, W. Ni, H. Zhang, M. Li, Z. Hu, F. Huang, Y. Cao, Z. Liang, M. Zhang, T. P. Russell and Y. Chen, *Nature Photon.*, **2015**, 9, 35.
- 2). N. S. Sariciftci, L. Smilowitz, A. J. Heeger and F. Wudl, *Science*, **1992**, 258, 1474.
- 3). X. Zhang, J. W. Shim, S. P. Tiwari, Q. Zhang, J. E. Norton, P.-T. Wu, S. Barlow, S. A. Jenekhe, B. Kippelen, J.-L. Brédas and S. R. Marder, *J. Mater. Chem.*, **2011**, 21, 4971.
- 4). J. Zhou, Y. Zuo, X. Wan, G. Long, Q. Zhang, W. Ni, Y. Liu, Z. Li, G. He, C. Li, B. Kan, M. Li and Y. Chen, *J. Am. Chem. Soc.*, **2013**, 135, 8484.
- 5). C. Duan, F. Huang and Y. Cao, *J. Mater. Chem.*, **2012**, 22, 10416.
- 6). M. Hirade, T. Yasuda and C. Adachi, *J. Phys. Chem. C*, **2013**, 117, 4986.
- 7). H. M. Ko, H. Choi, S. Paek, K. Kim, K. Song, J. K. Lee and J. Ko, *J. Mater. Chem.*, **2011**, 21, 7248.

- 8). H. Bürckstümmer, E. V. Tulyakova, M. Deppisch, M. R. Lenze, N. M. Kronenberg, M. Gsänger, M. Stolte, K. Meerholz and F. Würthner, *Angew. Chem. Int. Ed.*, **2011**, *50*, 11628.
- 9). S. Ko, E. T. Hoke, L. Pandey, S. Hong, R. Mondal, C. Risko, Y. Yi, R. Noriega, M. D. McGehee, J. L. Brédas, A. Salleo and Z. Bao, *J. Am. Chem. Soc.*, **2012**, *134*, 5222.
- 10). C. Quinton, V. Alain-Rizzo, C. Dumas-Verdes, G. Clavier, L. Vignau and P. Audebert, *New J. Chem.*, **2015**, *39*, 9700.
- 11). J. Frey, A. D. Bond and A. B. Holmes, *Chem Comm.*, **2002**, 2424.
- 12). H. Zhou, L. Yang, S. C. Price, K. J. Knight and W. You, *Angew. Chem. Int. Ed.*, **2010**, *49*, 7992.
- 13). H. C. Lim, S. H. Min, E. Lee, J. Jang, S. H. Kim and J.-I. Hong, *ACS Appl. Mater. Interfaces*, **2015**, *7*, 11069.
- 14). D. Sun, S. V. Rosokha and J. K. Kochi, *J. Am. Chem. Soc.*, **2004**, *126*, 1388.
- 15). V. Coropceanu, M. Malagoli, D. A. da Silva Filho, N. E. Gruhn, T. G. Bill and J. L. Brédas, *Phys. Rev. Lett.*, **2002**, *89*, 27553.
- 16). P. Shen, G. Sang, J. Lu, B. Zhao, M. Wan, Y. Zou, Y. Li and S. Tan, *Macromolecules*, **2008**, *41*, 5716.
- 17). C. Reichardt, *Solvent and Solvent Effects in Organic Chemistry*, 3rd ed; VCH publishers: Weinheim, **2003**.
- 18). G. Zeng, W.-L. Yu, S.-J. Chua and W. Huang, *Macromolecules*, **2002**, *35*, 6907.
- 19). Y. Wang, E. I. Rogers and R. G. Compton, *J. Electroanal. Chem.*, **2010**, *648*, 15.
- 20). S. Tanimoto and A. Ichimura, *J. Chem. Educ.*, **2013**, *90*, 778.

- 21). S. S. Jeon, C. Kim, J. Ko and S. S. Im, *J. Mater. Chem.*, **2011**, *21*, 8146.
- 22). K. S. Lee, W. J. Lee, N.-G. Park, S. O. Kim and J. H. Park, *Chem. Commun.*, **2011**, *47*, 4264.
- 23). A. V. Kesavan, A. D. Rao and P. C. Ramamurthy, *ACS Appl. Mater. Interfaces*, **2017**, *9*, 28774.
- 24). B. Lasse, W. Keld, W. J. Bjørn and J. Torben, *Sol. Energy Mater. Sol. Cells*, **2006**, *90*, 341.
- 25). H. Gerischer, *Electroanal. Chem. Inter. Electrochem*, **1975**, *58*, 263.
- 26). B. Ray, P. R. Nair and M. A. Alam, *Sol. Energy Mater. Sol. Cells*, **2011**, *95*, 3287.
- 27). H. Zang, Y. Liang, L. Yu and B. Hu, *Adv. Energy Mater.*, **2011**, *1*, 923.
- 28). S. K. Pal, T. Kesti, M. Maiti, F. Zhang, O. Inganäs, S. Hellström, M. R. Andersson, F. Oswald, F. Langa, T. österman, T. Pascher, A. Yartsev and V. Sundström, *J. Am. Chem. Soc.*, **2010**, *132*, 12440.
- 29). T. M. Clarke and J. R. Durrant, *Chem. Rev.*, **2010**, *110*, 6736.
- 30). B. Walker, A. B. Tamayo, X.-D. Dang, P. Z. Jung, H. Seo, A. Garcia, M. Tantiwivat and T.-Q. Nguyen, *Adv. Funct. Mater.*, **2009**, *19*, 3063.
- 31). C. V. Hoven, X.-D. Dang, R. C. Coffin, J. Peet, T.-Q. Nguyen and G. C. Barzan, *Adv. Mater.*, **2010**, *22*, E63.
- 32). X. Bulliard, Y. W. Jin, G. H. Lee, S. Yun, D.-S. Leem, T. Ro, K.-B. Park, C.-J. Heo, R.-I. Satoh, T. Yagi, Y. S. Choi, S.-J. Lim and S. Lee, *J. Mater. Chem. C*, **2016**, *4*, 1117.
- 33). M.-S. Kim, B.-G. Kim and J. Kim, *ACS Appl. Mater. Interfaces*, **2009**, *1*, 1264.
- 34). M. C. Scharber, D. Mühlbacher, M. Koppe, P. Denk, C. Waldauf, A. J. Heeger and C. J. Brabec, *Adv. Mater.*, **2006**, *18*, 789.

Section 2. Effect of π -linker on Push-Pull D- π -A Donor molecules for Highly Sensitivity Organic Photodectors

Abstract

We report organic photodetectors (OPDs) exhibiting high photocurrent density (J_{ph}), low dark current density (J_{d}), and broadband external quantum efficiency (EQE) using three push-pull type small molecules (**H1-H3**) as donor materials. We designed three push-pull type D- π -A molecules with different π -linker structures and systematically investigated their photophysical, thermal, and morphological properties, and OPD performance. Among three donor molecules, **H3** had weaker intermolecular interactions and lower π - π packing density than other donor molecules, and thus exhibited higher sensitivity and broadband EQE in both planar heterojunction (PHJ) OPDs and bulk heterojunction (BHJ) OPDs. The BHJ OPDs with **H3** exhibited a broadband EQE value of 64% at 530 nm, a low J_{d} value of 1.54×10^{-8} and a high J_{ph} value of $9.57 \times 10^{-3} \text{ Acm}^{-2}$ at -3 V bias under AM 1.5G irradiation.

KEYWORDS: organic photodetector, push-pull structure, dark current density, heterojunction, deep subgap state

1 Introduction

Organic photovoltaics have recently attracted great attention due to their advantages of low cost, physical flexibility, and easy fabrication of large area. One type of photovoltaics, organic photodetectors (OPDs) convert light energy into electrical signal such as current so that sensitivity and the magnitude of current generated by light are important.^{1,2} Although conventional photodetectors based on inorganic semiconductors have been used for a wide range of applications such as automobile cameras, medical instruments, optical communication and so on,^{3,4} there are still limitations in achieving high sensitivity and resolution.^{5,6} This is because electrical crosstalk occurs due to the long lifetime and rapid mobility of the carriers, and high cost is additionally generated for the nano-fabrication processes. For these reasons, small molecules with well-defined chemical structures are suitable candidate materials for OPDs due to their tunability of optical and electrical properties. However, one of the biggest challenges for small molecule-based OPDs is to realize panchromatic donor materials with high photocurrent density (J_{ph}) and low dark current density (J_d).⁷⁻¹⁰ It is therefore indispensable to develop OPD donor molecules satisfying the above characteristics. Although optical properties of π -conjugated push-pull molecules end-capped with an electron donor (D) and an electron acceptor (A) units can be easily tuned, their absorption bands tend to have a narrow full width at half maximum (FWHM) due to the strong intramolecular charge transfer (ICT) characteristic. However, with strong intermolecular interactions between donor materials, their absorption bands are effectively broadened at solid state.^{11,12} The general strategy for inducing π - π stacking would be to introduce a π -linker between D and A units.¹³ Furthermore, π - π stacking interactions in thin films would induce morphology changes, which

plays an important role in OPD performance. This is because that the interpenetrating network of donor and acceptor molecule domains in thin films are related to efficient dissociation of excitons and successful charge carrier extraction. In general, organic materials are polycrystalline or amorphous in thin film compared to inorganic materials. Polycrystalline structures tend to capture excitons¹⁴ and electrons¹⁵ because of various energy states generated at the interface,^{16,17} resulting in bad performance of OPD devices. Thus, these phenomena should be considered to achieve high efficiency OPD devices with a broad range of sunlight harvesting ability. Even though the influence of the molecular structure and the morphology on the performance of OPV devices has been investigated,¹⁸ the effect of these factors on the performance of OPD devices has not been studied systematically. Therefore, evaluation of correlation between the donor molecular structure and the performance of OPD device is required.

In this work, we report an approach to achieve high external quantum efficiency (EQE) with broad absorption range in the visible region in OPD devices using three push-pull (D- π -A) molecules as donor materials with different π -linker structures. We demonstrated that the π -linker structure of donor molecules affected π - π packing in thin films, resulting in different optical, thermal and morphological properties. We performed a systematic study on the relationship between donor molecular structures and the performance of the OPD devices. Among the three donor molecules examined, the **H3** with a short π -linker showed superior performance in bulk heterojunction (BHJ) OPD structures with a low J_d value of 1.54×10^{-8} , a high J_{ph} value of $1.54 \times 10^{-3} \text{ Acm}^{-2}$ and a EQE value of 64 % (530 nm) at -3 V bias. The result suggests that π -linker structure of push-pull D- π -A molecules could affect crystalline in thin film, and amorphous-like domain (**H3**) of

photoactive layer could induce more effective performance in OPD devices than the polycrystalline domain system (**H2**).

2 Experimental Methods

2.1 Reagents and Materials

All the chemical agents were used without further purification. Tetrakis(triphenylphosphine)palladium(0) (Pd(PPh₃)₄), Tris(dibenzylideneacetone)dipalladium(0) (Pd(dba)₃), 2,5-dibromothiophene, 2-(3-hexylthiophen-2-yl)-4,4,5,5-tetramethyl-1,3,2-dioxaborolane, 2-(3-oxo-2,3-dihydro-1H-inden-1-ylidene)malononitrile were purchased from Toyko Chemical Industry (TCI). N-bromosuccinimide (NBS), tetrabutylammonium hexafluorophosphate (TBAPF₆), Phosphorus(V) oxychloride (POCl₃), 4-bromo-N,N-diphenylaniline, potassium carbonate (K₂CO₃), sodium bicarbonate (NaHCO₃) and N,N'-dimethylformamide (DMF) were purchased from Sigma-Aldrich and SAMCHUN. Fullerene-C₆₀ (C₆₀, 99.95%) was purchased from SES Research.

2.2 Synthetic Procedure

dithieno[3,2-b:2',3'-d]thiophene (compound 4) was prepared according to the literature procedure¹

2-bromodithieno[3,2-b:2',3'-d]thiophene (5)

To a solution of **compound 4** (0.8 g, 4.1 mmol) in CHCl₃ (20 ml) cooled in an ice bath was slowly added AcOH (20 ml). The reaction mixture was treated with NBS (0.881 g, 4.9 mmol) and stirred for 10 h. The reaction mixture was treated with aqueous solution of NaOH (25 ml, 1 M), stirred in an ice bath for 2 h, then

concentrated under vacuum, and extracted with dichloromethane. The organic phase was washed with water and brine, and dried over anhydrous MgSO₄. All volatiles were evaporated and the crude product was purified by column chromatography on silica gel using dichloromethane to give yellow solid product (yield: 0.95 g, 85%). ¹H NMR (300 MHz, Acetone-d₆, ppm) δ: 7.67 (s, 1H), 7.65 (d, 1H, 4.3 Hz), 7.50 (d, 1H, 5.2 Hz)

6-bromodithieno[3,2-b:2',3'-d]thiophene-2-carbaldehyde (6)

DMF (0.85 ml, 11.6 mmol) and POCl₃ (0.55 ml, 5.8 mmol) were added to a solution of **compound 5** (0.8g, 2.9 mmol) in distilled dichloromethane (25 ml) cooled in an ice bath. The reaction mixture was stirred at RT for 2 h and then heated at 70 oC for 12 h. The reaction mixture was cooled to RT, treated with NaOAc (20 ml, 2 M), and stirred for 2 h. Volatiles were evaporated under vacuum and the resulting residue was extracted with dichloromethane. The organic phase was washed with water and brine, and dried over anhydrous Na₂SO₄. The crude product was purified by column chromatography on silica gel using dichloromethane and hexane (1:4 v/v) to give yellow-red solid product (yield: 0.66 g, 75 %). ¹H NMR (300 MHz, acetone-d₆, ppm) δ: 10.06 (s, 1H), 8.40 (s, 1H), 7.75 (s, 1H)

6-(4-(diphenylamino)phenyl)dithieno[3,2-b:2',3'-d]thiophene-2-carbaldehyde (8)

A mixture of **compound 7** (0.66 g, 2.2 mmol), **compound 6** (0.89 g, 2.4 mmol), Pd(PPh₃)₄ (0.083 g, 0.07 mmol) and NaHCO₃ (2.74 g, 32.7 mmol) in THF and H₂O (30 ml/10 ml, 3:1 v/v) was refluxed for 48 h. The reaction mixture was concentrated under vacuum and was extracted with dichloromethane. The organic

phase was washed with water and brine, and dried over anhydrous MgSO_4 . Volatiles were evaporated and the residue was purified by column chromatography on silica gel using dichloromethane and hexane (2:1 v/v) to give yellow solid product (yield: 0.68 g, 67 %). ^1H NMR (300 MHz, acetone- d_6 , ppm) δ : 10.04 (s, 1H), 8.38 (s, 1H), 7.84 (s, 1H), 7.69 (d, 2H, 8.7 Hz), 7.37 (t, 4H, 7.8 Hz), 7.16 (d, 6H, 8.3 Hz), 7.10 (t, 3H, 7.0 Hz)

2-((6-(4-(diphenylamino)phenyl)dithieno[3,2-b:2',3'-d]thiophen-2-yl)methylene)-1H-indene-1,3(2H)-dione (H1)

To a solution of **compound 8** (0.60 g, 1.28 mmol) in THF (20 ml) at 65 °C was added dropwise 1,3-indandione (0.215 g, 1.47 mmol) in THF (7 ml). The reaction mixture was stirred 60 h at the same temperature, cooled to RT and concentrated under vacuum. The crude product was purified by column chromatography on silica gel using dichloromethane to give dark pink solid product, which was treated with dichloromethane and ethanol to isolate the product as precipitates. The precipitate was purified further by temperature gradient sublimation under reduced pressure (10^{-3} torr) to give dark green solid product (yield: 0.27 g, 35%). ^1H NMR (300 MHz, DMSO- d_6 , ppm) δ : 8.63 (s, 1H), 8.13 (s, 1H), 7.93 (m, 5H), 7.66 (d, 2H), 7.37 (t, 4H, 7.7 Hz), 7.16 (s, 1H), 7.11 (d, 5H, 7.9 Hz), 7.01 (d, 2H, 8.5 Hz). HRMS (FAB) m/z : calcd $\text{C}_{36}\text{H}_{21}\text{NO}_2\text{S}_3$ 595.07, $[\text{M}+\text{H}]^+$: observed 595.07. Elemental analysis calc.: C, 72.58; H, 3.55; N, 2.35; O, 5.37; S, 16.14; found: C, 72.68; H, 3.47; N, 2.32; O, 5.37; S, 16.23

2,2':5',2''-terthiophene (9)

A mixture of 2,5-dibromothiophene (1 g, 4.13 mmol), thiophen-2-ylboronic acid (1.59 g, 12.4 mmol), $\text{Pd}(\text{PPh}_3)_4$ (0.29 mg, 0.25 mmol), and K_2CO_3 (5 ml, 2M) in

THF:MeOH (20:4 ml v/v) was heated at 100 °C for 36 h. Then the reaction mixture was cooled to RT, then concentrated under vacuum, and the resulting mixture was extracted with dichloromethane. The organic phase was washed with water and brine, and dried over anhydrous MgSO₄. Volatiles were evaporated and the crude product was purified by column chromatography on silica gel using hexane to give yellow solid product (yield: 0.70 g, 70%). ¹H NMR (300 MHz, acetone-d₆, ppm) δ: 7.46 (dd, 2H, 0.9, 5.1 Hz), 7.32 (dd, 2H, 0.9, 3.5 Hz), 7.23 (s, 2H), 7.11 (dd, 2H, 3.7, 5.0 Hz)

5-bromo-2,2':5',2''-terthiophene (10)

To a solution of **compound 9** (0.7 g, 2.82 mmol) in CHCl₃ (20 ml) cooled in an ice bath was slowly added AcOH (20 ml). The reaction mixture was treated with NBS (0.553 g, 3.1 mmol) and stirred for overnight. The reaction mixture was treated with saturated aqueous NaHCO₃ (20 ml), stirred at RT for 2 h, then concentrated under vacuum, and extracted with dichloromethane. The organic phase was washed with water and brine, and dried over anhydrous MgSO₄. All volatiles were evaporated and the crude product was purified by column chromatography on silica gel using hexane to give yellow solid product (yield: 0.70 g, 76%). ¹H NMR (300 MHz, Acetone-d₆, ppm) δ: 7.47 (t, 1H, 5.3 Hz), 7.33 (t, 1H, 3.5 Hz), 7.24 (s, 2H), 7.17 (m, 2H), 7.11 (m, 1H)

5''-bromo-[2,2':5',2''-terthiophene]-5-carbaldehyde (11)

DMF (0.66 ml, 8.59 mmol) and POCl₃ (0.41 ml, 4.30 mmol) were added to a solution of **compound 10** (0.7 g, 2.15 mmol) in distilled dichloromethane (20 ml) cooled in an ice bath. The reaction mixture was stirred at RT for 2 h and then heated at 70 °C for 12 h. The reaction mixture was cooled to RT, treated with

NaOAc (20 ml, 2 M), and stirred for 2 h. Volatiles were evaporated under vacuum and the resulting residue was extracted with dichloromethane. The organic phase was washed with water and brine, and dried over anhydrous Na₂SO₄. The crude product was purified by column chromatography on silica gel using dichloromethane and hexane (2:1 v/v) to give orange solid product (yield: 0.58 g, 76 %). ¹H NMR (300 MHz, acetone-d₆, ppm) δ: 9.95 (s, 1H), 7.96 (d, 1H, 4.0 Hz), 7.52 (d, 2H, 3.1 Hz), 7.33 (d, 1H, 3.9 Hz), 7.22 (dd, 2H, 3.9, 7.3 Hz)

5''-(4-(diphenylamino)phenyl)-[2,2':5',2''-terthiophene]-5-carbaldehyde (12)

A mixture of **compound 7** (0.71 g, 2.46 mmol), **compound 11** (0.58 g, 1.64 mmol), Pd(PPh₃)₄ (0.057 g, 0.049 mmol) and NaHCO₃ (2.07 g, 24.6 mmol) in THF and H₂O (30 ml/10 ml, 3:1 v/v) was refluxed for 48 h. The reaction mixture was concentrated under vacuum and was extracted with dichloromethane. The organic phase was washed with water and brine, and dried over anhydrous MgSO₄. Volatiles were evaporated and the residue was purified by column chromatography on silica gel using dichloromethane and hexane (2:1 v/v) to give orange-red solid product (yield: 0.72 g, 84 %). ¹H NMR (300 MHz, acetone-d₆, ppm) δ: 9.95 (s, 1H), 7.96 (d, 1H, 3.9 Hz), 7.63 (d, 2H, 8.6 Hz), 7.52 (dd, 2H, 3.9, 6.7 Hz), 7.39 (d, 3H, 3.7 Hz), 7.34 (t, 4H, 3.9 Hz), 7.13 (d, 6H, 7.8 Hz), 7.07 (d, 2H, 8.7 Hz)

2-((5''-(4-(diphenylamino)phenyl)-[2,2':5',2''-terthiophen]-5-yl)methylene)-1H-indene-1,3(2H)-dione (H2)

To a solution of **compound 12** (0.72 g, 1.4 mmol) in THF (25 ml) at 65 °C was added dropwise 1,3-indandione (0.235 g, 1.61 mmol) in THF (7 ml). The reaction mixture was stirred 60 h at the same temperature, cooled to RT and concentrated under vacuum. The crude product was purified by column chromatography on

silica gel using dichloromethane to give dark pink solid product, which was treated with dichloromethane and ethanol to isolate the product as precipitates. The precipitate was purified further by temperature gradient sublimation under reduced pressure (10^{-3} torr) to give dark green solid product (yield: 0.25 g, 28%). ^1H NMR (300 MHz, DMSO- d_6 , ppm) δ : 8.23 (d, 1H, 4.1 Hz), 8.08 (s, 1H), 7.95 (s, 4H), 7.70 (d, 1H, 3.9 Hz), 7.67 (d, 1H, 4.0 Hz), 7.61 (d, 2H, 8.6 Hz) 7.47 (dd, 3H, 3.8, 11.1 Hz), 7.36 (t, 4H, 7.7 Hz), 7.10 (t, 6H, 9.2 Hz), 7.00 (d, 2H, 8.5 Hz). HRMS (FAB) m/z : calcd C₄₀H₂₅NO₂S₃ 647.83, [M+H]⁺: observed 647.10. Elemental analysis calc.: C, 74.16; H, 3.89; N, 2.16; O, 4.94; S, 14.85; found: C, 74.18; H, 3.78; N, 2.09; O, 4.98; S, 14.93

N,N-diphenyl-4-(thiophen-2-yl)aniline (13)

A mixture of (4-(diphenylamino)phenyl)boronic acid (2.13 g, 7.4 mmol), 2-bromothiophene (1.0 g, 6.1 mmol), Pd(PPh₃)₄ (0.35 g, 0.31 mmol) and K₂CO₃ (15 ml, 2M) in THF (45 ml) was refluxed for 24 h. The reaction mixture was concentrated under vacuum and was extracted with dichloromethane. The organic phase was washed with water and brine, and dried over anhydrous MgSO₄. Volatiles were evaporated and the residue was purified by column chromatography on silica gel using hexane to give white solid product (yield: 1.43 g, 71 %). ^1H NMR (300 MHz, acetone- d_6 , ppm) δ : 7.59 (d, 2H, 8.6 Hz), 7.39 (t, 2H, 4.6 Hz), 7.34 (t, 4H, 7.9 Hz), 7.07 (m, 9H)

5-(4-(diphenylamino)phenyl)thiophene-2-carbaldehyde (14)

DMF (1.35 ml, 17.5 mmol) and POCl₃ (0.83 ml, 8.74 mmol) were added to a solution of **compound 13** (1.43 g, 4.37 mmol) in distilled dichloromethane (25 ml) cooled in an ice bath. The reaction mixture was stirred at RT for 2 h and then

heated at 70 °C for 12 h. The reaction mixture was cooled to RT, treated with NaOAc (25 ml, 2 M), and stirred for 2 h. Volatiles were evaporated under vacuum and the resulting residue was extracted with dichloromethane. The organic phase was washed with water and brine, and dried over anhydrous Na₂SO₄. The crude product was purified by column chromatography on silica gel using dichloromethane and hexane (2:1 v/v) to give yellow-green solid product (yield: 0.58 g, 76 %). ¹H NMR (300 MHz, acetone-d₆, ppm) δ: 9.92 (s, 1H), 7.95 (d, 1H, 3.9 Hz), 7.70 (dd, 2H, 1.9, 6.8 Hz), 7.57 (d, 1H, 4.0 Hz), 7.37 (dd, 4H, 5.4, 10.3 Hz), 7.14 (dd, 6H, 6.3, 7.6 Hz), 7.05 (d, 2H, 6.9 Hz)

2-((5-(4-(diphenylamino)phenyl)thiophen-2-yl)methylene)-1H-indene-1,3(2H)-dione (H3)

To a solution of **compound 14** (0.51 g, 1.4 mmol) in THF (25 ml) at 65 °C was added dropwise 1,3-indandione (0.252 g, 1.72 mmol) in THF (7 ml). The reaction mixture was stirred 60 h at the same temperature, cooled to RT and concentrated under vacuum. The crude product was purified by column chromatography on silica gel using dichloromethane to give pink-red solid product, which was treated with dichloromethane and ethanol to isolate the product as precipitates. The precipitate was purified further by temperature gradient sublimation under reduced pressure (10⁻³ torr) to give dark pink solid product (yield: 0.29 g, 37%). ¹H NMR (300 MHz, DMSO-d₆, ppm) δ: 8.25 (d, 1H, 4.1 Hz), 8.04 (s, 1H), 7.93 (m, 4H), 7.76 (d, 2H, 8.7 Hz), 7.69 (d, 1H, 4.1 Hz), 7.39 (t, 4H, 7.8 Hz), 7.15 (m, 6H), 7.00 (d, 2H, 8.7 Hz). HRMS (FAB) m/z: calcd C₃₂H₂₁NO₂S₃ 483.13, [M+H]⁺: observed 483.13. Elemental analysis calc.: C, 79.48; H, 4.38; N, 2.90; O, 6.62; S, 6.63; found: C, 79.59; H, 4.25; N, 2.78; O, 6.96; S, 6.42

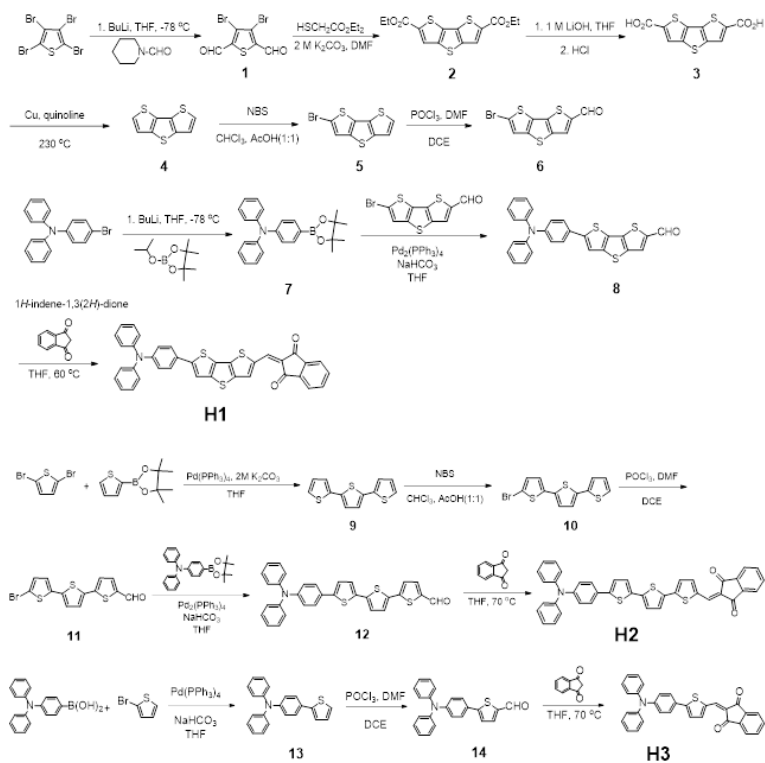
2.3 Instruments

^1H and ^{13}C NMR spectra were recorded in CDCl_3 , acetone- d_6 or DMSO- d_6 using Avance 300 and 400 MHz Bruker spectrometer. Mass spectra were obtained using a GC-MS spectrometer (JEOL, JMS-700). The optical properties were characterized by absorption (Beckman, DU650) and photoluminescence (PL) spectra (Jasco, FP-7500 spectrophotometer). The electrochemical properties were obtained using the cyclic voltammetry (CV) (CH instruments, 650B electrochemical analyzer). The electrochemical cell consists of three electrodes (a reference electrode, Ag/Ag^+ 0.01 M, a counter electrode (Pt) and a working electrode (Pt)) in dichloromethane containing 0.1 mM donor molecule as a redox material and tetrabutylammonium hexafluorophosphate (0.1 M TBAPF₆) as a supporting electrolyte. All potentials were calibrated using a ferrocene/ferrocenium (Fc/Fc^+) redox couple. Density functional theory (DFT) calculations were performed to obtain HOMO/LUMO energy levels of 3T and DTT using the Gaussian B3LYP/6-31G (Gaussian 09 Rev. B01). Tapping mode atomic force microscopy (AFM) (Veeco, NanoScope IV) images were acquired using a scan rate of 1 Hz under ambient atmosphere. All the samples were prepared by spin-casting onto ITO/glass substrate. The film thickness of organic layers was measured using alpha-step (KLA Tencor). Thermal properties of the synthesized materials were obtained using a thermal gravimetric analyzer (TGA) (TA instruments, Q-5000 IR) and differential scanning calorimeter (DSC) (TA instrument, DSC-Q1000). Elemental analysis was performed with the Thermo Fisher Scientific Elemental (Flash2000). High resolution transmission electron microscope (HRTEM, JEOL JEM-2100) was performed at 200 kV for acquisition the surface image of thin films. Current density–voltage (J – V) characteristics were measured under an AM

1.5G solar simulator (Oriel), or in the dark and recorded using a Keithley 237 source measurement unit. Before measurement, the light intensity was calibrated with the aid of a National Renewable Energy Laboratory-certified reference silicon solar cell fitted with a KG-5 filter. The EQE was measured using a 1,000 W Xe lamp (Oriel) combined with a calibrated monochromator (Acton Research). The intensity of monochromatic light was calibrated with the aid of a silicon photodiode (Newport).

2.4 Organic Photodetector Preparation

The OPDs have the following structure: indium tin oxide (ITO, 150 nm) / MoO₃ (3 nm) / Donor (20 nm) / C₆₀ (40 nm) / bathocuproine (BPC) (8 nm) / Al (100 nm) for OPDs with planar heterojunction and ITO (150 nm) / MoO₃ (3 nm) / Donor (10 nm) / Donor:C₆₀ (1:1, 150 nm) / C₆₀ (10 nm) / BCP (8 nm) / Al (100 nm) for OPDs with bulk heterojunction. The ITO substrate was successively cleaned with detergent solution, acetone, and isopropyl alcohol to remove particles and organic materials. MoO₃ was used as an interfacial layer and deposited using thermal evaporation onto the substrate with a rate of 0.2 Å/s. Donors and C₆₀ were also deposited using thermal evaporation onto the substrate with a rate of 0.4 Å/s. The exciton blocking layer, BCP, and aluminum metal cathode were deposited with rates of 0.5 Å/s and 4.0 Å/s, respectively. The all layers are successively evaporated without breaking the vacuum at a base pressure 5×10^{-7} torr and all devices were encapsulated in N₂ ambient before measurements.



Scheme 1. Synthesis of **H1**, **H2**, and **H3**.

3 Results and Discussion

3.1 Structural Characterization

Three donor molecules of **H1**, **H2** and **H3** were synthesized according to scheme 1. The detailed syntheses and structure characterizations of all the compounds were described in the Supporting Information. The final products were purified by temperature gradient sublimation under reduced pressure (10^{-3} torr) and then characterized by ^1H NMR, mass spectra, and elemental analysis. ^{13}C NMR spectra could not be obtained due to poor solubility of the final products. The push-pull

structure consists of triphenylamine as an electron-donating (D) unit and indandione as an electron-withdrawing (A) unit. The D and A units were linked through dithienothiophene (**H1**), terthiophene (**H2**), or thiophene (**H3**), as shown in scheme 1. To predict the optimized geometries and orbital energy levels of three donor molecules, density functional theory (DFT) calculations were performed using the B3LYP/6-31G basis sets. The orbital densities of the highest occupied molecular orbital (HOMO) and the lowest unoccupied molecular orbital (LUMO) were predominantly localized on the D and A units, respectively, showing the characteristics of a typical push-pull structure. And the shorter the distance between the D and A units, the larger the orbital overlap in the π -linker. The degree of the orbital overlap is in the order of **H3** > **H1** > **H2**. These results indicate that **H3** has better electronic coupling than that of other donor molecules. The dipole moments increased in the order of **H2** (5.39 D) > **H1** (5.22 D) > **H3** (4.26 D) with increasing distance between the D and A units.

3.2 Photophysical, Electrochemical and Thermal Properties

The absorption spectra of **H1**, **H2** and **H3** were investigated in solution state and in neat thin films fabricated by vacuum deposition as shown in *Fig. 2a* and summarized in *Table 1*. All donor molecules exhibited almost similar absorption bands. The absorption peaks around 300 and 380 nm were in agreement with $n-\pi^*$ electronic transition band of triphenylamine and $\pi-\pi^*$ transition bands of the π -linker, respectively.⁽¹⁹⁾ The long absorption band around 530 nm would originate from intramolecular charge transfer (ICT) between D and A units.¹³ The absorption spectra of these molecules in neat thin films showed broadened bands compared to those in solution state. Thin film of **H2** exhibited the widest absorption spectrum

presumably because of strong intermolecular π - π interactions. This suggests that the π -linker can affect intermolecular interactions, leading to changes in the electronic transitions in solid state. Table S1 predicts Gibbs free energy changes (ΔG^0) for the driving force of electron transfer.²⁰ ΔG^0 values were calculated as follows;

$$\Delta G^0 = PES_{donor} - EA_{C60} = (\lambda_{abs,max} - \lambda_{flu,mzxx}) - EA_{C60} \quad (1)$$

where PES_{donor} is the lowest potential energy surface of the excited donor and EA_{C60} is electron affinity of C_{60} as an acceptor molecules for OPD devices. The PES_{donor} values of donor molecules were estimated by stokes shift in optical spectra of thin films. Although the largest Stokes shift value was observed in **H2** with the highest dipole moment,²¹ calculated PES_{donor} and ΔG^0 values of three donor molecules were similar. Therefore, the performance of OPD devices would be determined by other factors such as morphology of thin films. Although the donor: C_{60} (1:1) blend films displayed a similar absorption pattern as neat thin films, the deges of the low energy region were blue-shifted compared to the neat thin films as shown in **Fig. 2a** and **b**.

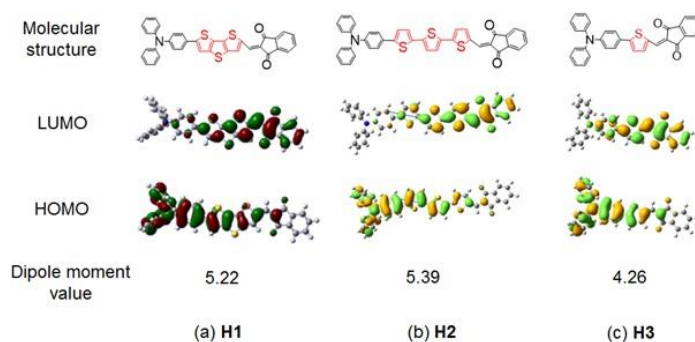


Fig. 1. Calculated geometries, orbital density maps and dipole moment values of (a) **H1**, (b) **H2** and (c) **H3**.

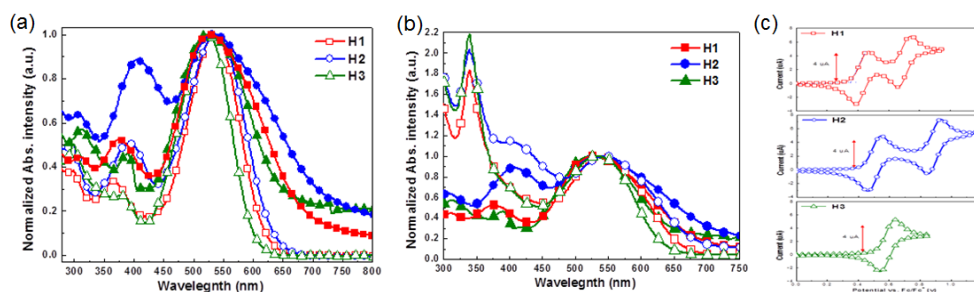


Fig. 2. Normalized UV-vis absorption spectra of (a) **H1**, **H2**, and **H3** (open circle: solution state in CH_2Cl_2 , closed circle: solid state in thin film), (b) **H1**, **H2** and **H3** (closed symbol line: neat thin film, open symbol line: **donor**: C_{60} (1:1) blend thin film) (rectangle: **H1**, circle: **H2** and triangle: **H3**) and (c) cyclic voltammograms of donor molecules in CH_2Cl_2 with tetrabutylammonium hexafluorophosphate (0.1 M TBAPF_6) as a supporting electrolyte at a scan rate of 0.05 V/s.

Thermal properties of **H1**, **H2** and **H3** were investigated with thermogravimetric analysis (TGA) and differential scanning calorimetry (DSC), and summarized in Table 1. T_d (decomposition temperature) value, defined as the temperature at which 5% mass loss occurs, was measured by TGA. **H2** exhibited slightly higher thermal stability than other molecules. The lowest values of T_d and T_g (glass transition temperature) were observed for **H3** because of its relatively flexible structure and low molecular weight. The HOMO and LUMO energy levels of these molecules were determined from the onset oxidation potential of cyclic voltammetry (CV) and the low-energy onset of absorption spectra. The values of energy gap (E_g), HOMO and LUMO levels of donor molecules were listed in **Table 1**. As shown in **Fig. 2c**, the CV showed quasi-reversible oxidation reactions in using tetrabutylammonium hexafluorophosphate (0.1 M TBAPF_6) as a supporting electrolyte in dichloromethane at a scan rate of 0.05 V/s. This is because that the cation radical of triphenylamine is stabilized by resonance delocalization.²² The HOMO and LUMO levels of donor molecules corrected by the

ferrocene/ferrocenium redox couple (Fc/FC⁺)²³ were almost identical. The HOMO value of **H2** (5.20 eV) was higher than those of **H1** (5.27 eV) and **H3** (5.36 eV). This indicates that the electron donating ability is further improved by three thiophene units as a π -linker. The E_g value of **H3** with a short π -conjugation length was the largest. These results suggest that optical, thermal and electrochemical properties of donor molecules can be tuned effectively through the introduction of π -linker.

Table 1 Photophysical and thermal properties of **H1**, **H2** and **H3**

Molecules	λ_{\max}^a (nm)	λ_{abs}^a (max) Lmol ⁻¹ cm ⁻¹	λ_{\max}^b (nm)	HOMO/LUMO ^c (eV)	E _g ^d (eV)	T _d ^e (°C)	T _g ^f (°C)
H1	536	4.0 × 10 ⁴	528	5.27/3.28	1.99	400	289
H2	538	3.1 × 10 ⁴	533	5.20/3.24	1.96	420	278
H3	523	3.0 × 10 ⁴	523	5.36/3.31	2.05	380	195

^a Measured in dichloromethane. ^b Thin film by vacuum thermal evaporation. ^c Energy levels from CV and absorption spectra. ^d Band gaps. ^e Temperature at 5% weight loss under nitrogen. ^f determined by DSC under nitrogen.

3.3 Morphology Study of Thin Films

The morphology of thin films is known to be one of the key factors determining the performance of OPDs. The morphology of thin films was investigated by tapping mode atomic force microscope (AFM) and scanning electron microscope (SEM). In general, long π -linker length ensured strong intermolecular interactions in thin films, which accordingly resulted in large domain size.^{19,24} The intermolecular interaction between donor molecules is among the factors affecting the morphology in thin films. As a result, neat thin film of **H2**

with a long π -linker displayed partial crystalline regions in the SEM images as shown in **Fig. 3h**. As shown in **Fig. 3a–f**, root mean square surface roughness (R_{rms}) values of the donor:C₆₀ (1:1) blend films were better than those of neat thin films. In the neat thin film of **H2** except for the region where partial crystallization was formed, both the domain sizes and the R_{rms} (0.53 nm) was observed to be smaller than those of of **H1** (1.1 nm) and **H3** (0.72 nm). Interestingly, the surface roughness and topography image of **H1** neat thin film were not significantly different from the blend film of **H1**:C₆₀ (1:1). On the other hand, surface roughness and image of **H2** and **H3** neat films were different from those of blend films (donor:C₆₀ (1:1)). It is noteworthy that the domain size as well as the packing density of molecules in thin films was influenced by the π -linker structure of donor molecules.

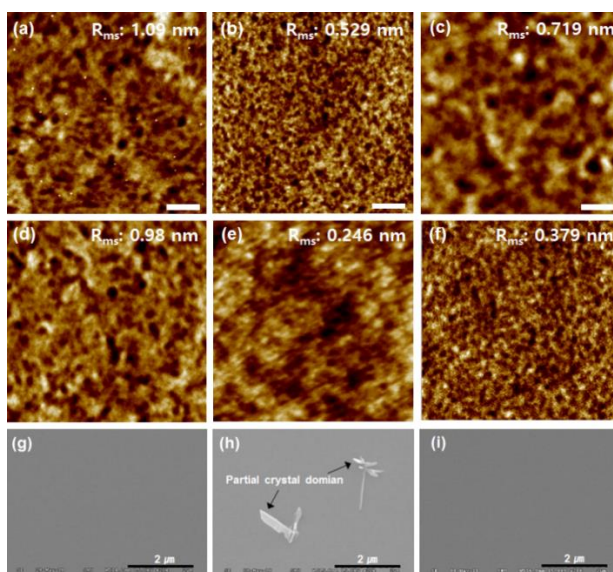


Fig. 3. AFM topographic images of (a) **H1**, (b) **H2**, (c) **H3**, (d) **H1**:C₆₀ (1:1), (e) **H2**:C₆₀ (1:1) and (f) **H3**:C₆₀ (1:1). All scan bars are 500 nm. And SEM image of neat thin films of (g) **H1**, (h) **H2**, (f) **H3**

Table 2 Characteristics data for measured of **H1**, **H2** and **H3**

Molecules	Reorganization energy (λ) ^a	$\lambda_{\text{abs, max}}$ (eV) ^b	PES value ^c	EA(C ₆₀)	ΔG° (PES – EA(C ₆₀))
	($\lambda_{\text{abs, max}}$ (eV) – $\lambda_{\text{flu, max}}$ (eV))	transition			
H1	0.58	2.96	3.54		– 0.96
H2	0.66	2.90	3.56	4.5	– 0.94
H3	0.54	2.99	3.53		– 0.97

^a Reorganization energy is Stokes shift in optical spectra of thin films. ^b $\lambda_{\text{abs, max}}$ transition is absorption peak from thin film. ^c PES is ($\lambda_{\text{abs, max}} - \lambda_{\text{flu, max}}$) – EA_{C60}.

3.4 Organic Photodetector Performance

Two types of OPD devices were fabricated using donor molecules and C₆₀. One is planar heterojunction (PHJ) with well-defined interface and another is co-evaporation of donor and C₆₀ molecules (1:1) resulting in the formation of a bulk heterojunction in photoactive layer. As shown in **Fig. 4**, the PHJ device based on **H3** (abbreviated as **P–H3**) exhibited better performance compared to others PHJ devices (using **H1** and **H3**) at semilog-current density-voltage (J – V) characteristics. The figure-of-merits of the devices according to the donor molecules were summarized in **Table 3**. The D^* value defined as the ability to detect a small photo signal was calculated using eq 1,

$$D^* = \frac{R}{(2qJ_D)^{1/2}} = \left(\frac{J_{ph}}{P_{light}}\right)(2qJ_D)^{1/2} \quad (1)$$

where R is the photoresponsivity, q the electron charge (1.6×10^{-19} C). Although, the PHJ device based on **H1** (abbreviated as **P–H1**) showed the highest J_{ph} value (6.4×10^{-3} Acm⁻²), the specific detectivity (D^*) value (2.2×10^{11} cmHz^{1/2}W⁻²) was lower than that of **P–H3** due to a high J_d value (3.4×10^{-8} Acm⁻²) at applied -3 V. One of the factors affecting J_d is injection of electrons from ITO electrode to the

LUMO of donor molecule despite the presence of a MoO₃ layer as an electron blocking layer between ITO electrode and photoactive layer. However, since the LUMO levels of donor molecules were similar, it is considered that the morphological difference of thin films would be the main reason for the generation of J_d . It can be inferred that the crystallinity and grain size were the main limiting factors for the J_d value,^{25,26} considering the results of AFM, SEM and optical properties. **H2** having a long π -linker was expected to better π - π stacking with large domains in thin film, but resulting in partial crystallization and small domain size in thin film as shown in *Fig. 3h*. Thus, many interface can be formed, leading to the generation of deep subgap states at the interface of domains.^{27,28} The deep subgap states originating from morphology disorders in thin films can act as trap sites in the devices²⁹ as shown in *Fig. 5*. As a result, the J_d values from the devices based on **H2** (abbreviated as **P-H2**) were considerably high in comparison with **P-H1** and **P-H3** devices. We examined the effect of the donor layer thickness on the OPD performance of the PHJ devices using **H1**. The resulting remilog J-V characteristics and EQE spectra were displayed in *Fig. 6*. The J_d values decreased with increased donor layer thickness, while the EQE value was reduced significantly at an active layer thickness of 40 nm. This suggests that exciton diffusion length (L_D) was shorter than the donor layer thickness, resulting in the reduced J_{ph} value.³⁰⁻³² These results implied that the photoactive layer thickness is crucial in controlling the performance of OPD devices. In general, BHJ devices showed improved J_d and EQE values compared to PHJ devices because excitons in BHJ devices are more probable to dissociate into free charge carriers within exciton lifetime due to larger interface area.³³⁻³⁵ The sensitivity of the OPD devices is mainly determined by J_d and EQE. The linear dynamic range (LDR) is expressed as;

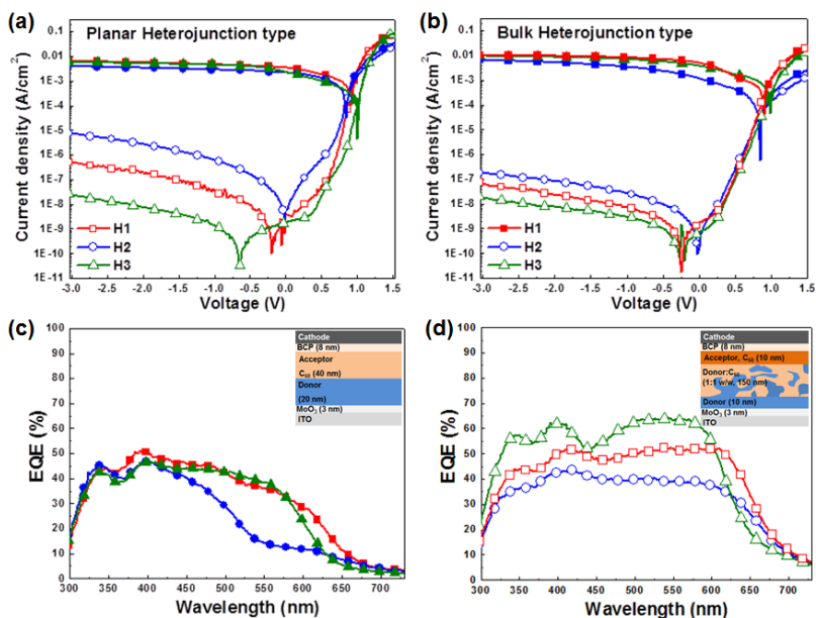


Fig. 4. J - V characteristics under dark (open symbols) and AM 1.5G illumination (open symbols) of (a) PHJ, (b) BHJ devices and EQE spectra of (c) PHJ, (d) BHJ devices at -3 V.

Table 3. Performance of the OPD devices with various donor molecules

@ -3 V	Donor molecules	$J_{d, best}$ (A/cm ²)	J_d (A/cm ²)	J_{ph} (A/cm ²)	D^* (cmHz ^{1/2} /W)	LDR (dB)	EQE (%) (@530 nm)
	H1	6.7×10^{-8}	4.9×10^{-7}	6.4×10^{-3}	2.2×10^{11}	82	40.7
PHJ	H2	3.4×10^{-6}	7.5×10^{-6}	2.1×10^{-3}	3.2×10^{10}	55	18.0
	H3	2.1×10^{-8}	3.4×10^{-8}	5.8×10^{-3}	6.5×10^{11}	107	40.2
	H1	3.2×10^{-8}	4.0×10^{-8}	1.0×10^{-2}	9.0×10^{11}	108	51.4
BHJ	H2	4.2×10^{-8}	2.2×10^{-7}	0.7×10^{-2}	2.8×10^{11}	92	41.0
	H3	8.8×10^{-9}	1.8×10^{-8}	9.6×10^{-2}	12.8×10^{11}	115	63.8

All the OPD devices were deposited by vacuum thermal evaporation.

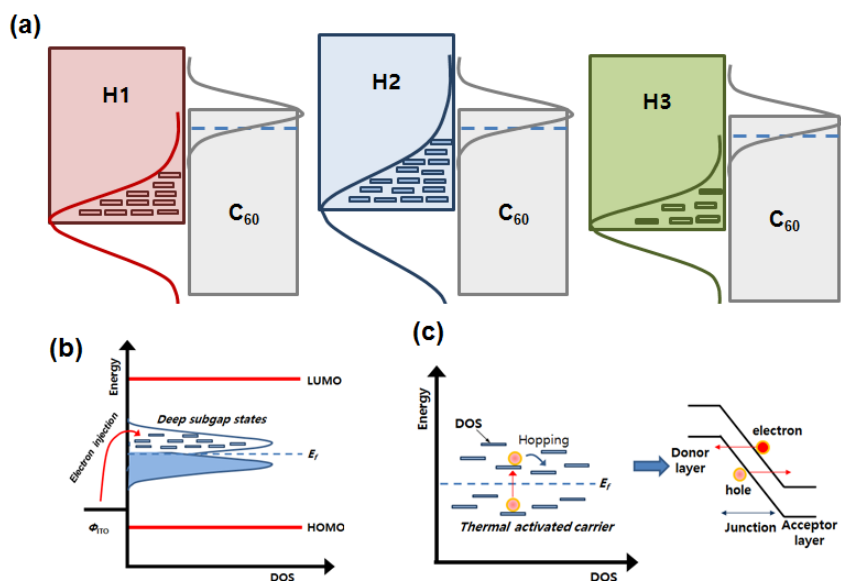


Fig. 5. (a) Schematic of density-of-states of donor molecules, (b) and (c) anticipated dark current mechanism of OPD devices.

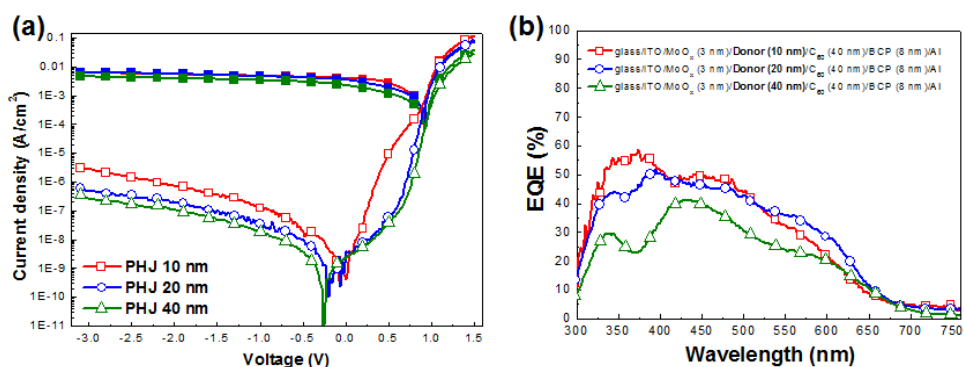


Fig. 6. (a) J–V characteristics under dark (closed symbol line) and under white light (open symbol line) and (b) EQE spectra at -3V. (rectangle: 10 nm of donor layer thickness, circle: 20 m of donor layer thickness, triangle: 40 nm of donor layer thickness)

$$\text{LDR} = 20 \log \frac{J_{ph}}{J_D} \quad (2)$$

OPD devices have a constant responsivity within LDR even with changing the intensity of incident light. The BHJ device based on **H3** showed a large LDR of 115 dB because of low J_a value, whereas the **H2**-based BHJ device produced an moderate LDR of 91.8 dB at the applied -3 V under the light intensity of 100 mWcm^{-2} . The EQE spectra of PHJ and BHJ devices obtained under a reverse bias of 0 V, -1 V, -2 V and -3 V can be used to quantify the efficiency of conversion of photons to current. According to the Onsager theory, applying a reverse bias to the devices increase the electrostatic potential barrier at the D/A interface so that free charge carrier density increases, resulting in enhanced maximum EQE values.^{25,36} Consequently, the EQE values were enhanced with increasing the applied reverse bias in the devices.

3.5 Analysis of J_a in PHJ OPD devices

Grazing-incidence wide-angle X-ray scattering (GIWAXS) measurements were performed to investigate the structural properties of neat and blend thin films which are photoactive layers, respectively. **Fig. 7** shows diffraction patterns of the neat thin films onto Si substrate along the in-plane direction. The diffraction patterns of **H2** show strong peaks at $q_{xy} = 0.755$ and 1.364 \AA^{-1} , in contrast, the diffraction pattern of **H1** shows weak peak at $q_{xy} = 1.508 \text{ \AA}^{-1}$ and that of **H3** shows no clear peak. These patterns indicate that only **H2** molecules form polycrystalline domains in the neat thin films, as discussed in **Fig 5**. Thus, both local energy states and trap sites can be induced with different type disordered or defects at the interfaces of domains.³⁷⁻³⁹ These results were in good agreement with the SEM images (**Fig 3**)

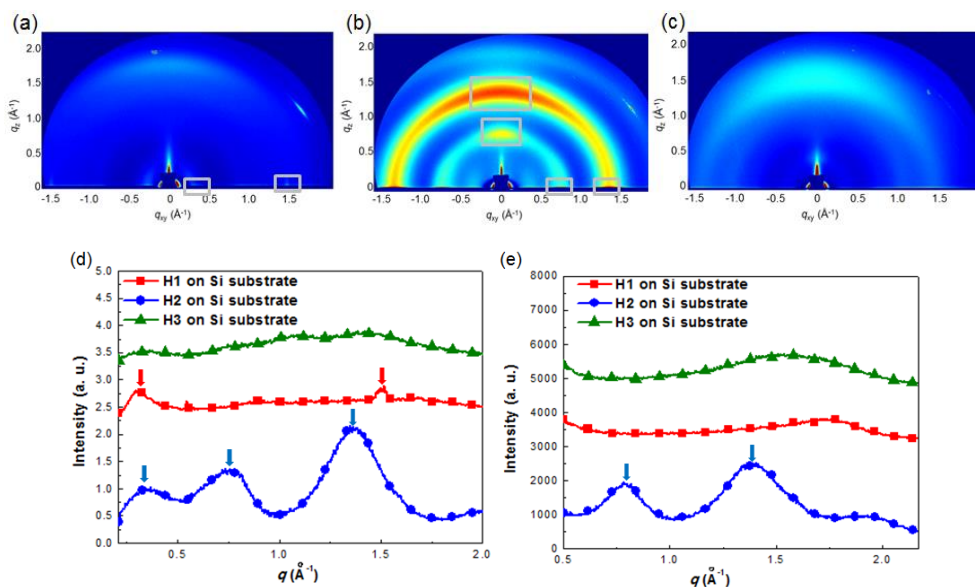


Fig. 7. 2D GIWAXS patterns of neat thin films of (a) **H1**, (b) **H2**, and (c) **H3**. Intensity integrals of (d) in-plane and (e) out-of-plane line cuts from 2D GIWAXS patterns.

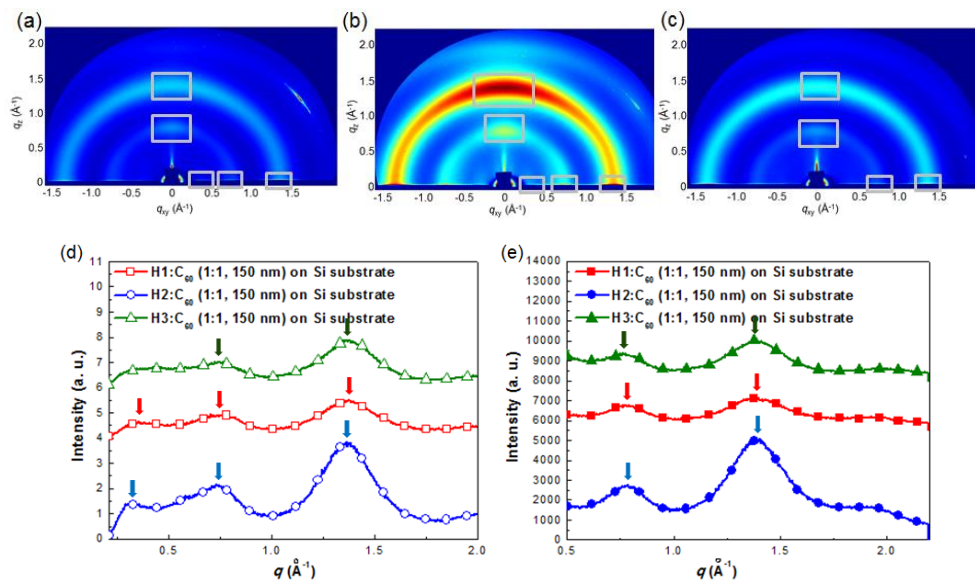


Fig. 8. 2D GIWAXS patterns of blend thin films (donor:C₆₀ 1:1) of (a) **H1**:C₆₀, (b) **H2**:C₆₀, and (c) **H3**:C₆₀. Intensity integrals of (d) in-plane and (e) out-of-plane line cuts from 2D GIWAXS patterns.

and high J_d values in OPD devices, and can provide insights into how the length of thiophene based on π -linker affects the molecular arrangement as well as crystallinity.^{40,41} On the other hand, the diffraction patterns of three blend films (1:1 volume ratio with C₆₀) exhibited clear peaks near $q_{xy} = 0.75$ and 1.374 \AA^{-1} as shown in **Fig 8**. The peak near $q_{xy} = 0.75 \text{ \AA}^{-1}$ is originated from the (111)-oriented C₆₀ face-centered cubic (FCC) phase ($q_{xy} = 0.769 \text{ \AA}^{-1}$), however, the peaks were observed at $q_{xy} = 0.753, 0.738$ and 0.760 \AA^{-1} in the patterns of **H1**:C₆₀, **H2**:C₆₀ and **H3**:C₆₀, respectively. The peak shift implies the change in lattice parameters of C₆₀ crystals in blend thin films. When the donor molecules were intercalated between C₆₀, the lattice parameters of C₆₀ were increased, leading to peak shift to smaller q value. This means that longer length of the donor molecules leads to larger peak shift of C₆₀ lattice. The values of peak shifts in the diffraction patterns were 0.016, 0.031, 0.009 \AA^{-1} in the blend thin films with **H1**, **H2** and **H3**, respectively. These peak shifts were consistent with the order of the π -linker length which was based on molecular structures as shown in **Fig 1**. The second diffraction peak near 1.37 \AA^{-1} can be discussed with packing of the donor molecules. Compared with diffraction patterns of neat thin films (only that of **H2** shows clear peaks), the peaks from packing of the donor molecules were observed in not only the pattern of **H2** but also the patterns of **H1** and **H3**. This indicates that in the blend thin films, C₆₀ induced molecular packing is enhanced, leading to phase separation. In addition, peak intensity indicates the higher crystallinity in **H2**:C₆₀ blend thin film compared with other thin films, indicating that the crystallinity of donor molecules affects the degree of intermixing with C₆₀. Thus, the different topography images were observed in blend thin films compared to neat thin films on AFM (**Fig. 3a-f**).

To analyze the electrical behavior of the PHJ devices, the semilog J - V characteristics measured under dark condition were plotted against internal built-in

potential as shown in **Fig. 9a** ($V_{\text{int}} = V_0 - V_{\text{bias}}$ where V_0 is the open-circuit voltage and V_{bias} is the applied voltage). The semilog J - V curves observed at above 0 V ($V_0 > V_{\text{bias}}$) were associated with shunt resistance (R_{sh}), thermally activated carriers at the D/A interface, or injected carriers from electrodes. The semilog J - V curves observed at below 0 V ($V_0 < V_{\text{bias}}$) were associated with series resistance (R_s). In the built-in potential $V_0 < V_{\text{bias}}$, the space charge limited current (SCLC) increased in the order of **P-H3** > **P-H1** > **P-H2**. However, the J_d values increased in the order of **P-H2** > **P-H1** > **P-H3** in the built-in potential $V_0 > V_{\text{bias}}$. To further study of J_d , electrochemical impedance spectroscopy (EIS) experiments were conducted for the PHJ devices base on different donor molecules without illumination at applied reverse bias of -2 V in **Fig. 9b**. In dark conditions, the semicircle in Nyquist plots include R_s , representing the outside circuit resistance at high frequency, and charge transfer resistance (R_{ct}), corresponding to the electron transfer between electrode and photoactive layer at low frequency.⁴² The R_{ct} values related to the J_d values of J - V characteristics as shown in **Fig. 9a** increased in order of **P-H2** (2.13 K Ω) > **P-H3** (10.8 K Ω). These results of GIWAXS and EIS experiments indicate that electrons were injected easily from ITO electrode to deep subgap states of **H2** donor molecules due to the low energy barrier, and then recombined as shown in **Fig. 5b**. Or the minority carriers were caused by thermal activation in deep subgap states of **H2** donor molecules, and then swept away from the p-n junction as shown in **Fig. 5c**. These phenomena cause the high J_d value in **P-H2**.

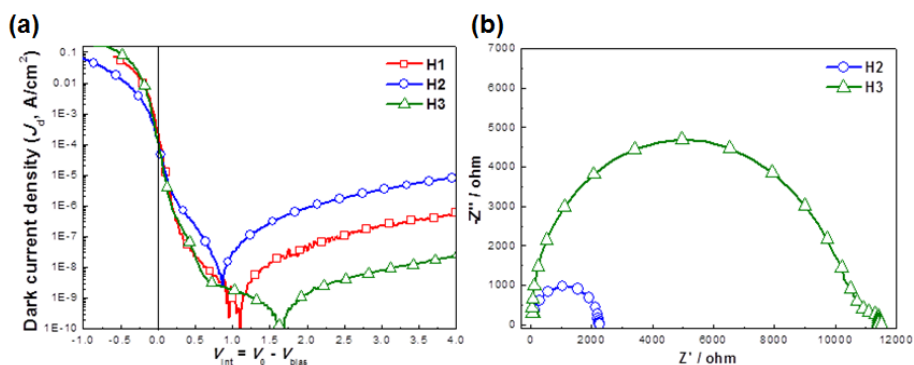


Fig. 9. (a) J - V characteristics as a function of internal built-in potential and (b) Nyquist plots (rectangle: **H1**, circle: **H2**, and triangle: **H3**). All PHJ devices were measured under dark condition.

4 Conclusion

In conclusion, we present how crystallinity and miscibility of donor and acceptor molecules affect the performance of OPD devices. Although synthesized three donor molecules denoted as **H1**, **H2** and **H3** have similar band gaps, HOMO and LUMO energy levels, the crystallinity and π - π packing were different in thin film due to the different π -linker structure. GIWAXS measurements revealed that **H3** having one thiophene as a π -linker for connecting electron-donating and electron-withdrawing units showed less intermolecular interaction than that of other donor molecules in thin films. As a result, BHJ OPD devices based on **H3**: C_{60} (1:1) exhibited broadband EQE value of 64% at 530 nm, low J_d value 1.54×10^{-8} Acm^{-2} , and high J_{ph} value of 9.57×10^{-3} Acm^{-2} at -3 V. The relatively high performance of OPD devices was attributed to amorphous domain system of the **H3** molecules in photoactive layer. These results provide an effective donor

molecular design and a strategy for reducing the J_d value to achieve high performance OPD devices.

5 References and Notes

- 1). R. D. Jansen-van Vuuren, A. Armin, A. K. Pandey, P. L. Burn and P. Meredith, *Adv. Mater.*, **2016**, *28*, 4766.
- 2). H. Dong, H. Zhu, Q. Meng, X. Gong and W. Hu, *Chem. Soc. Rev.*, **2012**, *41*, 1754.
- 3). N. Martino, D. Ghezzi, F. Benfenati, G. Lanzani and M. R. Antognazza, *J. Mater. Chem. B*, **2013**, *1*, 3768.
- 4). T. N. Ng, W. S. Wong, M. L. Chabinyk, S. Sambandan and R. A. Street, *Appl. Phys. Lett.* **2008**, *92*, 213303.
- 5). J. Schuster and E. Bellotti, *Appl. Phys. Lett.*, **2012**, *101*, 261118.
- 6). G. Konstantatos and E. H. Sargent, *Nat. Nanotechnol.*, **2010**, *5*, 391.
- 7). J. Miao, B. Meng, J. Liu and L. Wang, *Chem. Commun.*, **2018**, *54*, 303.
- 8). Z. Su, F. Hou, X. Wang, Y. Gao, F. Jin, G. Zhang, Y. Li, L. Zhang, B. Chu and W. Li, *ACS Appl. Mater. Interfaces*, **2015**, *7*, 2529.
- 9). S. Paek, H. Choi, C. Kim, N. Cho, S. So, K. Song, M. K. Nazeeruddin and J. Ko, *Chem. Commun.*, **2011**, *47*, 2874.
- 10). B. H. D. Zherebetsky, H. Wang, M. A. Kolaczowski, L. M. Klivansky, T. Tan, L. Wang and Y. Liu, *Chem. Sci.*, **2016**, *7*, 3857.
- 11). F. C. Spano. *Acc. Chem. Res.*, 2010, *43*, 429.

- 12). F. C. Spano .; C. Silva. *Annu. Rev. Phys. Chem.* 2014. 65, 477.
- 13). P. M. Beaujuge, C. M. Amb and J. R. Reynolds, *Acc. Chem. Res.*, **2010**, 43, 1396.
- 14). I. A. Howard, F. Laquai, E. P. Keivanidis, R. H. Friend and N. C. Greenham, *J. Phys. Chem. C*, **2009** , 113 , 21225.
- 15). J. J. Dittmer, E. A. Marseglia and R. H. Friend, *Adv. Mater.*, **2000**, 12 , 1270.
- 16). O. Ostroverkhova. *Chem. Rev.*, **2016**, 116, 13279.
- 17). M. Pope and C. E. Swenberg, *Electronic Processes in Organic Crystals and Polymers*. Oxford, 2 edition, **1999**.
- 18). C. M. Benavides, P. Murto, C. L. Chochos, V. G. Gregoriou, A. Avgeropoulos, X. Xiaofeng, K. Bini, A. Sharma, M. R. Andersson, O. Schmidt, C. J. Brabec, E. Wang and S. F. Tedde, *ACS Appl. Mater. Interface*, **2018**, 10, 12937.
- 19). H. C. LIM, J. -J. Kim, J. Jang and J.-I. Hong, *New J. Chem.*, **2018**, 42, 11458.
- 20). D. C. Coffey, B. W. Larson, A. W. Hains, J. B. Whitaker, N. Kopidakis, O. V. Boltalina, S. H. Strauss and G. Rumbles, *J. Phys. Chem. C*, **2012**, 116, 8916.
- 21). J.-I. Fujisawa, *Phys.Chem.Chem.Phys.*, **2015**, 1, 12228.
- 22). M. U. Munshi, G. Berden, J. Martens and J. Oomens, *Phys. Chem. Chem. Phys.*, **2017**, 19, 19881.
- 23). H. Zhou, L. Yang, S. C. Price, K. J. Knight and W. You, *Angew. Chem. Int. Ed.*, 2010, **49**, 7992.
- 24). R. He, L. Yu, P. Cai, F. Peng, J. Xu, L. Ying, J. Chen, W. Yang and Y. Cao, *Macromolecules*, **2014**, 47, 2921.

- 25). P. E. Keivanidis, P. K. H. Ho, R. H. Friend and N. C. Greenham, *Adv. Funct. Mater.*, **2010**, *20*, 3895.
- 26). J. A. Carr and S. Chaudhary, *Energy Environ. Sci.*, **2013**, *6*, 3414.
- 27). C. J. Brabec, M. Heeney, I. McCulloch and J. Nelson, *Chem. Soc. Rev.*, **2011**, *40*, 1185.
- 28). R. S. Ashraf, B. C. Schroeder, H. A. Bronstein, Z. Huang, S. Thomas, R. J. Kline, C. J. Brabec, P. Rannou, T. D. Anthopoulos, J. R. Durrant and I. McCulloch, *Adv. Mater.*, **2013**, *25*, 2029.
- 29). W. J. Potscavage, S. Yoo and B. Kippelen, *Appl. Phys. Lett.*, **2007**, *91*, 013508.
- 30). R. R. Lunt, J. B. Benziger and S. R. Forrest, *Adv. Mater.*, **2010**, *22*, 1233.
- 31). D. Kurrle and J. Pflaum, *Appl. Phys. Lett.*, **2008**, *92*, 133306.
- 32). M. Shtein, J. Mapel, J. B. Benziger and S. R. Forrest, *Appl. Phys. Lett.*, **2002**, *81*, 268.
- 33). F. Padinger, R. S. Rittberger, and N. S. Sariciftci, *Adv. Funct. Mater.*, **2003**, *13*, 85.
- 34). G. F. Burkhard, E. T. Hoke, Z. M. Beiley and M. D. McGehee, *J. Phys. Chem. C*, **2012**, *116*, 26674.
- 35). O. V. Mikhnenko, P. W. M. Blom and T.-Q. Nguyen, *Energy Environ. Sci.*, **2015**, *8*, 1867.
- 36). C. L. Braun, *J. Chem. Phys.*, **1984**, *80*, 4157.
- 37). J. H. Kang, D. A. da Silva Filho, J. L. Bredas and X.-Y. Zhu, *Appl. Phys. Lett.*, **2005**, *86*, 152115.
- 38). J. Rivany, L. H. Jimison, J. E. Northrup, M. F. Toney, R. Noriega, S. Lu, T. J. Marks, A. Facchetti and A. Salleo. *Nature Mater.*, **2009**, *8*, 952-958.

- 39). H. C. Lim, S. H. Min, E. Lee, J. Jang, S. H. Kim and J.-I. Hong, *ACS Appl. Mater. Interface*, **2015**, 7, 11069-11073.
- 40). M.-S. Choi, T.-M. Kim, H.-S. Shim, B.-S. Kim, H. J. Kim and J.-J. Kim, *ACS Appl. Mater. Interface*, **2015**, 7, 9134.
- 41). J. Rivnay, S. C. B. Mannsfeld, C. E. Miller, A. Salleo and M. F. Toney, *Chem Rev.*, **2012**, 112, 5488.
- 42). H. Wang, S. Xing, Y. Zheng, J. Kong J. Yu and A. D. Taylor, *ACS Appl. Mater. Interface*, **2018**, 10, 3856.

Section 3. Photocrosslinkable Oligothiophene for Hole Transport Layer in Organic Photovoltaic Devices

Abstract

Photocrosslinkable small molecule, 5T-p as hole transport material, was synthesized and characterized for solution-processed bulk heterojunction (BHJ) organic photovoltaic (OPV) devices. The 5T-p structure consisted of diacetylene as a photocross linker and quinquethiophene as a π -conjugated backbone. The photopolymerization of 5T-p thin films was controlled by irradiation time of UV light. The morphology and thickness of thin films were confirmed by atomic force microscope (AFM). Although the thin film as a hole transport layer was unfavourable due to improper crosslinking network morphology, photocrosslinking strategy based on small molecule was shown for the potential of the application to the organic electronic devices.

Keywords: Photocrosslinking, diacetylene, hole transport, bulk heterojunction, organic photovoltaic

1 Introduction

Organic photovoltaics (OPVs) have attracted over the past few decades due to the advantages of flexibility, low cost fabrication, and simple manufacturing.¹⁻³ The OPV devices is required to hole transport layer (HTL) between the transparent anode and the active layer to overcome issues arising from poor adhesion to organic and inorganic materials and the surface roughness of anode.⁴⁻⁶ In generally, conducting polymer (PEDOT:PSS) and metal oxide (MoO_3) are mainly used for the HTL in the OPV devices.^{7,8} However, PEDOT:PSS has a disadvantage due to i) high acidity (pH 2.5), ii) hydrophilic of PSS, resulting in corrosion of electrode and absorption of moisture. The reliability of the device is deteriorated.⁹⁻¹¹ On the other hand, the thin film of metal oxide by the vacuum deposition method is complicated process.¹²⁻¹³ The solution of these problems is essential for developing high efficient OPV devices. Therefore, new conducting materials are needed to replace PEDOT:PSS or metal oxides. Photocrosslinking agents have attracted attention since polymerization can be easily performed by UV irradiation or thermal treatment without chemical initiator or catalysts.¹⁴⁻¹⁶ Among them, polydiacetylene (PDA) prepared by the UV irradiation of self-assembled diacetylene monomers is useful due to the several intriguing structural and optical properties. The PDA has alternating double- and triple-bond groups in the main backbone structure and crosslinking concept is simple and powerful to make easily thin films from various solvents.¹⁷⁻¹⁹ However, the introduction of diacetylene units in π -conjugated backbone can disturb their π - π stacking, resulting in reducing electrical conductivity.²⁰⁻²¹ The development of materials without deteriorate electrical properties remains a challenge.

In this letter, we present small molecules photocrosslinkable material by using quinquethiophene (five-membered thiophene rings) end-capped with diacetylene moieties as a photocrosslinker and systematically explored the photophysical properties and the morphology of the thin film according to the degree of photopolymerization. We also investigated to apply thin film as a HTL layer of the bulk heterojunction (BHJ) OPV devices fabricated by blending the P3HT as an donor with [6,6]-phenyl-C₆₁-butyric acid methyl ester (PC₆₁BM) as the acceptor for the BHJ structure based active layer.

2 Experimental Methods

2.1 Synthetic Procedure

3,3''',3''''-4'-tetrahexyl-2,2':5',2'':5'',2''':5''',2''''-quinquethiophene (compound 3) was prepared according to the literature procedure.²²

3,3''',3''''-4'-tetrahexyl-[2,2':5',2'':5'',2''':5''',2''''-quinquethiophene]-5,5''''-dicarbaldehyde (compound 4) ¹H NMR (300 MHz, CDCl₃, ppm) δ: 9.85 (s, 2H), 7.61 (s, 2H), 7.16 (d, 4H, 1.8 Hz), 2.84 (dd, 8 H, 6.4, 8.2 Hz), 1.72 (m, 8H), 1.36 (m, 24H), 0.92 (dd, 12H, 4.9, 1.8 Hz).

6-propoxyhexa-2,4-diyne-1-ol (compound 5) ¹H NMR (300 MHz, CDCl₃, ppm) δ: 4.37 (s, 2H), 4.24 (s, 2H), 3.49 (t, 2H, 6.7 Hz), 1.65 (m, 2H), 0.96 (t, 3H, 7.4 Hz).

6-propoxyhexa-2,4-diynyl 2-cyanoacetate (compound 6) ¹H NMR (300 MHz, CDCl₃, ppm) δ: 4.90 (s, 2H), 4.24 (s, 2H), 3.54 (s, 2H), 3.49 (t, 2H, 6.7 Hz), 1.64 (m, 2H), 0.95 (t, 3H, 7.4 Hz).

bis(6-propoxyhexa-2,4-diyn-1-yl) 3,3'-(3,3''',3''',4'-tetrahexyl-[2,2':5',2'':5'',2''':5''',2''''-quinguethiophene]-5,5''''-diyl)(2E,2'E)-bis(2-cyanoacrylate) (5T-p) ¹H NMR (300 MHz, CDCl₃, ppm) δ: 8.26 (s, 2H), 7.62 (s, 2H), 7.24 (s, 2H), 7.19 (s, 2H), 4.98 (s, 4H), 4.36 (s, 4H), 3.49 (t, 6H, 6.5 Hz), 2.85 (dd, 6H, 7.1 Hz), 1.65 (m, 16H), 1.36 (m, 18H), 0.95 (t, 18H, 7.5 Hz) ¹³C NMR (75 MHz, CDCl₃, ppm) δ: 140.44, 139.30, 137.53, 136.31, 135.04, 134.21, 134.27, 134.10, 134.02, 132.22, 128.55, 127.96, 125.37, 96.21, 94.89, 72.19, 71.78, 71.84, 69.42, 58.40, 53.82, 31.69, 31.60, 31.54, 30.37, 30.05, 29.81, 28.45, 29.31, 29.22, 22.66, 22.61, 14.42, 10.28.

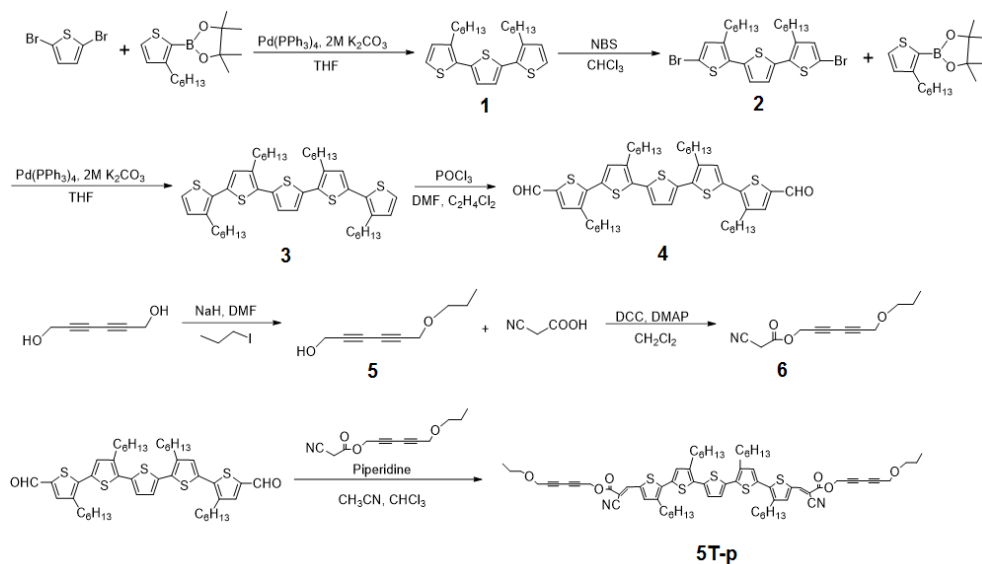
2.2 Organic Photovoltaic Devices Preparation

Device configuration of ITO/PEDOT:PSS or **5T-p**/P3HT:PC₆₁BM (2 wt%, 1:0.8 w/w)/LiF/Al was used to investigate the OPV device performance. Pre-patterned indium tin oxide (ITO, 13 ohm/sq) on glass was cleaned by sequential ultrasonication in deionized water (10 min), isopropyl alcohol (IPA) (10 min), followed by UV ozone treatment for 5 min. **5T-p** was spin-coated onto ITO to prepare hole transport layer (HTL). Photopolymerization was performed using a UV handy lamp (4 W), set to emit 254 nm light, the lamp positioned (within 5 cm) from the substrates, followed by thermal curing at 120 °C, 20 min. A reference device using

PEDOT:PSS (P) for the HTL was fabricated, and treated post-annealing process at 120 °C, 20 min in a glove box. Finally, LiF (1 nm) and Al (100 nm) were thermally evaporated under 10^{-6} torr as cathode electrode. The active area is 4 mm². The current-voltage characteristics of OPV devices were determined using a Keithley 2400 source meter and an AM1.5 simulated white light source.

3 Results and Discussion

The 5T-p molecule was synthesized according to Scheme 1 and fully characterized using ¹H NMR and ¹³C NMR. Quinquethiophene and diacetylene moieties at both ends were used as a π -conjugation main backbone and as a photocrosslinker, respectively. Optical properties of **5T-p** were investigated by UV/vis absorption spectroscopy in dichloromethane solution (λ_{max} : 493 nm, ϵ : 6.0×10^4) and in spin-cast thin films (λ_{max} : 586 nm) as shown **Fig. 1(a)**. Electrochemical experiment of **5T-p** was performed using cyclic voltammetry (CV). Two quasi-reversible oxidative processes were observed in tetrabutylammonium hexafluorophosphate (0.1 M TBAPF₆) as a supporting electrolyte in dichloromethane solution at a scan rate of 0.05 V/s (**Fig. 1(b)**). The first oxidation potential (E°_{ox}) of **5T-p**, estimated by the onset potential, was 0.52 eV versus the ferrocene/ferrocenium redox couple (Fc/Fc⁺).²³ Redox reactions showed that the peak current ratio ($i_{\text{pc}}/i_{\text{pa}}$) and peak-to-peak separation (ΔE_{pp}) for **5T-p** were 0.91 and 0.06 V. HOMO (5.32 eV) and LUMO (3.38 eV) levels of **5T-p** were calculated from CV measurements and absorption spectra. **5T-p** was spun cast from dichloromethane solution to produce thin film on ITO/glass substrate.



Scheme 1. Synthesis of **5T-p**

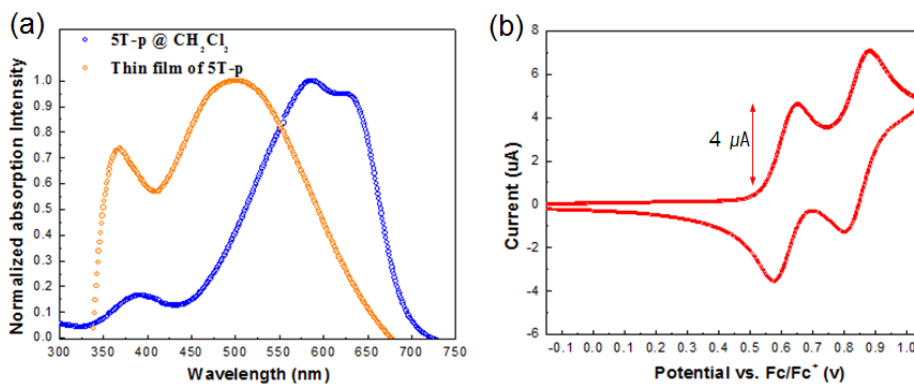


Fig. 1. Normalized UV/vis absorption spectra of (a) **5T-p**, and (b) cyclic voltammograms of **5T-p** in dichloromethane solution with tetrabutylammonium hexafluorophosphate (0.1 M TBAPF_6) as a supporting electrolyte at a scan rate of 0.05 V/s .

Red-shifted absorption spectrum was observed in spin-cast thin film due to the stronger intermolecular interactions in solid state, compared to the solution state. As expected, the polymerized **5T-p** molecules in thin film by UV irradiation with 254 nm for 30 min showed blue-to-red color changing, arising from the lowest π -electronic transition of conjugated backbone as shown *Fig. 1(a)* and *Fig. 2(a)* (see inserted digital camera image). The stress-induced chromic transition occurs by linked together between C1 and C4 carbon atoms of adjacent diacetylene moieties as photopolymerization progresses.¹⁷ The absorption spectra changing were observed with the treatment time of continuous UV irradiation. The absorption peak at 586 nm gradually decreased and blue-shifted (from 586 nm to 502 nm) is observed, relating to the H-aggregation of the polymerized **5T-p** molecules (*Fig. 2(a)*). The absorption intensity of thin films after washing treatment by chlorobenzene solution can be used to monitor the degree of polymerization as a function of reaction time with UV light as shown *Fig. 2(b)*. Although the absorption intensity was decreased after washing of the thin film due to the removal of 5T not formed photopolymerization, the thin film was sustained at a certain thickness regardless of

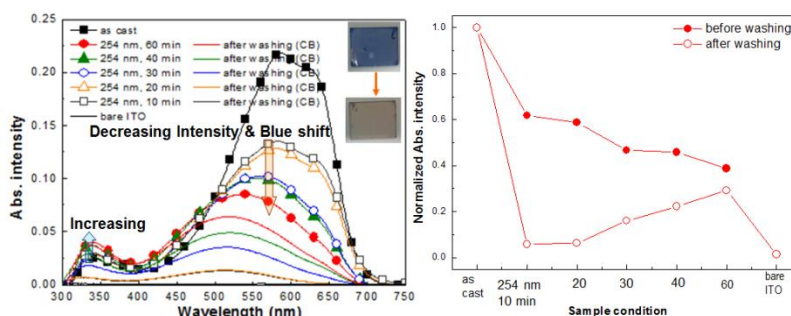


Fig. 2. UV/vis absorption spectra of (a) photopolymerized **5T-p** thin films (closed symbols: photopolymerized thin films and line: after chlorobenzene washing of thin films) and (b) absorption intensity of the thin films with 254 nm UV irradiation time.

the number of washing cycles, resulting in the constant absorption intensity. The results implied that once photopolymerization is formed on the substrate, it is insoluble in all common solvents and provide the potential of the solution-processed thin film without damaging of the layer. These phenomena coincide with tapping mode AFM images of thin films as shown **Fig. 3**. The obtained surface morphology images corroborate the presence of the polymerized **5T-p** molecules layer and significantly different from the bare ITO surface. In addition, the thickness of the remaining layer after the washing treatment was increased and the surface roughness was also decreased due to the polymerized thin layer. The results consisted with the changing intensity of absorption spectra. Although the color transition by polymerization was also observed only thermal annealing at 120 °C for 30 and 60 min, the absorption intensity was dramatically decreased after washing treatment with chlorobenzene. It means that polymerization of 5T-p molecules in thin film seems to be has proceeded unevenly compared to UV irradiation method.

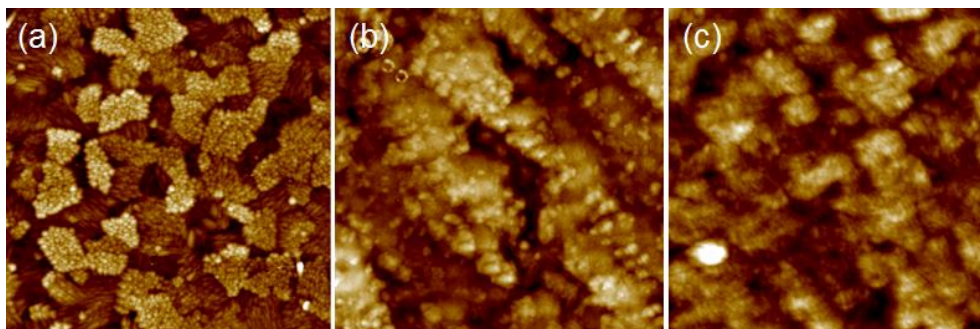


Fig. 3. AFM topographic image of (a) bare ITO only and (b) without thermal treatment , (c) with thermal treatment (120 °C, 20 min) of photopolymerized thin film after UV irradiation (254 nm, 60 min)

Table 1. Photovoltaic Performance of OPVs with various HTLs^a

Devices	V_{oc} (V)	J_{sc} (mAcm ⁻²)	FF	PCE (%)
Pristine (PEDOT:PSS)	0.59	12.01	0.55	3.86
Photopolymerization thin film	0.47	0.07	0.25	0.01
PEDOT:PSS/Photopolymerization thin film	0.34	0.25	0.24	0.02

^a The device structure in all cases is ITO/HTL/P3HT:PC₆₁BM (2 wt%, 1:0.8 w/w)/LiF/Al.

The photopolymerized thin films were prepared with 60 min exposure at 254 nm UV handy lamp followed by thermal annealing at 120 oC, 20 min for use as a HTL layer of BHJ OPV devices. The photoactive layers consisted of P3HT as a donor and PC₆₁BM as an acceptor, blended in a 2 wt% and 1:0.8 w/w ratio. The figure of merit, such as the open circuit voltage (V_{oc}), short-circuit current (J_{sc}), fill factor (FF), and power conversion efficiency (PCE), are summarized in Table 1. The BHJ OPV devices based on the photopolymerization thin films employed in this study were found to be significantly low efficient than those based on PEDOT:PSS. This is because the polymerized **5T-p** materials with low electrical mobility exhibiting low hopping distance of the charge carriers. These results indicate that the thin film morphology of HTL has significant influence on the device performance.

4 Conclusion

We designed and synthesized functionalized small molecules consisting of diacetylene moieties as a photocrosslinker and quinquethiophene as a p-

conjugation backbone. It was found that the degree of photopolymerization in thin films was obtained with the reaction time of UV irradiation. Although the photopolymerized thin films as a HTL of BHJ OPV devices show lower device performance than that of PEDOT:PSS, it appears that the elaborate design of photocrosslinking strategy based on small molecule should be considered for the potential of the application to the organic electronic devices.

5 References and Notes

- 1). M. Hirade, T. Yasuda and C. Adachi, *J. Phys. Chem. C*, **2013**, *117*, 4989.
- 2). H. Kim, B. H. Lee, K. C. Lee, G. Kim, J. Y. Yu, N. Kim, S. H. Lee and K. Lee, *Adv. Energy. Mater.*, **2013**, *3*, 1575.
- 3). G. He, Z. Li, X. Wan, Y. Liu, J. Zhou, G. Long, M. Zhang and Y. Chen, *J. Mater. Chem.*, **2012**, *22*, 9173.
- 4). H. C. Lim, S. H. Min, E. Lee, J. Jang, S. H. Kim and J.-I. Hong, *ACS Appl. Mater. Interfaces*, **2015**, *7*, 11069.
- 5). C. Gong, H. B. Yang, Q. L. Song, Z. S. Lu and C. M. Li, *Sol. Energy Mater. Sol. Cells*, **2012**, *100*, 115.
- 6). J. Ouyang, C. W. Chu, F. C. Chen, Q. Xu and Y. Yang, *Adv. Funct. Mater.*, **2005**, *15*, 203.
- 7). Y. Xia and J. Ouyang, *J. Mater. Chem.*, **2011**, *21*, 4927.
- 8). X. Crispin, F. L. E. Jakobsson, A. Crispin, P. C. M. Grim, P. Adersson, A. Volodin, C. van Haesendonck, M. Van der Auweraer, W. R. Salaneck and M. Berggren, *Chem. Mater.*, **2006**, *18*, 4354.

- 9). H. Okuzaki, H. Suzuki and T. Ito, *J. Phys. Chem. B*, **2009**, *113*, 11378.
- 10). U. Lang, N. Naujoks and J. Dual, *Synth. Met.*, **2009**, *159*, 473.
- 11). V. Shrotriya, G. Li, Y. Yao, C. W. Chu and Y. Yang, *Appl. Phys. Lett.*, **2006**, *88*, 073508.
- 12). R. Lampande, G. W. Kim, J. Boizot, Y. J. Kim, R. Pode and J. H. Kwon, *J. Mater. Chem. A*, **2013**, *1*, 6895
- 13). T. Hori, T. Shibata, V. Kittichungchit, H. Moritou, J. Sakai, H. Kubo, A. Fujii and M. Ozaki, *Thin Solid Films*, **2009**, *518*, 522.
- 14). J.-M. Kim, Y. B. Lee, S. K. Chae and D. J. Ahn, *Adv. Funct. Mater.*, **2006**, *16*, 2103.
- 15). L. Valentini, D. Bagnis, A. Marrocchi, M. Seri, A. Taticchi and J. M. Kenny, *Chem. Mater.*, **2008**, *20*, 32.
- 16). S. Khiev, L. Derue, G. Ayenew, H. Medlej, R. Brown, L. Rubatat, R. C. Hiorns, G. Wantz and C. D. Lartigau, *Polym. Chem.*, **2013**, *4*, 4145.
- 17). B. Yoon, S. Lee and J.-M. Kim, *Chem. Soc. Rev.*, **2009**, *38*, 1958.
- 18). H. Ringsdorf, B. Schlarb and J. Venzmer, *Angew. Chem., Int. Ed. Engl.*, **1988**, *27*, 113.
- 19). M. A. Reppy and B. A. Pindzola, *Chem. Commun.*, **2007**, 4317.
- 20). B. J. Kim, Y. Miyamoto, B. Ma and M. J. Fréchet, *Adv. Funct. Mater.*, **2009**, *19*, 2273.
- 21). M. M. Alam, S. A. Jenekhe, *Chem. Mater.*, **2004**, *16*, 4647.
- 22). Y. Liu, X. Wan, F. Wang, J. Zhou, G. Long, J. Tian, J. You, Y. Yang and Y. Chen, *Adv. Energy. Mater.*, **2011**, *1*, 771
- 23). H. Zhou, L. Yang, S. C. Price, K. J. Knight and W. You, *Angew. Chem. Int. Ed.*, **2010**, *49*, 7992.

Section 4. Self-Assembled Carbon Dot/Poly(3,4-ethylenedioxythiophene):Poly(styrene sulfonate) Organogels for Efficient Charge Transport in Photovoltaic Devices

Abstract

We report the self-assembly of poly(3,4-ethylene dioxothiophene):poly(styrene sulfonate) (PEDOT:PSS) organogel films incorporating carbon dots (C-dots). Owing to the electrostatic interaction between the C-dots and the PEDOT chains, C-dots@PEDOT core-shell nanostructures are readily formed. We demonstrate that the C-dots affect the reorientation of PEDOT chains and the formation of interconnected structure of PEDOT-rich domains, improving the charge transport pathway. The power conversion efficiency of the organic photovoltaic device containing the self-assembled organogel as the hole extraction layer (HEL) was 26% higher than the device with pristine PEDOT-PSS as the HEL.

Keywords: Self-assembly, organogel, PEDOT:PSS, Carbon dots, organic photovoltaic

1 Introduction

Organic photovoltaics (OPVs) have drawn much attention as potential next-generation renewable energy sources on account of low production costs and solution processability, which make mass production of OPVs viable.¹⁻⁴ To fabricate OPVs, poly(3,4-ethylenedioxythiophene):poly(styrene sulfonate) (PEDOT:PSS) is inserted as the hole extraction layer (HEL) between the anode and the active layer to overcome issues arising from energy level alignment and the surface roughness of anode.⁵⁻⁸ However, PEDOT:PSS shows poor electrical properties because the PSS chains, which are the counterions of PEDOT, are insulators. The electrical properties of PEDOT:PSS are usually improved by solvent or acid treatment,⁹⁻¹³ annealing,^{14,15} and by adding organic compounds¹⁶⁻¹⁸ affecting the orientation of the PEDOT chains within the matrix, leading to expanded-coil conformation that strengthen interactions between the PEDOT chains. These strategies focus on increasing the conductivity of PEDOT:PSS by controlling the PEDOT chain orientation, but unfortunately the improvement of OPV performance was not directly proportional to the increase in conductivity. Thus, fine-tuning the orientation and morphology of PEDOT:PSS to improve electrical percolation pathways for achieving optimized device efficiency remains a challenge.

Recently, graphene oxide (GO), a two-dimensional carbon allotrope, has been used to improve the electrical properties of PEDOT:PSS by gelation,¹⁹⁻²¹ although GO by itself is insulating. These studies indicate that GO can also act as an effective additive for PEDOT:PSS, however, the aggregation of large-sized GO sheets and their wide size distribution make it difficult to achieve the fine-tuning of the electrical properties of PEDOT:PSS for practical applications. In this letter, we

report the synthesis of PEDOT:PSS organogels incorporating relatively uniform-sized carbon dots (C-dots). The C-dots can act as a physical linker among PEDOT chains through electrostatic interaction, resulting in the formation of core-shell nanostructure. The nanoscopic morphology and orientation of PEDOT:PSS in the organogel were investigated to clarify the influence of the incorporation of C-dots on their electrical properties. The PEDOT:PSS films containing the C-dots were subsequently used as the HEL in a typical poly(3-hexylthiophene) (P3HT):[6,6]-phenyl-C₆₁-butyric acid methyl ester (PCBM) bulk heterojunction OPV.

2 Experimental Methods

2.1 Synthetic Procedure

Preparation of Carbon Dots (C-dots)

Carbon nanofibers (NEXCARB-H, 0.30 g) were added into a mixture composed of concentrated H₂SO₄ (60 mL) and HNO₃ (20 mL), followed by sonication for 2 h and continuous stirring for 1 day at 120 °C. After cooling and dilution with deionized (DI) water, the solution was neutralized with Na₂CO₃. The C-dots were isolated through size-selective precipitation by centrifugation at 12,000 rpm for 30 min. Ethanol was added into the supernatant solution with a volume ratio of 2:1, and then the solution was centrifuged under the same conditions. This process was repeated three times to obtain uniform-sized C-dots. The supernatant of C-dots solution was further dialyzed and dispersed into isopropyl alcohol (IPA). All reagents and solvents used in this study were commercially available and used without further purification.

Preparation of PEDOT:PSS Organogel with C-dots

IPA was added into PEDOT:PSS (CLEVIOS PH500) aqueous solution (3:7, v/v) so as to be miscible with the C-dot solution. The C-dots (0.19 wt% into IPA) solutions were injected into the PEDOT:PSS solution and allowed to stand for 1 h to produce the organogel. The C-dots solutions were introduced into the PEDOT:PSS solution with two different volume fractions (20 and 50% v/v).

2.2 Fabrication of Organic Photovoltaic Devices

Device configuration of ITO/hole extraction layer (HEL)/P3HT:PCBM/LiF/Al was used to investigate the effect of the incorporation of C-dots into the HEL on the charge transport in the devices. Pre-patterned indium tin oxide (ITO, 13 ohm/sq) on glass was cleaned by carrying out sequential ultrasonication in DI water (10 min), IPA (10 min), and IPA at 80 °C (5 min), followed by UV ozone treatment for 10 min. PEDOT:PSS organogels were spin-coated onto ITO with 4000 rpm for 40 s in order to prepare the HELs, and then a post-annealing process was conducted at 120 °C for 20 min. P3HT:PCBM (1:0.8 w/w) chlorobenzene solution (2.0 wt%) was spin-coated onto the HEL with 2000 rpm for 30 s in a glove box and then annealed at 150 °C for 10 min. Finally, LiF (1 nm) and Al (100 nm) as the cathode electrode were thermally evaporated under 10^{-6} torr. The active area is 4 mm².

2.3 Instruments

Atomic force microscopy (Veeco, NanoScope IV) images were acquired in non-contact mode at a scan rate of 1 Hz under ambient atmosphere. All of the samples were prepared by spin-casting onto SiO₂/Si wafers. Ultraviolet

photoemission spectroscopy (UPS, Hitachi AC-2) was carried out for the work functions measurement of the HEL of the samples. X-ray diffraction patterns were obtained by a Bruker D8 advance diffractometer, with a Cu K α X-ray source (40 kV, 40 mA) and a LYNXEYE XE detector with a 0.02 step/s scan rate. A focused ion beam (FIB, FEI Helios 650) was used for acquiring cross sectional images of the samples. Thin film specimens with a thickness of 100 nm were prepared for TEM analysis with lift-off method using a nanomanipulator (Omniprobe). HRTEM (JEOL JEM-2100, 3010) and HAADF-STEM (FEI Technai F20) were performed at 200 kV for acquisition of cross-sectional images of the organogels. The current–voltage characteristics were determined by using a Keithley 2400 source meter and an AM1.5 simulated white light source.

3 Results and Discussions

The pristine C-dots were fabricated from carbon nanofibers (CNFs) via excess oxidation and size-selective precipitation. The as-synthesized C-dots with a diameter of about 8–10 nm were characterized by high-resolution transmission electron microscopy (HRTEM) in *Fig. 1(d)*. The results are consistent with structures previously reported.²² The organogel was prepared by mixing a C-dots (0.19 wt%)-isopropyl alcohol (IPA) solution with a 70 vol% aqueous solution of PEDOT:PSS (CLEVIOS PH500) in IPA. The mixture was left undisturbed for 1 h. Consequently, the PEDOT:PSS solution readily formed viscous organogels, as shown in *Fig. 2(b)*. The prepared organogels are termed as ogC-dots_{0.2} and ogC-dots_{0.5} with the subscripts denoting the volume fraction of the C-dots solution. As a control, pristine PEDOT:PSS sample was also treated with IPA and prepared with

the same procedure without C-dots. **Fig. 2(c)** and **(d)** show the cross-sectional high-angle annular dark-field scanning TEM (HAADF-STEM) image of the organogel films obtained by drying the solvent. Interestingly, the results indicate the formation of core-shell nanostructure (CSNS) with an average diameter of about 12 nm in the organogel, while the pristine PEDOT:PSS only had a granular structure of the PEDOT:PSS agglomeration in the matrix.^{12,23} Owing to the high C-dots content in PEDOT:PSS, ogC-dots_{0.5} showed more aggregated CSNSs than ogC-dots_{0.2}, although their morphologies were similar. It is noteworthy that the core size of the CSNSs is almost identical to the as-synthesized C-dots diameter. Since the HAADF-STEM image of as-synthesized C-dots only shows a particle-like structure and the brightness of the HAADF-STEM image is proportional to the sample thickness and the square of the atomic number,²³ it is obvious that the bright shell (ca. 2.5 nm in thickness) in the HAADF-STEM images indicates the agglomeration of PEDOT:PSS chains on the C-dots in **Fig. 1(b)**, and schematic image of C-dots@PEDOT CSNS in **Fig. 1(a)**.

To clarify the PEDOT:PSS agglomeration, X-ray diffraction (XRD) patterns of PEDOT:PSS films obtained with various volume fractions of C-dots solutions were acquired, as shown in **Fig. 3(a)**. The pristine PEDOT:PSS film exhibited two

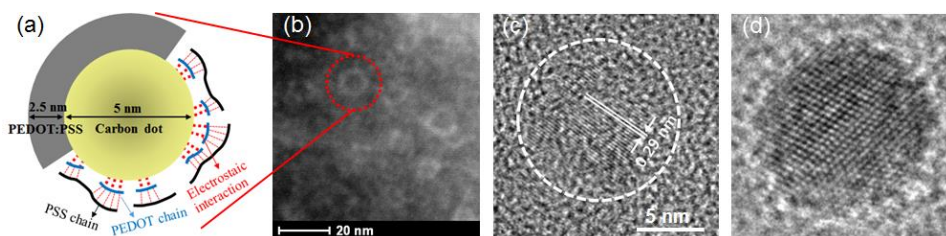


Fig. 1. (a) Schematic image, (b) high-angle annular dark-field scanning TEM (HAADF-STEM) of C-dots@PEDOT CSNS and high-resolution transmission electron microscopy (HRTEM) image of (c) the as-synthesized C-dots, (d) C-dots@PEDOT CSNS

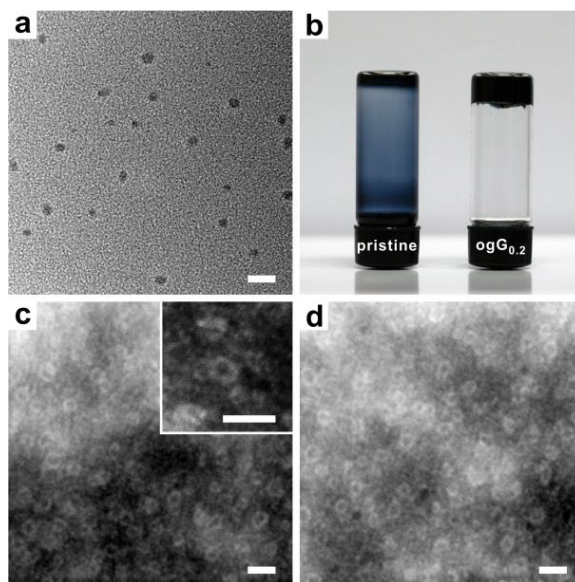


Fig. 2. (a) High-resolution transmission electron microscopy (HRTEM) image of the as-synthesized C-dots. (b) Photograph of the pristine PEDOT:PSS and the self-assembled organogel. Cross-sectional high-angle annular dark-field scanning TEM (HAADF-STEM) images of (c) ogC-dots_{0.2} and (d) ogC-dots_{0.5} PEDOT:PSS organogel with 20 vol% and 50 vol% C-dots solution, respectively. The inset shows the magnified the core-shell nanostructures (CSNSs). All the scale bars are 20 nm.

broad peaks at $2\theta = 25.8^\circ$ and 18.0° , which correspond to the π - π interchain stacking of PEDOT and the amorphous halos of PSS chains, respectively.^{12,24} In the case of the organogel with C-dots, the XRD patterns indicate a significant increase in the peak intensity at $2\theta = 3.5^\circ$ and 25.8° , representing the enhancement of the crystalline structure along the (100) and (010) lattices, corresponding to the lamella stacking and interchain stacking of PEDOT chains, respectively.²⁵ With increase in the C-dots solution volume fraction, the crystallinity of the PEDOT interchain stacking (d -spacing = 3.5 Å) gradually increased; however, the crystallinity corresponding to the lamella stacking of PEDOT showed no significant difference

in terms of the peak intensity. Notably, the peak intensity at $2\theta = 18.0^\circ$, corresponding to the interchain stacking of PSS chains reduced after the addition of C-dots. The intensity ratio of the peaks at $2\theta = 25.8^\circ$ and 18.0° (i.e., the ratio of the interchain stacking of PEDOT to PSS) was about four times larger than that shown by samples without C-dots. From these results, the agglomeration of PEDOT:PSS chains onto the C-dots might mainly lead to ordered crystalline PEDOT with interchain π - π stacking. Thus, the bright shell in the HAADF-STEM images indicates the agglomeration of the stacked PEDOT chains on the surface of the C-dots. We propose a model to explain the formation of the C-dots@PEDOT CSNS shown in **Fig. 2(b)**. It is known that the insulating PSS counterions enable the conducting PEDOT chains to exist as a stable aqueous suspension through Coulomb interaction. The addition of IPA into the PEDOT:PSS aqueous solution readily weakens the Coulomb interaction between the positively charged PEDOT and negatively charged PSS components by the screening effect, resulting in a conformational transition into an extended-coil structure of PEDOT.²⁶ Subsequently, the addition of C-dots would allow the extended PEDOT chains to interact with the C-dots because of the presence of abundant negatively charged functional groups on the C-dots surface. During gelation, the PEDOT chains preferentially interacting with the C-dots were stacked on the C-dots surface owing to the electrostatic interaction as well as π - π stacking,¹³ leading to the formation of CSNSs. The addition of C-dots affected the surface morphology of the PEDOT:PSS film as well as the interactions between the PEDOT chains in the polymer matrix. **Fig. 4** shows the nanoscopic morphology of the PEDOT:PSS film with C-dots obtained by atomic force microscopy (AFM). The phase image of the pristine PEDOT:PSS demonstrated phase separation between them where each domain had a disconnected and isolated nanostructure (**Fig. 4(a)**) with the bright

and dark regions in the phase image of PEDOT:PSS representing the PEDOT-rich and PSS-rich domains, respectively.¹¹ In contrast, **Fig. 4(b)** and (c), which are images from samples containing the C-dots, show relatively homogenous and interconnected PEDOT-rich domains. This morphological transition of the PEDOT-rich domain implies that the C-dots not only act as physical linkers within the organogels, but also hold the PEDOT-rich domains by the aggregation of CSNSs.

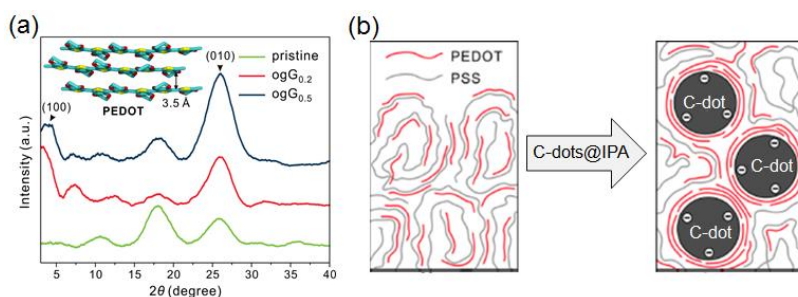


Fig. 3. (a) X-ray diffraction (XRD) patterns of the PEDOT:PSS organogel films obtained with volume fractions of C-dots solution. The inset shows the molecular structure of crystalline PEDOT chains with the (010) lattice spacing. (b) The schematic representation of the formation of the C-dots@PEDOT CSNS

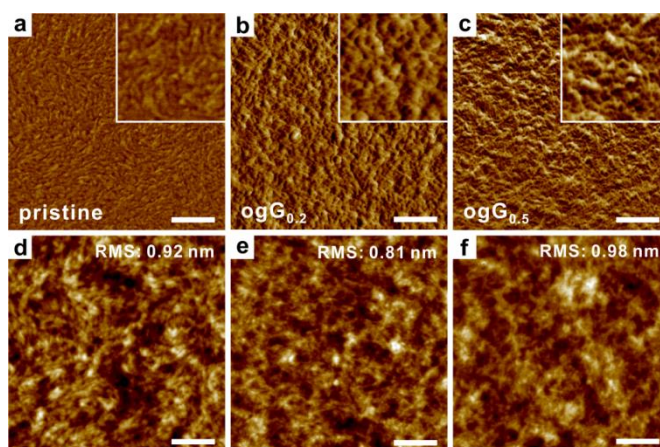


Fig. 4. Phase and topographic images of PEDOT:PSS organogel films of (a, d) pristine PEDOT:PSS, (b, e) ogC-dots_{0.2}, and (c, f) ogC-dots_{0.5} samples. All scale bars are 200 nm.

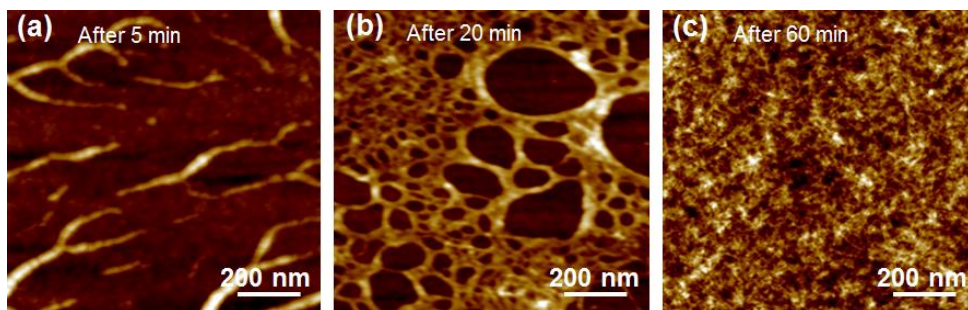


Fig. 5. The sequential change of AFM topographic images obtained during the formation of the PEDOT:PSS organogel film depending on the gelation (a) 5 min, (b) 20 min, and (c) 60 min after the addition of 20 vol% of C-dots solution.

The topological images of the organogels also reveal a more interconnected and reticulated structure. The formation of the reticulated structure was observed by a time-dependent AFM study during the gelation, as shown in *Fig. 5*. Interestingly, the incorporation of C-dots did not significantly affect the surface roughness of PEDOT:PSS film in contrast with the incorporation of GO sheets,²¹ owing to the small-sized C-dots. In addition, the organogel films also showed a high transparency, similar to the PEDOT:PSS/GO composite.¹⁹ The reorientation of PEDOT chains with phase separation is advantageous in enhancing the conductivity of PEDOT:PSS because of the lowered energy barrier required for charge hopping across the domains and chains.¹¹ Since the PEDOT chains in the organogel prefer to interact with each other in the CSNS and the PEDOT-rich domains show a three-dimensionally interconnected structure in the PEDOT:PSS matrix simultaneously, the charge hopping pathway is improved, leading to enhanced conductivity of the organogel.

The organogel films were used as the HEL in P3HT/PCBM bulk heterojunction OPVs fabricated by solution-processing (*Fig. 6(a)*). The characteristic parameters, such as the open-circuit voltage (V_{OC}), short-circuit current (J_{SC}), fill factor (FF),

and power conversion efficiency (PCE), are summarized in Table 1. Since the work function of the C-dots film was 5.0 eV (as obtained by ultraviolet photoelectron spectroscopy), the energy barrier to hole injection between the anode and the HEL was insignificantly affected by the C-dots incorporation. Minor differences were also identified in V_{OC} among the OPVs, indicating that the ohmic contact of the anode/active layer was maintained in the presence of C-dots. These results suggest that including C-dots in the HEL preserves the interfaces of the OPV system without disruption. Indeed, using ogC-dot_{0.2} as the HEL leads to an increase in the PCE by 26% compared to the PCE of the OPV with pristine PEDOT:PSS as the HEL. This significant enhancement in PCE is mainly attributed to the increase in J_{SC} , resulting from the enhanced conductivity and lowered series resistance of the organogel, as shown in **Fig. 6(b)**. The organogels showed more than four times higher conductivity in comparison to the pristine PEDOT:PSS whose conductivity was just about 1 S/cm. It can support the fact that the CSNSs provide a better pathway for the charge hopping with three-dimensionally interconnected structure of the HEL. However, the enhanced charge hopping pathway in the HELs with the C-dots shows a negative effect on FF. In general, the decrease in FF is related to the increase in series resistance or the decrease in shunt resistance of OPV.²⁷ The shunt resistance is also reduced with the incorporation of the C-dots, resulting in a leakage current between the electrodes. In contrast, the OPV with ogC-dots_{0.5} as the HEL showed a decrease in both J_{SC} and FF, and a small increase in device efficiency. The increased series resistance of ogC-dots_{0.5} in comparison to that of ogC-dots_{0.2} implies that excess C-dots disrupt charge transport within the HEL because of the aggregation of CSNSs and the higher population of the insulating C-dots. Thus, ogC-dots_{0.2} is considered as the optimum HEL to yield OPVs with the best performance.

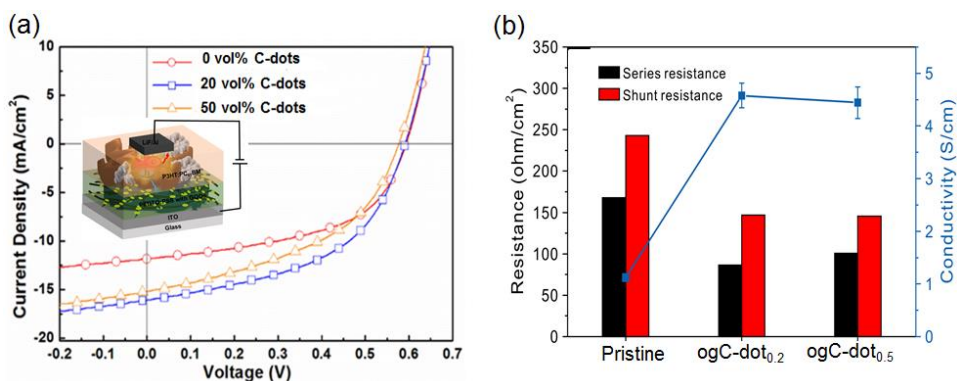


Figure 6. (a) Current density-voltage (J-V) characteristics of the OPV with the pristine PEDOT:PSS, ogC-dot_{0.2}, and ogC-dot_{0.5} as the hole extraction layer (HEL). (b) Series and shunt resistances of OPVs and the conductivity of the pristine PEDOT:PSS, ogC-dot_{0.2}, and ogC-dot_{0.5} films.

Table 1. Photovoltaic Performance of OPVs with various HELs^a

Devices	V_{oc} (V)	J_{sc} (mAcm ⁻²)	FF (%)	PCE (%)	Δ PCE (%)
pristine	0.58	11.97	54	3.77	-
ogC-dot _{0.2}	0.59	16.08	50	4.74	126
ogC-dot _{0.5}	0.58	14.59	48	4.08	108

^a The device structure in all cases is ITO/HEL/P3HT:PC₆₁BM/LiF/Al.

4 Conclusion

In conclusion, we have successfully demonstrated a simple process to fabricate a PEDOT:PSS-based organogel containing C-dots for efficient charge transport in a HEL of OPVs. The organogel film consisted of PEDOT-rich domains

in the matrix, formed by stacking PEDOT chains on the surface of C-dots, leading to CSNSs. These structures were formed because of the electrostatic interactions between the components. Furthermore, during gelation, three-dimensionally interconnected structures were also formed in the organogel film through the aggregation of the C-dot@PEDOT CSNSs, which improved the charge transport pathway. The use of organogel films with these distinct conformations and morphologies of the PEDOT-rich domains improved the OPV performance by up to 26% (in comparison to that of the OPV containing the pristine PEDOT:PSS as HEL). These results suggest that incorporation of C-dots in the organogel is compatible with the solution processing of OPV devices and is a promising strategy for enhancing the electrical properties of PEDOT:PSS, leading to the performance enhancement in flexible devices such as OPVs and polymer-based light emitting diodes.

5 References and Notes

- 1). Z. Liu, J. Li and F. Yan, *Adv. Mater.* **2013**, *25*, 4296.
- 2). J. You, L. Dou, K. Yoshimura, T. Kato, K. Ohya, T. Moriarty, K. Emery, C.-C. Chen, J. Gao and G. Li, *Nat. Commun.* **2013**, *4*, 1446.
- 3). A. Facchetti, *Chem. Mater.* **2011**, *23*, 733.
- 4). S. Günes, H. Neugebauer and N. S. Sariciftci, *Chem. Rev.* **2007**, *107*, 1324.
- 5). S. Guo, M. A. Ruderer, M. Rawolle, V. Körstgens, C. Birkenstock, J. Perlich and P. Müller-Buschbaum, *ACS Appl. Mater. Interfaces* **2013**, *5*, 8581.
- 6). H. Park, R. M. Howden, M. C. Barr, V. Bulović, K. Gleason and J. Kong, *ACS Nano* **2012**, *6*, 6370.

- 7). C. Gong, H. B. Yang, Q. L. Song, Z. S. Lu and C. M. Li, *Sol. Energy Mater. Sol. Cells* **2012**, *100*, 115.
- 8). J. Ouyang, C. W. Chu, F. C. Chen, Q. Xu and Y. Yang, *Adv. Funct. Mater.* **2005**, *15*, 203.
- 9). J. S. Yang, S. H. Oh, D. L. Kim, S. J. Kim and H. J. Kim, *ACS Appl. Mater. Interfaces* **2012**, *4*, 5394.
- 10). Y. Xia and J. Ouyang, *J. Mater. Chem.* **2011**, *21*, 4927.
- 11). D. A. Mengistie, M. A. Ibrahim, P. C. Wang and C. W. Chu, *ACS Appl. Mater. Interfaces* **2014**, *6*, 2292.
- 12). N. Kim, S. Kee, S. H. Lee, B. H. Lee, Y. H. Kahng, Y. R. Jo, B. J. Kim and K. Lee, *Adv. Mater.* **2014**, *26*, 2268.
- 13). J. Zhou and G. Lubineau, *ACS Appl. Mater. Interfaces* **2013**, *5*, 6189.
- 14). J. S. Yeo, J. M. Yun, D. Y. Kim, S. Park, S. S. Kim, M. H. Yoon, T. W. Kim and S. I. Na, *ACS Appl. Mater. Interfaces* **2012**, *4*, 2551.
- 15). J. Zhou, D. H. Anjum, L. Chen, X. Xu, I. A. Ventura, L. Jiang and G. Lubineau, *J. Mater. Chem. C* **2014**, *2*, 9903.
- 16). Y. Xia, K. Sun and J. Ouyang, *Energy Environ. Sci.* **2012**, *5*, 5325.
- 17). W. Zhang, B. Zhao, Z. He, X. Zhao, H. Wang, S. Yang, H. Wu, and Y. Cao, *Energy Environ. Sci.* **2013**, *6*, 1956.
- 18). J. Y. Oh, M. Shin, J. B. Lee, J. H. Ahn, H. K. Baik and U. Jeong, *ACS Appl. Mater. Interfaces* **2014**, *6*, 6954.
- 19). V. C. Tung, J. Kim, L. J. Cote and J. Huang, *J. Am. Chem. Soc.* **2011**, *133*, 9262.
- 20). H. S. Dehsari, E. K. Shalamzari, J. N. Gavgani, F. A. Taromi and S. Ghanbary, *RSC Adv.* **2014**, *4*, 55067.

- 21). J. C. Yu, J. I. Jang, B. R. Lee, G. W. Lee, J. T. Han and M. H. Song, *ACS Appl. Mater. Interfaces* **2014**, *6*, 2067.
- 22). E. Lee, J. Ryu and J. Jang, *Chem. Commun.* **2013**, *49*, 9995.
- 23). U. Lang, E. Muller, N. Naujoks and J. Dual, *Adv. Funct. Mater.* **2009**, *19*, 1215.
- 24). J. Zhou, E. Q. Li, R. Li, X. Xu, I. A. Ventura, A. Moussawi, D. H. Anjum, M. N. Hedhili, D.-M. Smilgies and G. Lubineau, *J. Mater. Chem. C* **2015**, *3*, 2528.
- 25). N. Kim, B. H. Lee, D. Choi, G. Kim, H. Kim, J. R. Kim, J. Lee, Y. H. Kahng and K. Lee, *Phys. Rev. Lett.* **2012**, *109*, 1.
- 26). D. Alemu, H.-Y. Wei, K.-C. Ho and C.-W. Chu, *Energy Environ. Sci.* **2012**, *5*, 9662.
- 27). Z. Hu, J. Zhang and Y. Zhu, *Renewable Energy* **2014**, *62*, 100.

Section 5. Quantum Dots-Silica Composite as an Efficient Spectral Converter in a Luminescent Down-Shifting Layer of Organic Photovoltaic Devices

Abstract

We developed gradient quantum dot (QD)@polyvinylpyrrolidone (PVP)-silica composite as a spectral converter to improve light harvesting of the photoactive layer in organic photovoltaic (OPV) devices. The spectral converter prepared by a simple sol-gel method served as a luminescent down-shifting (LDS) layer that absorbed ultraviolet and emitted visible light. Re-emitted light energy from the LDS layer appeared within the absorption range of P3HT as the photoactive donor material in OPV devices. We investigated how the light harvesting ability was affected by the concentration of QD@PVP and the thickness of the LDS layer. Consequently, the OPV devices with the LDS layer showed increased power conversion efficiency (PCE) from 3.38% to 3.68% compared to pristine OPV devices due to improved incident light transmittance and increased light harvesting.

Keywords: Luminescent down-shifting, spectral converter, light harvesting, bulk heterojunction, organic photovoltaic

1 Introduction

Organic photovoltaic (OPV) solar cells have received much attention as a renewable energy source due to the advantage of flexibility, easy synthesis of active layer materials, and low-cost fabrication of large areas.¹⁻³ Intensive researches have been conducted, reaching a power conversion efficiency (PCE) of 13 %.¹ However, there are still challenges to improving efficiency and lifetime of OPV devices, compared to inorganic solar cells.^{4,5} Ultraviolet (UV) light has been known to weakly contribute to photon-to-current conversion and degrade organic photoactive materials such as polymers and small molecules, and thus would reduce lifetime as well as PCE of OPV devices.^{6,7} It was known that these problems could be solved by using spectral converters.⁸⁻¹⁰ The ideal photo-conversion materials (spectral converters) should absorb UV photon energy in a wide range and efficiently transfer absorbed energy to the photoactive materials in OPVs. To meet these requirements, colloidal quantum dots (QDs) are considered the most promising as practical spectral converters.¹¹⁻¹³ QDs can be used in two ways to be applied to OPVs. One method is incorporation of QDs into the active layer or carrier transport layer of OPVs for exciton (electron-hole pair) generation or charge transport.¹¹ There is another method utilizing QDs as a luminescent down-shifting (LDS) material, embedded within the host matrix.¹²

The host matrix should be transparent over a broad range of wavelengths, and should ensure durability during the fabrication processes and should be completely miscible with guest QDs with no aggregation. Polymeric host materials provide good optical and thermal properties as well as easy processing.^{14,15} However, the surface of QDs is hydrophobic and unstable toward radical species, generated during free radical polymerization processes in the presence of QDs. Simple

mixing of poly(methyl methacrylate) (PMMA) polymers with QDs induces phase separation, owing to low compatibility of PMMA with organic-coated QDs.^{16,17} Several research groups have been striving to overcome these problems involved in QDs-polymer composites.^{18,19} Alternatively, the silica sol-gel process, including hydrolysis and condensation, has been considered a promising approach for the host matrix due to the transparency in the UV-Vis region and the stability of thin film during OPV fabrication process.^{14,20} However, acid-catalysed hydrolysis process of silicate is incompatible with hydrophobic QDs because the surface of QDs can be attacked by proton (H^+) in acidic aqueous solution.¹⁷ This phenomena would lead to low quantum yields by energy transfer between its aggregates.²¹ In addition, CdSe core and core@shell quantum dots are unstable under long-term irradiation.²²⁻²⁴ Thus, it is necessary to overcome those problems mentioned above for more desirable LDS materials.

Herein, we describe the development of gradient QDs@ polyvinylpyrrolidone (PVP)-silica composite and its LDS effect in OPVs. As a spectral converter, gradient QDs have several merits, including high absorption coefficient in the UV range, and narrow emission spectrum (full width at half maximum, FWHM ~ 30 nm). In particular, gradient QDs have better quantum yields and (photo)chemical stability than core@shell QDs.²⁴⁻²⁶ Host materials were prepared by just mixing tetraethyl orthosilicate (TEOS) and methyltrimethoxysilane (MTMS) in water which can be hydrolysable even without any catalyst. The resulting organosilica matrix is ideal as the host matrix of a LDS layer due to the transparency in the UV-Vis region and no negative effect on photoluminescence (PL) of QDs. Hydrophobic QDs were wrapped with an amphiphilic polymer, polyvinylpyrrolidone (PVP), to make them soluble in chloroform. The QDs-silica composite can be applied as a LDS layer in OPVs using a typical blend of poly(3-

hexylthiophene) (P3HT):[6,6]-phenyl-C₆₁-butyric acid methyl ester (PCBM) as active materials of bulk heterojunction (BHJ) OPVs. The 8.9 % improvement of PCE in the OPV performance is attributed to enhancement in the light harvesting of a QDs-silica thin film as a LDS layer.

2 Experimental Methods

2.1 Synthetic Procedure

Preparing the Mixed chalcogenide stock solutions

Both selenium (0.03158 g, 0.4 mmol) and sulfur (0.1282 g, 4.0 mmol) were weighed into a vial in the glove box and 3 ml of tri-n-octylphosphine (2.19 g, 6.72 mmol) was added for the synthesis of the green-emitting gradient alloy QDs. The mixture was stirred overnight until all the solids were dissolved and the mixture solution became clear and colorless. This solution was stored at room temperature in the glove box until being used.

Synthesis of the green-emitting gradient alloy QDs

For the synthesis of the green-emitting gradient alloy QDs ($\lambda_{em} = 550$ nm), cadmium acetate (CdO) dehydrate (0.4 mmol) and zinc acetate (Zn(OAc)₂) (4.0 mmol), oleic acid (OA) (5.5 ml, 17.6 mmol), and 1-octadecene (ODE) (10 ml) were mixed. The mixture was heated to 180 °C until all the solids in the flask were dissolved clearly to generate metal precursors of Cd-OA and Zn-OA. These were degassed at 150 °C under vacuum for 20 min to remove the produced water. The mixture was heated to 300 °C, and the chalcogenide precursor solution containing Se (0.4 mmol) and S (4.0 mmol) was injected. The mixed metal and chalcogenide

solution was heated at 280 °C for 10 min. After the reaction, solution was cooled down to 25 °C and centrifuged at 4000 rpm with acetone. Purified QDs 0.1 g and PVP 1 g were stirred in chloroform 100 ml for 24 h. We dissolved QD@PVP in chloroform for OPV process. We dissolved QD@PVP (abbreviated as QDs) in ethanol to test acid endurance.

2.2 Preparation of QDs-Silica Thin Films for a Luminescent Down-Shifting Layer

The solution for the luminescent down-shifting layer was prepared as follows. The precursor solution for sol-gel process was made to be 1:1.5:4.3 molar ratio of TEOS:MTMS:H₂O. The solution was stirred for 72 hr at room temperature. The synthesized QDs in chloroform were mixed in 1:1 volume ratio with the precursor solution for sol-gel process. The weight of the QDs varied from 0 to 0.5 wt% (5 mg QDs/1 ml solution). The ITO/glass substrates were sequentially cleaned using detergent (Gmbh, Muscasol, 10 min), deionized water (10 min), isopropyl alcohol (IPA) (10 min) with ultrasonication, followed by annealing at 120 °C for 3 hr. The substrates underwent an ozone treatment for 5 min. LDS layers was fabricated by spin-casting process on the opposite side of the ITO/glass substrate. An ITO/glass substrate without an LDS layer was also prepared for the control device. All the samples of the as-prepared LDS layer were annealed at 120 °C, 30 min for thermal curing.

2.3 Fabrication of Organic Photovoltaic Devices

PEDOT:PSS (CLEVIOS P) aqueous solution was spin-coated onto pre-patterned ITO/glass with or without a luminescent down-shifting layer substrate to

prepared the hole transport layer (HTL) and then carried out post-annealing treatment at 120 °C, 20 min in glove box into nitrogen gas. Then, 2.0 wt% of P3HT:PC₆₁BM (1:0.8 w/w) in chlorobenzene solvent for active layer of bulk heterojunction type was spin-coated on PEDOT:PSS as a hole transport layer (50 nm) at 2000 rpm, 30s and then annealed at 150 °C, 10 min in an nitrogen atmosphere glove box. The active layer thickness is 100 nm measured by profilometry. Finally LiF (1 nm) and Al (100 nm) were thermally evaporated under 10⁻⁶ torr as a cathode electrode.

2.4 Instruments

High resolution transmission electron microscope (HRTEM, JEOL JEM-2100) was performed at 200 kV for acquisition of the as-synthesized QDs. Scanning electron microscope was used (SEM, Hitachi S-4300) for confirming thin films thickness of the QDs-silica composite. The optical properties of all the prepared samples were characterized by absorption (UV-Vis) spectra and photoluminescence (PL) (Beckman DU650, Jasco FP-7500 spectrophotometer). The current-voltage characteristics of OPV devices were determined by using a Keithley 2400 source meter and an AM1.5 simulated white light source.

3 Results and Discussion

All The gradient QDs were synthesized utilizing the pyrolysis method with a minor modification .²⁷ The gradient QDs show high quantum efficiency and stability under ambient conditions compared to core@shell QDs in *Fig. 1(d)*. As prepared, the gradient QDs capped by oleic acid (OA) have an average diameter of ca. 6 nm

(see **Fig. 1(a)** for the transmission electron microscopy image of the sample). The alloy inside gradient QDs means chemical composition heterogeneities and strains, which affect XRD peak shifts and broadening in **Fig. 2(a)**.²⁸ Since dispersion of QDs in the LDS layer is a crucial factor for the application as a spectral converter,¹³ the hydrophobic OA-capped QDs were wrapped with an amphiphilic polymer, PVP (see **Fig. 1(b)**). The PVP-wrapping of gradient QDs (abbreviated as QDs, *vide infra*) were carried out by mixing OA-coated gradient QDs and PVP in chloroform, and stirring for 24 hr. The QDs showed no change in PL properties (intensity and emission wavelength), which indicates that QDs were not aggregated.^{19,29} This QDs show high endurance in acidic and basic conditions, allowing further chemical transformation in **Fig. 2(b)** and **(c)**.

For the application as a LDS layer, the QDs-silica composites were prepared as follows to confirm compatibility of QDs with the silica medium. The sol-gel precursor solution for the host matrix was prepared simply by blending tetraethyl orthosilicate (TEOS) and methyltrimethoxysilane (MTMS) in water (TEOS:MTMS:H₂O = 1:1.5:4.3 in molar ratio) and then stirring for 72 hr at room temperature without catalyst, which was added to the chloroform solution of QDs in ethanol (co-solvent of sol-gel process). The PL emission wavelength of the resulting composite films on a slide glass depends on the size and composition of QDs. The resulting silica matrix is ideal as the host matrix of a LDS layer due to the transparency in the UV-Vis region, and the QDs do not aggregate in the silica medium. The QDs-silica composites having green emission were deposited on the opposite side of the ITO/glass substrate by spin-casting, and then thermal curing at 120 °C for 30 min. The optical properties of QDs-silica (0.1 and 0.5 wt%) thin films were investigated by measuring absorption and PL spectra, compared to 0.005 wt% OA-coated QDs in ethanol.

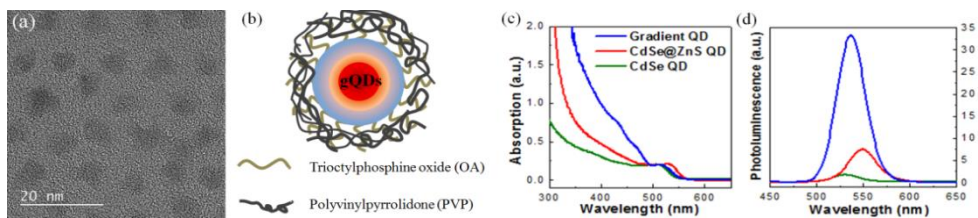


Fig. 1. TEM image of oleic acid (OA)-coated gradient QDs (insert image: SAED pattern), (b) schematic of QDs@PVP, and (c) absorption and (d) photoluminescence of CdSe (green), CdSe@ZnS (red), and gradient QDs (blue)

There are no noticeable differences in absorption and PL spectra between QDs-silica thin films and OA-coated QDs in *Fig. 3(a)*. This indicates that the QDs were well dispersed without both phase separation and aggregation in the thin film (silica matrix). Normalized PL spectra by excitation at 350 nm appeared between 520 and 620 nm and the maximum peak was at 562 nm with a FWHM of 40 nm in *Fig. 3(b)*. The emission spectrum of the thin film appeared within the absorption range (350 to 650 nm with λ_{\max} of 551 nm) of the poly(3-hexylthiophene) (P3HT) thin film as a photoactive material for OPVs, as shown in *Fig. 2*. Therefore, it is apparent that the QDs in thin film on the opposite side of a ITO/glass substrate can act as a spectral converter through converting a part of near UV light to green visible light so that the photo-response of the P3HT will be increased.^{9,10}

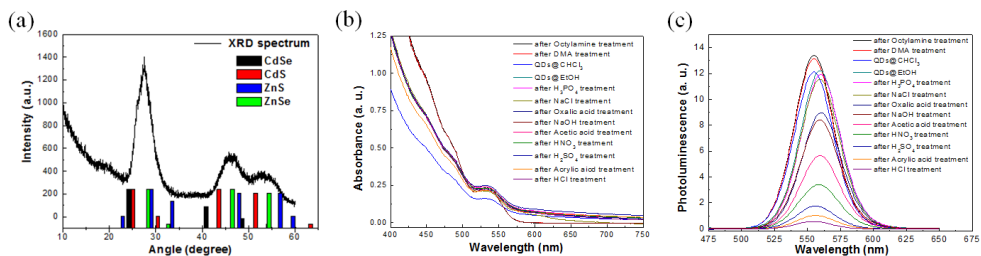


Fig. 2. XRD spectrum of OA-coated gradient QDs (black solid line) (inserted reference of bulk CdSe (black bar), CdS (red bar), ZnS (blue bar), and ZnSe (green bar)) and changes (b) absorption, and (b) photoluminescence intensity after acid or base treatment of QDs (we injected 1 ml acid or base solution into QDs and then measured optical properties after 1 h

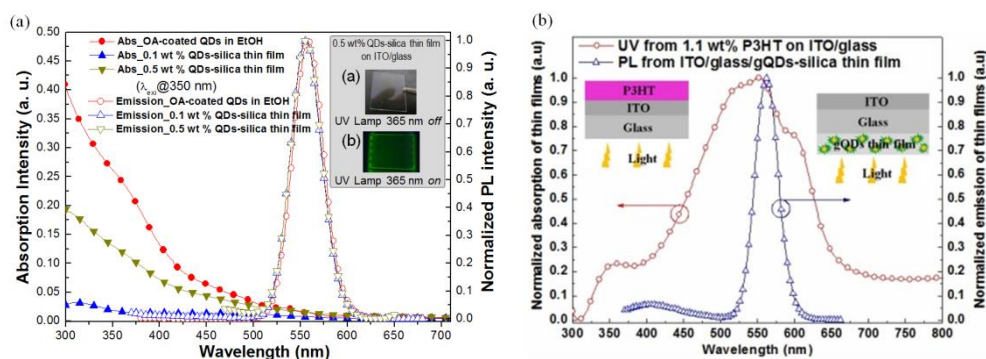


Fig. 3. (a) UV-visible absorption (filled symbols) and photoluminescent spectra (open symbol) of the ITO/glass/QDs-silica thin films and OA-coated QDs in EtOH (inserted image of QDs-silica thin film (a) without, and (b) with 365 nm UV irradiation), and (b) UV-visible absorption of the P3HT/ITO/glass thin film (circle) and photoluminescent spectra of the ITO/glass/QDs-silica thin film (triangle)

We also investigated the effect of the thin film thickness on the optical properties of the thin films of 0.1 wt% QDs-silica composites. The PL spectra show that the emission intensity increases with the thickness of the QDs-silica thin film. However, the transmittance was not affected by the thickness of the thin film in the visible range. This result clearly reveals that the QDs were well dispersed in the thin film.

We also examined the effect of the concentration of QDs (0 to 0.5 wt%) on the optical properties of QDs-silica thin film. The concentration of QDs in the silica matrix directly affected the light harvesting of P3HT.^{6,10} The thin films with different concentrations of QDs have uniform surfaces and similar thicknesses of ca. 3.1 μm , confirmed by scanning electron microscopy (SEM). The transmittance of QDs-silica thin films in the short-wavelength region is almost linearly diminished with the concentration of QDs as shown in **Fig. 4(a)**. This result implies that the photoactive layer in OPV can be protected against photo-degradation because of the efficient UV-absorbing QDs in the LDS layer.^{6,7}

However, in the wavelength range from 400 to 650 nm, the transmittance value of bare ITO/glass substrate is 82.1% and those of the thin films are 83.6, 83.0, 82.5, and 82.1 % with QDs loading of 0, 0.1, 0.3, and 0.5 wt% on ITO/glass substrate, respectively in **Fig. 4(b)**. These results imply that as the intensity of the incident sun light increases, the absorption of the photoactive materials is enhanced due to gradient refractive index from the thin film to ITO. The refractive index of the silica matrix ($n_D = 1.2$) is between those of air ($n_D = 1.0$) and glass substrate ($n_D = 1.5$).³⁰ The transmittance values of the thin films with 0 – 0.3 wt% QDs are higher than that of the only ITO/glass substrate in the absorption wavelength range of P3HT. We investigated the effect of QDs-silica thin films as a LDS layer on the OPV device performance (in terms of the light harvesting ability with various concentrations of QDs within the silica matrix). The thermal stability of QDs-silica thin films is important because the annealing processes are required after the spin casting of a LDS layer during the fabrication of the OPV devices. The QDs-silica thin films are stable enough during the fabrication of OPV devices because a thin film based on the MTMS:TEOS copolymer can be cured at 420 °C.³⁰ **Fig. 5(a)** shows a schematic of the bulk heterojunction (BHJ) OPV with the LDS layer. Four

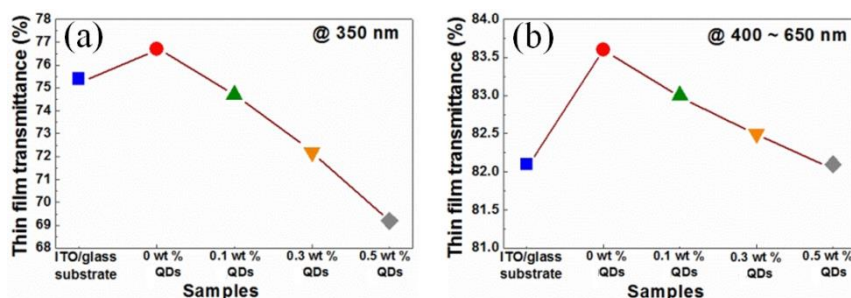


Fig. 4. (a) Transmittance values according to the QDs concentration in the thin films on the opposite side of the ITO/glass/QDs-silica thin films

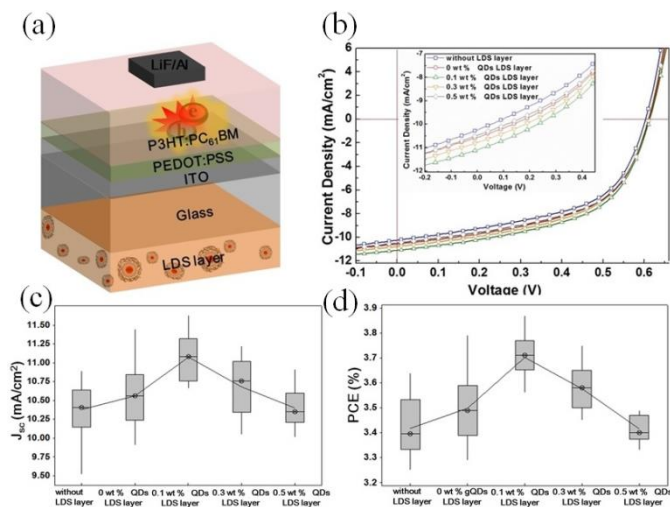


Fig. 5. (a) Schematic of the OPV device, (b) current density-voltage (J - V) curves, (c) J_{sc} and (d) PCE values with various concentration of QDs in thin films

BHJ devices were fabricated using PEDOT:PSS as a hole transport layer (HTL), P3HT:[6,6]-phenyl-C₆₁-butyric acid methyl ester (PCBM) (1:0.8, w/w) as an photoactive layer, and the QDs-silica (0, 0.1, 0.3, and 0.5 wt% of QDs) thin films as a LDS layer. A reference BHJ device was also fabricated without a LDS layer. The characteristic parameters of the OPV devices, including the open-circuit voltage (V_{oc}), short-circuit current (J_{sc}), fill factor (FF), and power conversion efficiency (PCE), are summarized in **Table 1**. The V_{oc} and FF values were similar in all the devices. As expected, the J - V curves of the devices with a LDS layer (**Fig. 5(b)**) exhibited higher values of J_{sc} and PCE than those of the reference device without a LDS layer. The J_{sc} value (11.17 mA/cm²) of the device with a 0.1 wt% QDs in the LDS layer is higher than that of the reference device (10.26 mA/cm²). This is because the QDs in the thin film is uniformly dispersed and their emission range is within the absorption range of P3HT, leading to more effective generation of excitons in P3HT.⁸⁻¹⁰ The maximum J_{sc} and PCE values were observed at 0.1 wt%

QDs in the LDS layer. The PCE and J_{sc} values gradually decrease with increasing amount of QDs (0.3 and 0.5 wt%) in the LDS layer. These results imply that increasing the amount of QDs in the LDS layer results in more effective light harvesting of the LDS layer (in the short wavelength region) but in less transmittance of the incident sun light (in the visible range). Thus, one should make a balance between two factors for improving efficiency of OPVs. It is, therefore, reasonable to infer that the QDs-silica thin film as a LDS layer enables light harvesting and protection of the photoactive layer from UV light.

Table 3 Photovoltaic performances of bulk heterojunction OPV devices according to the concentration of QDs in LDS layer

Devices	V_{oc} (V)	J_{sc} (mAcm ⁻²)	FF (%)	PCE (%)	Δ PCE (%)
w/o LDS layer	0.61	10.26	54	3.38	-
0 wt% QDs LDS layer	0.61	10.64	54	3.50	103.6
0.1 wt% QDs LDS layer	0.61	11.17	54	3.68	108.9
0.3 wt% QDs LDS layer	0.61	10.73	54	3.53	104.5
0.5 wt% QDs LDS layer	0.61	10.40	54	3.43	101.3

All devices are consisted with ITO/PEDOT:PSS/P3HT:PC₆₁BM (2 wt%, 1:0.8 w/w)/LiF/Al

4 Conclusion

In conclusion, we developed QDs-silica thin films as an efficient LDS layer of OPV devices where QDs and silica matrix were used as a spectral converter and a transparent host matrix, respectively. The QDs were dispersed effectively without both phase separation and aggregation in the silica matrix. The LDS layer enabled effective light harvesting in the short wavelength region and

thus reemitted visible light in the absorption range of P3HT, enabling increased light harvesting of the photoactive layer. It was found that the OPV fabricated with a 0.1 wt% QDs in the LDS layer results in 8.9% increase in the PCE. This approach is expected to be applied to other kinds of solar cells and light-emitting diodes.

5 References and Notes

- 1). W. Zhao, S. Li, H. Yao, S. Zhang, Y. Zhang, B. Yang and J. Hou, *J. Am. Chem. Soc.*, **2017**, *139*, 7148.
- 2). S. Berson, R. D. Bettignies, S. Bailly and S. Guillerez, *Adv. Funct. Mater.*, **2007**, *17*, 1377.
- 3). K. Feng, X. Xu, Z. Li, Y. Li, T. Yu and Q. Peng, *Chem. Commun.*, **2015**, *51*, 6290.
- 4). M. Jørgensen, K. Norman and F. C. Krebs, *Sol. Energy. Mater. Sol.*, **2008**, *92*, 686.
- 5). V. Sivakov, G. Andrä, A. Gawlik, A. Berger, J. Plentz, F. Falk and S. H. Christiansen, *Nano Lett.*, **2009**, *9*, 1549.
- 6). P. G. Parejo, M. Zay and D. Levy, *J. Mater. Chem.*, **2006**, *16*, 2165.
- 7). W. Xu, H. Song, D. Yan, H. Zhu, Y. Wang, S. Xu, X. Bai, B. Dong and Y. Liu, *J. Mater. Chem.*, **2011**, *21*, 12331.
- 8). M. J. Currie, J. K. Mapel, T. D. Heidel, S. Goffri and M. A. Baldo, *Science*, **2008**, *321*, 226.

- 9). J. J. Huang, Z. F. Zhong, M. Z. Rong, X. Zhou, X. D. Chen and M. Q. Zhang, *Carbon*, **2014**, *70*, 190.
- 10). T.-H. Wang, T.-W. Huang, Y.-C. Tsai, Y.-W. Chang and C.-S. Liao, *Chem. Commun.*, **2015**, *51*, 7253.
- 11). P. V. Kamat, *J. Phys. Chem. C*, **2008**, *112*, 18737.
- 12). F. P-Milton and Y. K. Gun'ko, *J. Mater. Chem.*, **2012**, *22*, 16687.
- 13). F. Meinardi, A. Colombo, K. A. Velizhanin, R. Simonutti, M. Lorenzon, L. Beverina, R. Viswanatha, V. I. Klimov and S. Brovelli, *Nature Photon.*, **2014**, *8*, 392.
- 14). S. M. Reda, *Acta Materialia*, **2008**, *56*, 259.
- 15). Y. Ma, B. Zhang, M. Gu, S. Huang, X. Liu, B. Liu and C. Ni, *J. Appl. Polym. Sci.*, **2013**, *130*, 1548.
- 16). H. Zhang, C. Wang, M. Li, X. Ji, J. Zhang and B. Yang, *Chem. Mater.*, **2005**, *17*, 4783.
- 17). H. Kim, B. H. Kwon, M. Suh, D. S. Kang, Y. Kim and D. Y. Jeon, *Electrochem. Solid-State Lett.*, **2011**, *14*, K55.
- 18). C. Graf, Dirk L. J. Vossen, A. Imhof and A. van Blaaderen, *Langmuir*, **2003**, *19*, 6693.
- 19). T. Pellegrino, L. Manna, S. Kudera, L. Tim, K. Dmitry, A. L. Rogach, S. Keller, J. Rädler, G. Natile and W. J. Parak, *Nano Lett.*, **2004**, *4*, 703.
- 20). Z. Ning, O. Voznyy, J. Pan, S. Hoogland, V. Adinolfi, J. Xu, M. Li, A. R. Kirmani, J.-P. Sun, J. Minor, K. W. Kemp, H. Dong, L. Rollny, A. Labelle, G. Carey, B. Sutherland, I. Hill, A. Amassian, H. Liu, J. Tang, O. M. Bakr and E. H. Sargent, *Nature Mater.*, **2014**, *13*, 822.

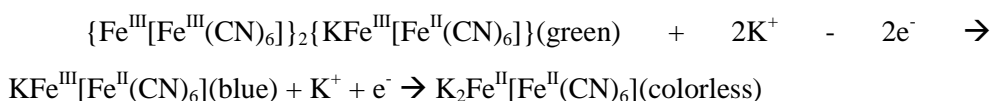
- 21). S. H. Jeong, J. S. Lee, J. T. Nam, K. H. Im, J. H. Hur, J.-J. Park, J.-M. Kim, B. H. Chon, T. H. Joo and S. J. Kim, *J. Phys. Chem. C*, **2010**, *114*, 14362.
- 22). J. Cho, Y. K. Jung, J.-K. Lee and H.-S. Jung, *Langmuir*, **2017**, *33*, 3711.
- 23). J. J. Li, A. Wang, W. Guo, J. C. Keay, T. D. Mishima, M. B. Johnson and X. Peng, *J. Am. Chem. Soc.*, **2003**, *125*, 12567.
- 24). R. E. Bailey and S. Nie, *J. Am. Chem. Soc.*, **2003**, *125*, 7100.
- 25). Y. Fu, D. Kim, W. Jiang, W. Yin, T. K. Zhn and H. Chae, *RSC. Adv.*, **2017**, *7*, 40866.
- 26). J. Lim, W. K. Bae, D. Lee, M. K. Nam, J. Jung, C. Lee, K. Char and S. Lee, *Chem. Mater.*, **2011**, *23*, 4459.
- 27). J. S. Cho, Y. K. Jung and J.-K. Lee, *J. Mater. Chem.*, **2012**, *22*, 10827.
- 28). Y. Golan, G. Hodes and I. Rubinstein, *J. Phys. Chem.*, **1996**, *100*, 2220
- 29). J. M. Cha, Y. Cui and J.-K. Lee, *J. Mater. Chem.*, **2010**, *20*, 5533.
- 30). S. Kim, J. Cho and K. Char, *Langmuir*, **2007**, *23*, 6737.

**Part III. Studies on Carbon Dots as an Ion Conductor
on Energy Harvesting of Electrochromic Devices**

1. Introduction

1.1. General Introduction

Since the electrochemical coloration was observed of bulk tungsten oxide in 1930 year by Kobosew,¹ electrochromic devices (ECDs) have been developed for the various fields such as electrochemical sensor, EC display, EC smart window, and EC automobile mirror.²⁻⁵ Electrochromism is defined as a reversible color change of a material caused by a electrochemical oxidation-reduction (redox) reaction with electrode.⁵ The switching multiple colors of electrochromic (EC) materials are given terms polyelectrochromism. The color change of EC materials is achieved by controlling the bandgap (E_g) through changes in the composition and structure of the molecules. Since the early 2000 year, both new electrochromic (EC) materials and ECD have been development by the increasing research efforts.⁶⁻⁹ The main electrochromic materials are: 1). Transition metal oxides¹⁰, 2). Organic small molecules¹¹, and 3). Conducting polymers¹². The transition metal oxide such as tungsten trioxide (WO_3)⁶, Prussian blue (PB)¹³, and Metal oxides (NiO, TiO_2 , MoO_3)^{14,15} can formed to thin film by various methods like electrochemical deposition,¹⁶ sol-gel process,¹⁷ chemical vapor deposition,¹⁸ and spray deposition.¹⁹ Prussian blue (iron(III) hexacyanoferrate(II), $Fe^{3+}-(CN)_6-Fe^{2+}$), discovered by Diesbach in 1704s, can change reversible color between green, blue, and colorless (bleached) by the intercalation/de-intercalation of mobile potassium (K^+) ions.²⁰



Tungsten trioxide is colorless in oxidation state and blue color in reduction state as a function of the concentration of Li mobile ions. The color change process is caused by electron exchange between W^{5+} and W^{6+} ions.



In case of organic molecules, such as viologen derivatives and conducting polymer, organic material has advantages with various molecular structures, low cost and easy processing. The change color of viologen is related to the first redox state, owing to optical charge transfer between the oxidized state (+1) and reduced state (zero valent nitrogens).²¹

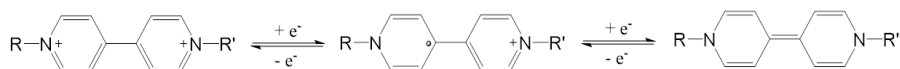


Fig. 1.1. The three redox state of viologen

The color of conducting polymers, such as polypyrrole, polythiophene and polyaniline, depends on the degree of doping into polymer structure. Hence, a large number of colors are available with the polymeric materials.^{22,23}

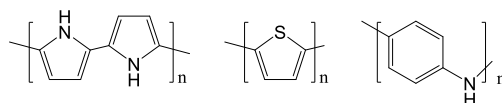


Fig. 1.2. The conducting polymer structure

The ECDs are divided into two types such as solid and solution type, depending on the nature of the EC layer and the electrolyte.^{24,25} The solid-state ECDs have multilayer structure, involving insoluble thin films. The ionic charge transport is a key play to rate-limiting process for the redox reaction of EC layer due to the low ionic conductivity of the electrolyte. The other hand, the solution-state ECDs use a solution electrolyte with the dissolved EC material. The EC materials are diffused into the bulk of the solution and undergo a homogeneous

electron transfer through collision of them, resulting in color changing. The solution-state ECDs have several disadvantages, compared to solid. A long time and high power consumption are required for changing the color.

1.2. Working Principle of ECDs

Electrochromic devices (ECDs), which are a type of electrochemical cell, consist of electrical conducting electrode, electrochromic layer, and ion storage layer.²⁶ As shown *Fig. 1.3*, the electrochromic (EC) layer, changing its color through the redox reaction, is on a transparent conducting electrode (TCO) such as indium tin oxide (ITO). An ion storage layer on the opposite electrode such as counter electrode causes the counter electrochemical reaction. The electrodes are separated by an ion conducting layer such as electrolyte. Therefore, the ECD is electrically short-circuited and current is generated by the migration of ions, depending on the direction of the applied voltage. A typical electrochromic materials are Prussian blue (PB), poly(3,4-ethylenedioxythiophene) (PEDOT), polyaniline (PANI), viologene derivatives, and Phthalocyanine. The electroactive species comprise different numbers of electrons before and after the redox process, so different spectroscopic transitions are exhibited with these redox states. Hence the materials need energies between oxidized and reduced state through the electron transfer reaction with electrode. The EC layer should have the following characteristics; high-coloration efficiency, fast redox process, and good electrochemical stability. The color switching of EC layer in ECD is changed by the applied electrical voltage or current. It means that any charge is flowed external circuit along with the charge-compensating ions which are intercalation or de-intercalation for electroneutrality of the EC material, similar to secondary ion

battery. Therefore two redox couples must be involved in TCO and counter electrode, one species being oxidized while the other one is reduced. Although electrical field in ECD is removed, including movement of any charge and ion, the color state of EC layer is sustained for their memory effect under open-circuit conditions. The ECD characteristics are determined by the figure of merit: coloration efficiency (η), contrast ratio (CR), optical density (OD), switching time, and cycling life. The CR is defined as the transmittance change in coloring and bleaching state in the case of transmissive device type and given;

$$CR(\Delta T) = T_b - T_c$$

where T_c , T_b are transmittance of the coloring state and of the bleaching state, respectively. The ΔT depends on ionic conductivity and the thickness of EC layer. OD is expressed optical transmittance at a given wavelength as $\log_{10}(1/T)$. The η (cm^2/C) is defined as the change in the ΔOD to injected or ejected charge density (Q) and is represented:

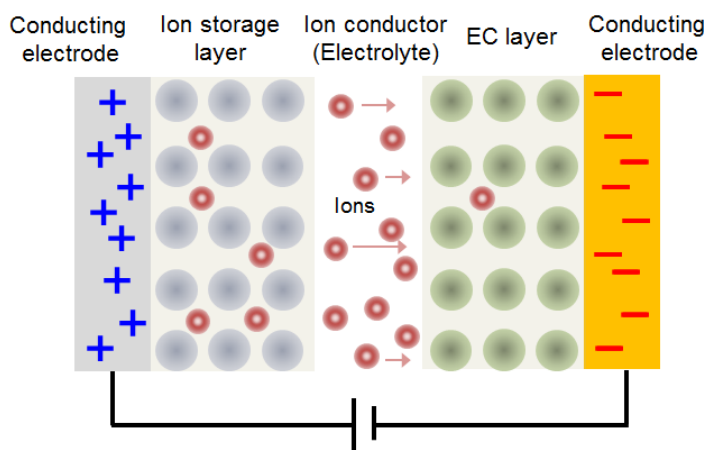


Fig. 1.3. Schematic side view of electrochromic device structure

$$\eta(\lambda) = \frac{\Delta OD}{\Delta Q} = \frac{\log\left(\frac{T_b}{T_c}\right)}{\Delta Q}$$

The switching time is the time required to change from its coloring state to its bleaching state. There are involved with ionic conductivity of the electrolyte, morphology of the EC layer, and device structure. The cycle life represents the number of the color switching cycles without any significant extent of the decreasing performance. The reasons for the low cycle life are related to the degradation of TCO, EC layer, and electrolyte. The degradation of materials is occurred by the complex elements. Thus, the cycle life depends on the stability of the constituent materials when charging/discharging for the changing color of the EC material. For example, as the color switching is repeated, many electrochemical issues, such as heat release from the resistance or detrimental side reaction from the applied electric field, can result in the loss of the ECDs performance.

2. References and Notes

- 1). N. Kobosew and N. I. Nekrassow, *Zeitschrift fur elektrochemie und angewandte physikalische. Chemie.*, **1930**, 36, 529.
- 2). A. Balan, D. Baran and L. Toppare, *Polym. Chem.* **2011** , 2, 1029 .
- 3). R. J. Mortimer, *Annu. Rev. Mater. Res.* **2011** , 41, 241 .
- 4). C. M. Amb, A. L. Dyer and J. R. Reynolds , *Chem. Mater.* **2011** , 23, 397 .
- 5). J. R. Platt, *J. Chem. Phys.* **1961** , 34, 862 .
- 6). J. Wang , E. Khoo, P. S. Lee and J. Ma , *J. Phys. Chem. C* **2008** , 112, 14306.
- 7). G. E. Gunbas, A. Durmus and L. Toppare , *Adv. Funct. Mater.* **2008** , 18, 2026 .

- 8). S. Xiong, P. Jia, K. Y. Myab, J. Ma, F. Boey and X. Lu, *Electrochim. Acta* **2008**, *53*, 3523 .
- 9). S. Bhandari , M. Deepa , A. K. Srivastava , A. G. Joshi , R. Kant , *Phys. Chem. B* **2009** , *113*, 9416 .
- 10). D.N. Buckley and L.D. Burke, *J. Chem Soc. Faraday*, **1975**, *72*, 1447.
- 11). M.M. Nicholson, Electrochromism and display devices, in: C.C. Leznoff, A.B.P. Lever (Eds.), *Phthalocyanines: Properties and Applications*, Vol. 3, VCH, Weinheim.
- 12). H. Meng, D. Tucker, S. Chaffins, Y. Chen, R. Helgeson, B. Dunn, and F. Wudl, *Adv. Mater.*, **2003**, *15*, 146.
- 13). M.B. Robin, *Inorg. Chem.* **1962**, *1*, 337.
- 14). S.-Y. Lin, Y.-C. Chen, C.-M. Wang, C.-Y. Wen and T.-Y. Shin, *Solid State Ionics*, **2012**, *212*, 81.
- 15). D. D. Yao, R. A. Rani, A. P. O'Mullane, K. Kalantar-zadeh and J. Z. Ou, *J. Phys. Chem. C*, **2014**, *118*, 10867.
- 16). L.D. Burke and O.J. Murphy, *J. Electroanal. Chem.*, **1980**, *112*, 379.
- 17). P.M.S. Monk, R.J. Mortimer and D.R. Rosseinsky, *Electrochromism: Fundamentals and Applications*, VCH, Weinheim, 1995.
- 18). T. Maruyama and S. Arai, *J. Electrochem. Soc.*, **1996**, *143*, 1383.
- 19). P.S. Patil, L.D. Kadam and C.D. Lokhande, *Solar Ener. Mater. Solar Cells*, **1998**, *53*, 229.
- 20). P. R. Somani and S. Radhakrishnan, *Mater. Chem. Phys.*, **2002**, *77*, 117.
- 21). D.J. Barclay, D.H. Martin, Electrochromic displays, in: E.R. Howells (Ed.), *Technology of Chemicals and Materials for Electronics*, p. 266.
- 22). F. Garnier, G. Tourillon, M. Gazard, and J. C. Dubois, *J. Electroanal. Chem.*, **1983**, *148*, 299.

- 23). A. Watanabe, K. Mori, Y. Iwasaki, Y. Nakamura, and S. Niizuma, *Macromolecules*, **1987**, *20*, 1793.
- 24). V. Neburchilov, J. Martin, H. Wang and J. Zhang, *J. Power Sources*, **2007**, *169*, 221.
- 25). J.-P. Randin , *J. Electrochem. Soc.* **1982** , *129* , 1215.
- 26). V. K. Thakur, G. Ding, J. Ma, P. S. Lee and X. Lu, *Adv. Mater.* **2012**, *24*, 4071.

Section 1. Studies on (Carbon-Dots)ⁿ⁻M_n⁺ as a New Type of Supporting Electrolyte for High-Performance Electrochromic Devices

Abstract

A new type of supporting electrolyte based on carbon dots and metal cations was prepared and characterized. The nano-sized carbon dots with high polarizability bear metal counter cation (M_n⁺) such as K⁺, Na⁺, Li⁺ by electrostatic interaction and π-cation interaction due to its polyanionic form and high sp² honeycomb structure. The (carbon-dot)ⁿ⁻M_n⁺ electrolytes showed high thermal (T_d = 655 °C) and chemical stability, high cation number (n⁺ ≥ 24), and ion conductivity. In addition, the (carbon-dot)ⁿ⁻M_n⁺ is nontoxic and environmentally friendly ionic compounds. Based on these characteristics, the physicochemical properties of the (carbon-dot)ⁿ⁻M_n⁺ was studied and investigated for electrochromic devices (ECDs). The ECDs exhibited enhanced electrochromic performance with good cycling life high coloration efficiency (η , 103.0 cm²C⁻¹) and optical density (ΔOD , 0.89).

Keywords: Carbon dot, metal counter cation, supporting electrolyte, ionic compound, electrochromic device

1 Introduction

The interesting of energy saving systems such as secondary ion batteries, electrochromic devices (ECDs), and dye-sensitized solar cells (DSSCs) is increasing due to the environmental problems represented by global warming and energy crisis. Among such electrochemical cells, electrochromic devices (ECDs), such as smart window, car mirrors, and optical display means a smart function that changes color. However the ECDs must be improved in efficiency and reliability in order to be used in practical application.¹⁻³ One of the important factors for enhancing the performance of ECDs is material stability of electrolytes during the electrochemical reactions. Since the ECDs behave like a thin film battery that changes color depending whether electrochromic material (EC) is charged or discharged by electrical current or voltage, the electrolyte in ECDs is to provide counter ions to maintain the electrical neutrality of the EC.⁴ As a result, the electrolyte as an ion conductor is an indispensable component because electrochemical reaction is supported by electrolytes in ECDs. High ionic conductivity of electrolyte facilitates the movement of ions into and out of an EC material to initiate color change. Furthermore, since undesired chemical reactions must not occur during operation of the device, the electrolyte should possess good thermally as well as chemically stable. To solve these issues, various methods have been proposed. For example, incorporation of electrolyte into the electrochromic material has been introduced and new polyelectrolyte or poly electrolyte systems have been developed.⁵⁻⁷ However, the highly dense polymer in electrolyte component decreased color switching properties and coloration efficiency due to the slow ionic and ambipolar conductivity. As a result, both the concentrated and the depleted electrolyte have very low ion conductivity, which cause the

polarization of the ECDs, leading to the degradation the performance of ECDs. Another problem is that their high cost makes them usually unsuitable for their use as the sole electrolyte. Therefore, it is highly essential to explore new electrolyte system with enhanced electrochemical stability and ion conductivity to improve the electrochromic performance.

In this work, we developed a new type of supporting electrolyte. The carbon dots prepared from hydrothermal oxidation of carbon nanofiber precursors have polyanionic forms of oxygen-bearing functional groups on their surface and edge. The carbon dots form ionic compounds with metal counter cations (M_n^+) such as K^+ , Na^+ , and Li^+ via electrostatic interaction and π -cation interaction, resulting in (carbon-dot) $^nM_n^+$ electrolytes. The (carbon-dot) $^nM_n^+$ showed high thermal, electrochemical stability and ion conductivity, which was used as an electrolyte for ECDs. The resulting ECDs exhibit excellent performance electrochromism with fast response time, long lifetime, high coloration efficiency and low power consumption in ECDs, compared to conventional electrolytes such as KCl, K_2CO_3 and K_2SO_4 .

2 Experimental Methods

2.1 Reagents and Materials

All the chemical agents used in this study were commercially available and used without further purification. Carbon nanofiber (precursor), potassium carbonate, Lithium hydroxide, Lithium carbonate and sodium carbonate were purchased from Sigma-Aldrich and SAMCHUN.

2.2 Preparation of (Carbon-dot)ⁿ-M_n⁺

Carbon nanofibers (NEXCARB-H, 0.30 g) were added into a mixture composed of concentrated H₂SO₄ (18 mL) and HNO₃ (6 mL), followed by sonication for 1 h and continuous stirring for 1 day at 120 °C. After cooling and solution containing metal precursors (K₂CO₃ or LiOH) was poured for adjusting the pH 4. The (carbon-dot)ⁿ-M_n⁺ were isolated through size-selective precipitation by centrifugation at 12,000 rpm for 30 min. Ethanol was added into the supernatant solution with a volume ratio of 1:1, and then the solution was centrifuged under the same conditions. This process was repeated three times to obtain uniform-sized (carbon-dot)ⁿ-M_n⁺. The supernatant of (carbon-dot)ⁿ-M_n⁺ solution was further dialyzed and dispersed into DI water, or diethyl carbonate (DEC) solvent for 48 h to remove the excess ions and large size of (carbon-dot)ⁿ-M_n⁺. All reagents and solvents used in this study were commercially available and used without further purification.

2.3 Deposition of Prussian Blue on Indium Tin Oxide (ITO) Electrodes

Prussian blue (PB) thin films on ITO substrate were deposited⁸ by chronoamperometry method in electrochemical cell, which consists of three electrodes (a reference electrode, Ag/Ag⁺ 0.01 M, a counter electrode (Pt) and a working electrode (Pt)) in aqueous solution, containing 0.05 M HCl, 0.05 M K₃Fe(CN)₆, and 0.05 M FeCl₃·6H₂O. The PB thin films were subjected to 3 cycles, 0.72 to 0.77 V at a scan rate of 50 mVs⁻¹ for 300 s. The electrochemical deposition provided PB films with an average film thickness of 320 nm, as calculated from the 6.3 mCcm⁻² charge passed on electrochemically switching colour states. Once the

immobilized PB films on the ITO surface were obtained, they should be rinsed with DI water and kept away from dust and grease.

2.4 Instruments

The electrochemical experiments were performed with a CH instrument (650B electrochemical analyzer) using three electrode system, at room temperature (RT). All potential were reported versus Ag/AgCl reference electrode. Electrochemical impedance spectroscopy (EIS) was performed with 5 mV amplitude in a frequency range from 1 to 100 kHz. Thermal properties of materials were obtained using a thermal gravimetric analyzer (TGA) (TA instruments, Q-5000 IR). The optical properties were characterized by absorption (Beckman, DU650) and photoluminescence (PL) spectra (Jasco, FP-7500 spectrophotometer). Fourier-transform infrared (FT-IR) spectroscopy was conducted using a Nicolet 6700 (Thermo scientific, USA). Functional groups and chemical composition of (carbon-dot)ⁿ-M_n⁺ were analysed by x-ray photoelectron spectroscopy (XPS) (Kratos, AXIS Supra) using a monochromatic AlK α (15 kV, 375 W). Raman spectroscopy was conducted using Labram aramis (Horiba) with 514 nm Ar-ion laser. HRTEM (JEOL, KEO-2100) and HAADF-STEM (FEI, Technai F20) were performed at 200 kV for acquisition of carbon dots images. The electrochromic properties including coloration/bleaching, optical density and coloration efficiency were measured by transmittance variation at a wavelength of 700 nm with alternately applied potential of -0.16 and 0.4 V, 50% duty cycle for 10 s in each state.

3 Results and Discussion

The prepared (carbon-dot)ⁿM_n⁺ (M⁺ means metal counter cation such as K⁺, Na⁺ or Li⁺) was stably formed white-yellow suspensions in aqueous solution as well as organic solvents such as ethanol (EtOH), isopropyl alcohol (IPA), and diethyl carbonate (DEC). The UV/vis spectra exhibited two peaks at the (carbon-dot)ⁿLi_n⁺ dispersed in aqueous solution as well as in DEC/EC (1:1 v/v) mixture solvent shown in **Fig. 1**. The absorption peak at 269 nm would originate from π - π^* transition in the sp² carbon atoms of carbon-dots. The absorption peak at 347 nm can be ascribed to the n- π^* transitions presence of oxygen atom at the edge site of carbon dots involved in C=O or C-O groups.⁹⁻¹² Although photoluminescence (PL) intensity was reduced, the excitation-dependent photoluminescence (PL) emission spectra were observed from blue to red-shifted with decreasing excitation energy shown in **Fig. 1(a)**. The blue PL emission at 420 nm would originate from quantum confinement effect of carbon dots. On the other hands, the green emission bands at 520 nm arise from edge effect of oxygen functional groups.¹² Although no difference in absorption spectra was observed, the broad and red-shifted PL spectra of (carbon-dot)ⁿLi_n⁺ emerged in aqueous solution, compared to in DEC/EC mixture solvent as shown **Fig. 1**. This result is in good agreement with the TEM image that showed aggregated (carbon-dots)ⁿLi_n⁺ with mostly below 50 nm in aqueous solution shown **Fig. 2(b)**. This is because strong interaction such as electrostatic attraction, and/or π -cation interaction between these oxygen functional groups and metal cations in aqueous solution.^{11,13,14} (These interactions is described in more detail later) On the other hand, well-dispersed and uniformly sized carbon dots were observed in organic solvent in **Fig. 2(a)**. These results implied that there might be a correlation between the evolution of the PL spectra and the size effect of (carbon-dots)ⁿM_n⁺.

X-ray photoelectron spectroscopy (XPS) was performed to determine the composition of the (carbon-dot)ⁿM_n⁺ electrolytes. In **Fig 3(d, e, f)** shows the C 1s

spectra of (carbon-dot)ⁿM_n⁺. All (carbon-dot)ⁿM_n⁺ show that the peak at 284.5 eV was from sp² domain of carbon dots surface. The oxygen species of carbon dots were observed that sp³ carbon including C–O at 285.5 eV, and O–C=O at 288.3 eV.¹⁵⁻¹⁷ The K, Na or Li 2p spectrum of the (carbon-dots)ⁿM_n⁺ was also observed. These results means that metal cations were induced to the anion-bearing carbon dots.

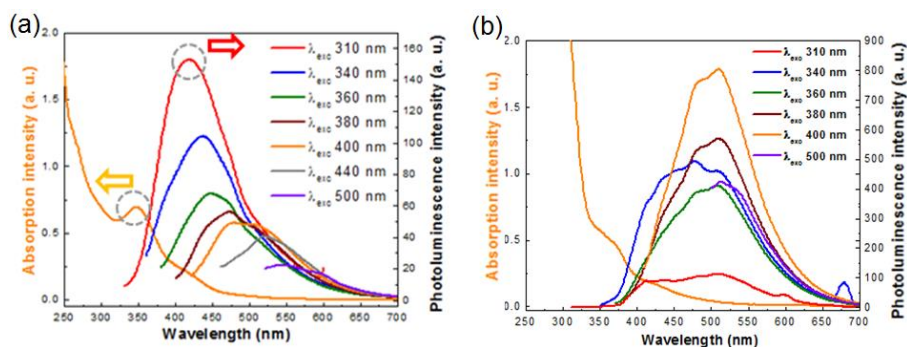


Fig. 1. UV-vis and PLE spectra of (a) (carbon-dot)ⁿLi_n⁺ (0.2 mg/ml in an DEC/EC mixture (1:1 v/v), and (b) (carbon-dot)ⁿLi_n⁺ (0.2 mg/ml in an aqueous solution)

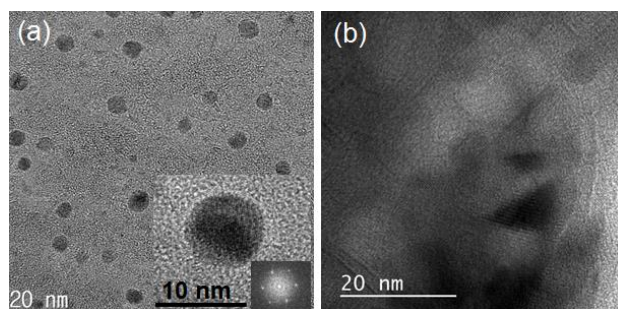


Fig. 2. TEM image of (a) (carbon-dot)ⁿLi_n⁺ (0.2 mg/ml in an DEC/EC mixture (1:1 v/v), and (b) (carbon-dot)ⁿLi_n⁺ (0.2 mg/ml in an aqueous solution) (inserted image: High resolution TEM image of (carbon-dot)ⁿLi_n⁺ and corresponding 2D FFT image)

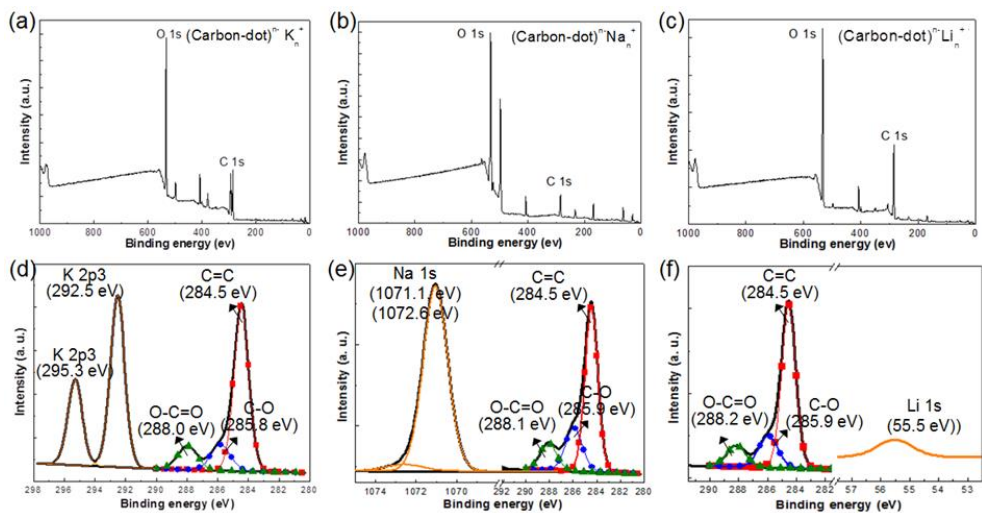


Fig. 3. The XPS C1s spectra of (a) (carbon-dot)ⁿK_n⁺, (b) (carbon-dot)ⁿNa_n⁺, (c) (carbon-dot)ⁿLi_n⁺, and metal cation spectra of (d) (carbon-dot)ⁿK_n⁺, (e) (carbon-dot)ⁿNa_n⁺, and (f) (carbon-dot)ⁿLi_n⁺.

On the other hands, no XPS spectra from metal cations were observed in sample only carbon dots (not shown data). Fourier transform infrared (FT-IR) of all the (carbon-dot)ⁿM_n⁺ samples also revealed C=C structures and various oxygen groups of carbon dots, including a broad O-H stretching of hydroxyl and carboxylic groups around 3450 cm⁻¹, C=O stretching of carboxyl groups around 1760 cm⁻¹, aromatic stretching (C=C) of carbon peak at 1640 cm⁻¹, C-O stretching of carboxyl groups and C-H bending around 1340 cm⁻¹, and C-O stretching of epoxy deformation on the basal plane around 1300 and 1080 cm⁻¹ as shown **Fig.4**.^{16,17} These results implied that oxygen functionalization takes place at the edge site of carbon dots due to the unzipping mechanism related to the oxidative break process converted from epoxy pairs to carbonyl pairs.¹⁸

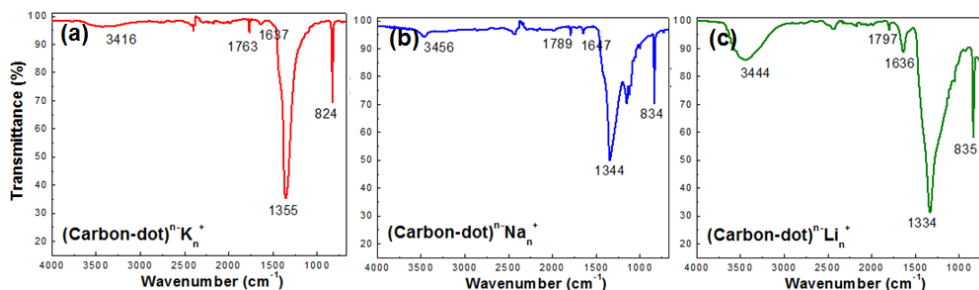


Fig. 4. FT-IR spectra of (a) $(\text{carbon-dot})^n\text{K}_n^+$, (b) $(\text{carbon-dot})^n\text{Na}_n^+$, and (c) $(\text{carbon-dot})^n\text{Li}_n^+$

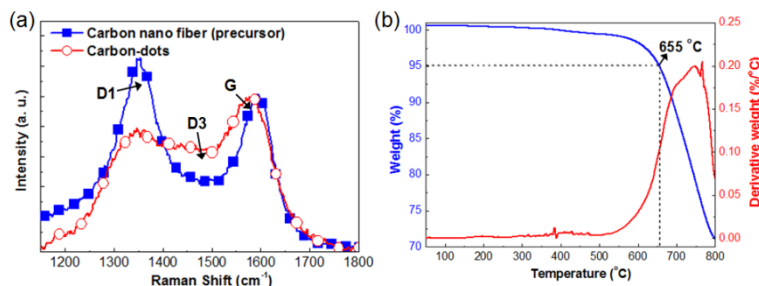


Fig. 5. (a) Raman spectra of HNF (closed rectangle), $(\text{carbon-dot})^n\text{Li}_n^+$ (open circle), and (b) TGA data of $(\text{carbon-dots})^n\text{Li}_n^+$

Raman spectroscopy data of carbon nanofiber (CNFs) precursors and $(\text{carbon-dot})\text{Li}_x^+$ were investigated as shown **Fig. 5(a)**. Two samples show multiple Raman band, relating to the characteristic modes of graphite such as D and G bands. The G band is from the vibrations of sp^2 carbon (E_{2g} mode), while the D1 and D3 band are related to the disordered graphitic lattice and oxygen functional groups, respectively.^{19,20} CNFs show a crystalline G band at 1593 cm^{-1} and a disordered D band at 1354 cm^{-1} . In case of the carbon dots, the G and D bands were found at 1576 cm^{-1} and 1348 cm^{-1} , respectively. The peaks were broadened compared to CNFs, and the relative intensity of the G band is enhanced as compared to that of the D band. The red shift of Raman spectrum could be

attributed to the metal cations on edge of carbon dots. These results including UV/vis, PL, XPS, FT-IR and Raman spectra indicated that a number of several types oxygen-containing functional groups as C–O, C=O, and O–C=O were decorated on the edge carbon dots. As a result, metal cations were induced by interaction between carbon dots and metal cations, such as electrostatic interaction and/or π -cation interaction.²¹⁻²³ The (carbon-dot)ⁿM_n⁺ electrolytes must be thermally stable, as they can be decomposed due to heat generated during redox reaction in electrochemical cells. Therefore, (carbon-dot)ⁿLi_n⁺ was examined by thermal gravimetric analyzer (TGA). The resulting data exhibited higher thermal stability in **Fig. 5(b)**. This result implies that the sp² structure of carbon dots can contribute to the thermal stability and would suppress its degradation.

To further investigate the properties of (carbon-dot)ⁿM_n⁺ as a supporting electrolyte in ECDs, the morphologies and thicknesses of prussian blue (PB, KFe^{III}[Fe^{II}(CN)₆]) thin films as a EC material, prepared by electrochemical deposition method²⁴ were investigated by a scanning electron microscope (SEM), as shown in **Fig. 6(a)** and **(b)**. The UV-vis spectra of the PB thin films display a broaden absorption band around 700 nm with increasing the electrical deposition time of PB on ITO surface.^{25,26} **Fig. 6(c)** showed the optical transmittance value as a function of the deposition time. The absorbance at 700 nm was linearly rise with the increasing number of electrical deposition cycles. These results implied a uniform film deposition growth.

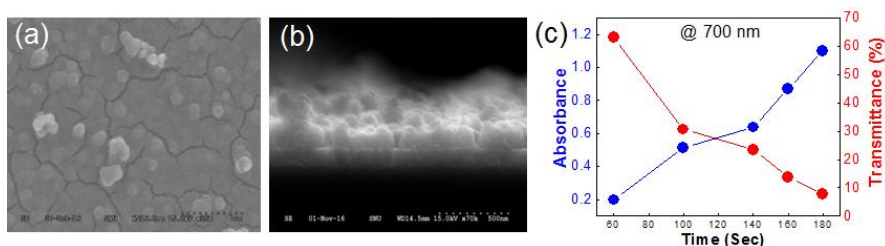
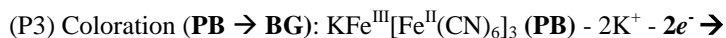
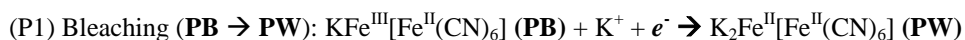


Fig. 6. (a) SEM image of PB thin films electrodeposited at 40 uA for 140 s obtained from (a) plan-view, (b) cross-sectional view, and (c) absorbance and optical transmittance spectra of PB thin films as a function of electrodeposition time

To investigate electrochemical behavior of optimized PB thin films (40 uA, 140 s) according to electrolyte type such as (carbon-dot)ⁿM_n⁺, KCl, K₂CO₃, and K₂SO₄, cyclic voltammetry (CV) was performed using a three-electrode system, consisting of working electrode (PB thin film), counter electrode (Pt) and reference electrode (Ag/AgCl). The color change of PB thin films occurs upon the intercalation/deintercalation of counter cations into the lattice channel of PB structure by applied voltage or current. The redox reactions in PB thin film by ion diffusion can be expressed as;²⁷⁻²⁹



The electrochemical reaction of PB thin films showed three redox reactions regardless of electrolyte species as shown in **Fig. 7**. The results were listed in **Table 1**. An interesting observation is that different redox behaviors were observed in PB thin films depending on the type of electrolytes used. This is because the transport of alkali cations such as K⁺, Na⁺, and Li⁺ dominates the redox reaction of the PB thin film, and charge transfer reaction between the PB thin film and alkali cations is limited by the channel radius of the PB structure. When (carbon-dot)ⁿNa_n⁺, (carbon-dot)ⁿLi_n⁺, and KCl were used, cyclic voltammogram (CV) showed relatively slow and irreversible redox reaction, resulting in large peak-to-peak separation (ΔE_{pp}). This is probably due to other side reaction occurred by higher voltage of redox reaction. It should be noted that this may cause problems in the stability of PB thin film. According to electrochemical studies, although the current order is KCl > (carbon-dot)ⁿK_n⁺ > K₂CO₃ > K₂SO₄ > (carbon-dot)ⁿNa_n⁺ >

(carbon-dot)ⁿLi_n⁺ for the redox reaction of the PB thin film, (carbon-dot)ⁿK_n⁺ showed the better electrochemical properties than others materials. Therefore, it is expected that the superior electrochromic performance will be observed when using (carbon-dot)ⁿK_n⁺ in ECDs.

To further study the redox reaction kinetic of PB thin films upon electrolyte types, electrochemical impedance spectroscopy (EIS) was performed. There are two types of redox reactions that occur in an electrochromic process. One is charge transfer at the PB material/electrolyte interface and another is a diffusion controlled redox reaction within the lattices of PB material. Since the rate-determining steps of metal cations intercalation and deintercalation are diffusion-controlled, both the response time of color changing from PW to PB and coloration efficiency of ECDs are controlled by the ion conductivity of electrolyte.

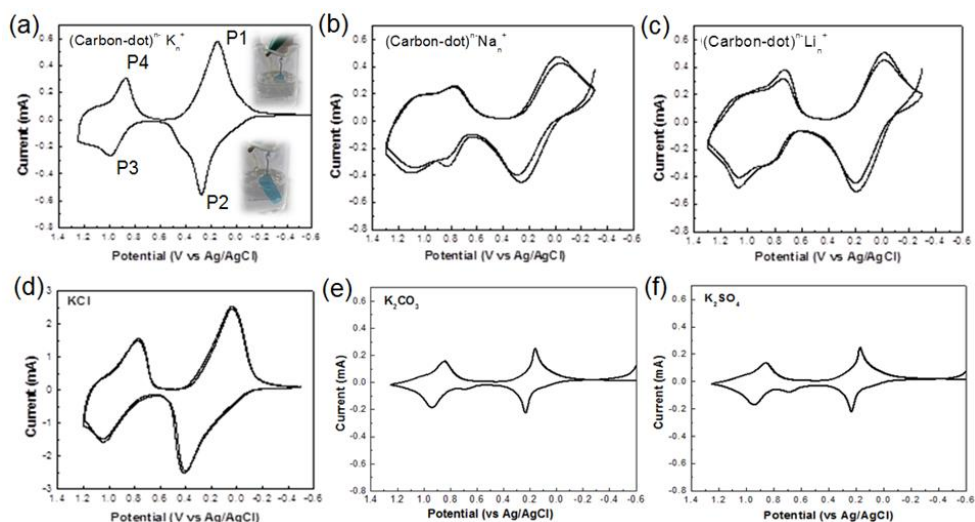


Fig. 7. Cyclic voltammety of PB thin film in 0.5 M (a) (carbon-dots)ⁿK_n⁺, (b) (carbon-dots)ⁿNa_n⁺, and (c) (carbon-dots)ⁿLi_n⁺, (d) KCl, (e) K₂CO₃, and (f) K₂SO₄ solution as a supporting electrolyte at a scan rate of 20 mVs⁻¹ (Ag/AgCl: reference electrode, Pt: counter electrode, and PB film: working electrode), (inserted image: coloration/bleaching state of PB thin film)

Table 1. Electrochemical data of PB thin films^a

Materials	electrochemical redox process					
	E_{re}^o (V)	i_{pc} (mA)	E_{ox}^o (V)	i_{pa} (mA)	ΔE_{pp} (V)	i_{pa}/i_{pc}
KCl	0.041	0.89	0.408	0.35	0.36	0.39
K ₂ CO ₃	0.160	0.23	0.233	0.17	0.073	0.74
K ₂ SO ₄	0.170	0.21	0.233	0.16	0.063	0.76
(carbon-dot) ⁿ⁻ K _n ⁺	0.149	0.30	0.274	0.27	0.125	0.90
(carbon-dot) ⁿ⁻ Na _n ⁺	-0.019	0.15	0.256	0.14	0.275	0.93
(carbon-dot) ⁿ⁻ Li _n ⁺	-0.011	0.06	0.193	0.17	0.204	2.83

^a All electrochemical data were measured at RT. All potentials were calibrated using the Ag/AgCl reference electrode.

Table 2. Diffusion coefficient of metal cations and EIS data using various electrolytes^a

		(C-dot) ⁿ⁻ K _n ⁺	(C-dot) ⁿ⁻ Na _n ⁺	(C-dot) ⁿ⁻ Li _n ⁺	KCl	K ₂ CO ₃	K ₂ SO ₄
D^o (cm ² /s)	PB → PW	9.8×10^{-10}	2.0×10^{-10}	1.8×10^{-12}	2.7×10^{-10}	1.0×10^{-9}	1.6×10^{-9}
	PW → PB	2.2×10^{-10}	6.8×10^{-10}	3.4×10^{-11}	7.8×10^{-10}	2.4×10^{-10}	4.1×10^{-10}
PB → PW (intercalation)	R_s (W)	34	45	71	34	83	82
	R_{ct} (W)	52	285	359	62	47	31
PW → PB (deintercalation)	R_s (W)	35	46	72	33	84	82
	R_{ct} (W)	53	1585	4949	80	214	89

^a All electrochemical data were measured at RT.

In case of (carbon-dot)ⁿM_n⁺, the carbon dot anions were too bulky to be movable, while metal counter cations can be movable easily when electric field is generated in electrochemical cell. As expected, different impedance characteristics were observed in **Fig. 8**. Nyquist plots of PB thin films exhibited a similar series resistance value, relating to the electric resistance of the electrolytes in **Table 2**. However, there were different results of semicircle at a high frequency region, considering to the charge transfer resistance (R_{ct}) which means coloration/bleaching of PB thin film. The order of R_{ct} is (carbon-dot)ⁿK_n⁺ > K₂SO₄ \cong KCl > K₂CO₃ > (carbon-dot)ⁿNa_n⁺ > (carbon-dot)ⁿLi_n⁺. This is because the hydrated radius of Na⁺ (1.83 Å) and Li⁺ (2.37 Å) are larger than that of the channel radius of PB structure.^{30,31} On the other hand, K⁺ ions (1.25 Å) with a small hydration radius can move easily in and out of the channel radius of PB. The slope of the straight line in lower frequency region means the mass transfer of cations toward the PB thin film from the electrolyte solution. The diffusion resistance of K⁺ cation was relatively low compared to Na⁺ and Li⁺ cations. Thus (carbon-dots)ⁿK_n⁺ caused a high electrochemical current value (i_{pa} & i_{pc}) (see CV data in Fig 8).^{25,32,33} The electrochemical studies including CV and EIS have shown that (carbon-dots)ⁿK_n⁺ was a suitable material as a supporting electrolyte.

For the demonstration of practical application of (carbon-dot)ⁿM_n⁺ in ECDs, the electrochromic behavior of PB thin films was explored as a function of the electrolyte types in three electrode system. Electrochromic (EC) behaviors of PB thin films exhibited bleaching state at a bias of -0.16 V, resulting from P1 reaction. Thus, K⁺ ions migrated into the lattice channel of reduced PB to maintain electroneutrality of the PB thin film.^{25,29} After changing the applied voltage to 0.4 V, the PW films returned to the coloration state (PB), corresponding to the P2 reaction. It is obvious that PB was also oxidized with the K⁺ ions flowing out the lattice channel of PB structure. The EC characteristics such as optical density (OD), coloration efficiency (η), switching time, and cycling life were obtained by the chronoamperometry method under switched voltage alternate biases at -0.16 and

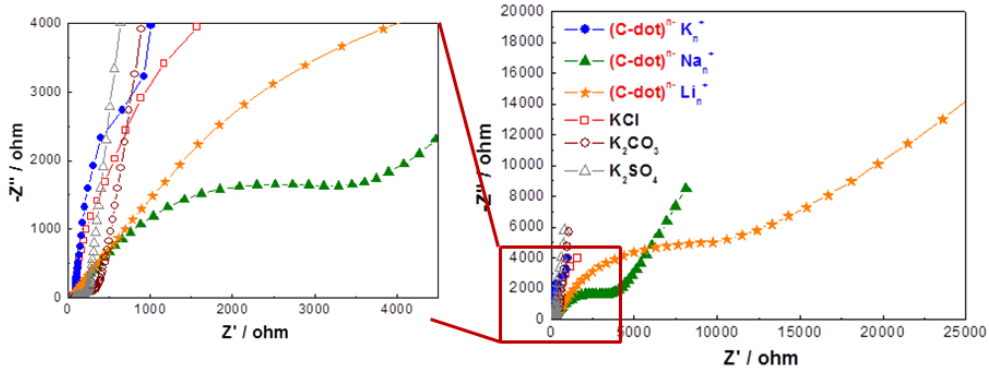


Fig. 8. Electrochemical impedance spectra (EIS) of PB thin films under ac amplitude of 5 mV as function of electrolytes (The concentration of the electrolytes used was 0.5 M).

0.4 V for 10 s each. The obtained parameters of ECDs properties in the presence of same concentration (0.5 M (carbon-dots)ⁿK_n⁺, (carbon-dots)ⁿNa_n⁺, (carbon-dots)ⁿLi_n⁺, KCl, K₂CO₃, and K₂SO₄, respectively) were presented in **Table 3**. The major parameter η in electrochromic process depended on charge transfer between PB thin film and electrolyte and redox reaction determined by the diffusion of counter ions within PB thin films. The η (cm²/C) is defined as the change in the ΔOD to injected or ejected charge density (Q) and is represented;

$$\eta(\lambda) = \frac{\Delta OD}{\Delta Q} = \frac{\log\left(\frac{T_b}{T_c}\right)}{\Delta Q} \quad (1)$$

where T_c , T_b are transmittance of the coloring state and of the bleaching state, respectively. The characteristics of ECDs varied depending on the type of electrolytes used. When using (carbon-dot)ⁿK_n⁺ in ECDs, all parameter values were better than that of other electrolytes. The η and ΔOD based on (carbon-dot)ⁿK_n⁺ were measured to be 103.0 cm²C⁻¹ and 0.89, respectively. The η is a key parameter for ECDs, meaning that high η can provide a large optical modulation

with low charge insertion or extraction. Moreover, cycle life related to the number of the color switching exhibited slightly degradation with 73% (ΔT) after 1,000 switching cycles in **Fig. 9**. These results reveal that (carbon-dot)ⁿK_n⁺ are enough to perform supporting electrolyte, leading to stable switching behavior of PB thin films. In contrast, the η and ΔOD of PB thin film using KCl (and K₂CO₃) electrolyte were 81.6 (88.7) cm²C⁻¹ and 0.71 (0.76), respectively and subsequently deteriorated with switching cycles. Consequently, electrochromism of PB thin film was not observed after 200 switching cycles. This is probably that Cl⁻ anions attack or adsorbed the surface of PB thin film and low transference number of K⁺ cation cause the degradation of PB thin film.³⁴ The carbon dot anions with large size were slow to diffuse, thus (carbon-dot)ⁿK_n⁺ serves as single ion conductors, resulting in close to 1.0 of K⁺ cation transference number. This is one of the most important characteristics for electrochemical applications. As a result, (carbon-dot)ⁿK_n⁺ facilitated redox reaction of PB thin film and achieved fast response time, long lifetime, high coloration efficiency and low power consumption of PB thin film compared to commercial electrolytes.

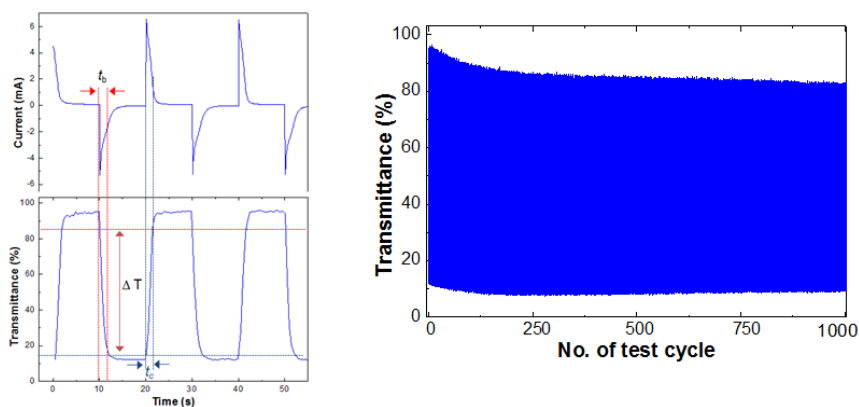


Fig. 9. (a) Chronoamperometry curve and the corresponding in situ optical transmittance change, and (b) optical transmittance as a function of operation cycles at 700 nm

Table 3. Electrochemical data of PB thin films^a

Materials	ΔOD ($\log(T_b/T_c)$)	η (cm ² /C) ($\Delta OD/\Delta Q$)	τ_b (s)	τ_c (s)	ΔT_{200} (%)	ΔT_{300} (%)	ΔT_{1000} (%)
KCl	0.71	81.6	1.9	3.0	66	x	x
K ₂ CO ₃	0.76	88.7	1.5	2.0	22	x	x
K ₂ SO ₄	0.96	150.6	5.6	6.0	52	52	52
(Carbon-dot) ⁿ -K _n ⁺	0.89	103.0	1.5	2.1	75	75	73
(Carbon-dot) ⁿ -Na _n ⁺	0.71	84.0	1.6	2.8	84	39	x
(Carbon-dot) ⁿ -Li _n ⁺	0.52	78.7	2.4	2.6	57	x	x

^a All electrochemical data were measured at RT. Three electrodes system was used (PB thin film: working electrode, Pt: counter electrode, and Ag/AgCl: reference electrode). Transmittance values were measured at 700 nm. The color switching time is defined as the time to reach 90 and 10% of the final color changing state in transmittance between the steady PB and PW states, respectively

4 Conclusion

In conclusion, we successfully demonstrated a new type of (carbon-dot)ⁿ-M_n⁺ as a supporting electrolyte. The (carbon-dot)ⁿ-M_n⁺ were formed because of the electrostatic interaction and π -cation interaction between carbon dots and metal counter cations. The structural, physical and electrochemical studies of (carbon-dot)ⁿ-M_n⁺ exhibit high thermal, electrochemical stability and ion conductivity. The ECDs using (carbon-dot)ⁿ-K_n⁺ show improved electrochromic performance, relating with high color efficiency (103.0 cm²C⁻¹), optical density (0.89) and long-term cycling life, compared with commercial electrolytes such as KCl, K₂CO₃, and K₂SO₄. These results suggest that (carbon-dot)ⁿ-M_n⁺ exhibit promising prospective

application in electrochemical cells, including secondary ion battery, supercapacitor, and electrochemical transistor.

5 References and Notes

- 1). P. Monk , R. Mortimer , D. Rosseinsky , *Electrochromism and Electrochromic Devices* , Cambridge University Press , Cambridge, UK **2007**
- 2). K. Wang, H. Wu, Y. Meng. Y. Zhang and Z. Wei, *Energy Environ. Sci.*, **2012**, *5*, 8384.
- 3). A. Michaelis, H. Berneth, D. Haarer, S. Kostromine, R. Neigl and R. Schmidt, *Adv. Mater.*, **2001**, *13*, 1825.
- 4). J. Wang, L. Zhang, L. Yu, Z. Jiao, H. Xie, X. W. Lou and X. W. Sun, *Nat. Commun.*, **2014**, *5*, 4921.
- 5). E. Hwang, S. Seo, S. Bak, H. Lee, M. Lee and H. Lee, *Adv. Mater.*, **2014**, *26*, 5129.
- 6). H. C. Moon, T. P. Lodge and C. D. Frisbie, *Chem. Mater.*, **2015**, *27*, 1420.
- 7). A. M. Stephan and K. S. Nahm, *Polymer*, **2006**, *47*, 5952.
- 8). L. M. N. Assis, L. Ponez, A. Januszko, K. Grudzinski and A. Pawlicka, *Electrochim. Acta*, **2013**, *111*, 299.
- 9). D. Pan, J. Zhang, Z. Li and M. Wu, *Adv. Mater.* **2010**, *22*, 734.
- 10). B. Mohamed, D. Jingjing, Z. Austin, R. Chloe and F. de C. Maria, *J. Environ. Sci.*, **2018**, *65*, 223.

- 11). S. Chen, J.-W. Liu, M.-L. Chen, X.-W. Chen and J.-H. Wang, *Chem. Commun.*, **2012**, 48, 7637.
- 12). K. Lingam, R. Podila, H. Qian, S. Serkiz and A. M. Rao, *Adv. Funct. Mater.* **2013**, 23, 5062.
- 13). P. Sun, M. Zhu, K. Wang, M. Zhong, J. Wei, D. Wu, Z. Xu and H. Zhu, *ACS Nano*, **2013**, 7, 428.
- 14). P. Sun, F. Zheng, M. Zhu, Z. Song, K. Wang, M. Zhong, D. Wu, R. B. Little, Z. Xu and H. Zhu, *ACS Nano*, **2014**, 8, 850.
- 15). C.-a. Tao, J. Wang, S. Qin, Y. Lv, Y. Long, H. Zhu and Z. Jiang, *J. Mater. Chem.*, **2012**, 22, 24856.
- 16). P. Juan, G. Wei, K. G. Bipin, L. Zheng, R.-A. Rebeca, G. Liehui, S. Li, B. A. Lawrence, Z. Xiaobo, G. Guanhuai, A. V. Sajna, A. K. Benny, A. M. Angel, H. Takuya, J.-J. Zhu and M. A. Pulickel, *Nano Lett.*, **2012**, 12, 844.10).
- 17). M. Samal, N. Barange, D.-H. Ko and K. Yun, *J. Phys. Chem. C*, **2015**, 119, 19619.
- 18). L. Zhenyu, Z. Wenhua, L. Yi, Y. Jinlong and G. H. Jian, *J. Am. Chem. Soc.*, **2009**, 131, 6320.
- 19). Z. Zainab, H. N. Zhen, W. Xing, X. S. Zhi, Y. N. Hai, B. Jing and T. S. Li, *Carbon*, **2013**, 61, 57.
- 20). A. C. Ferrari,¹ J. C. Meyer, V. Scardaci, C. Casiraghi, M. Lazzeri, F. Mauri, S. Piscanec, D. Jiang, K. S. Novoselov, S. Roth and A. K. Geim, *Phys Rev Lett.*, **2006**, 97, 187401.
- 21). F. Wan, H. Shi, W. Chen, Z. Gu, L. Du, P. Wang, J. Wang and Y. Huang, *Nanomaterials*, **2017**, 7, 210.
- 22). S. Zhang, Y. Li, H. Song, X. Chen, J. Zhou, S. Hong and M. Huang, *Sci. Rep.*, **2015**, 6, 19292

- 23). G. Rajender and P. K. Giri, *J. Mater. Chem. C*, **2016**, *4*, 10852.
- 24). J. J. Garcia-Jareno, D. Benito, J. Navarro-Laboulais and F. Vicente, *J. Chem. Ed.*, **1998**, *75*, 881.
- 25). X. Liu, A. Zhou, Y. Dou, T. Pan, M. Shao, J. Han and M. Wei, *Nanoscale*, **2015**, *7*, 17088.
- 26). H.-C. Lu, S.-Y. Kao, T.-H. Chang, C.-W. Kung and K.-C. Ho, *Sol. Energy Mater. Sol. Cells*, **2016**, *147*, 75.
- 27). K. Itaya, T. Ataka and S. Toshima, *J. Am. Chem. Soc.*, **1982**, *104*, 4767.
- 28). C. Gervais, M.-A. Languille, S. Réguer, M. Gillet, S. Pelletier, C. Garnier, E. P. Vicenzi and L. Bertrand, *J. Anal. At. Spectrom.*, **2013**, *28*, 1600.
- 29). R. Yan, L. Liu, H. Zhao, Y. G. Zhu, C. Jia, M. Han and Q. Wang, *J. Mater. Chem. C*, **2016**, *4*, 8997.
- 30). J. J. Garcia-Jareño, D. Gimenez-Romero, F. Vicente, C. Gabrielli, M. Keddad and H. Perrot, *J. Phys. Chem. B*, **2003**, *107*, 11321.
- 31). M. H. Pournaghi-Azar and H. Dastangoo, *J. Electroanal. Chem.*, **2004**, *573*, 355.
- 32). C. H. Li, Y. Nanba, D. Asakura, M. Okubo and D. R. Talham, *RSC Adv.*, **2014**, *4*, 24955.
- 33). R. Saliba, B. Agricole, C. Mingotaud and S. Ravaine, *J. Phys. Chem. B*, **1999**, *103*, 9712.
- 34). A. Roig, J. Navarro, R. Tamarit and F. Vicente, *J. Electroanal. Chem.*, **1993**, *360*, 55.

국문초록

유기 반도체는 다양한 구조, 저렴한 제조공정 비용 그리고 독특한 물리적 성질로 인해 지난 수십년 동안 큰 주목을 받고 있다. 유기 반도체는 유기태양전지 (OPV), 유기광검출기 (OPD), 유기발광다이오드 (OLED), 전기변색소자 (ECD), 그리고 이차이온전지 등과 같은 (광학)전자 기기에 사용되고 있다. 특히, 파이-콘주게이션된 단분자 들은 에너지 수확과 관련하여 상당한 주목을 받고 있다. 이는 지구 온난화와 에너지 위기로 인한 환경 문제로 인해 에너지 절약 시스템에 대한 관심이 증가되고 있기 때문이다. 또한 분자 구조 변화를 통해 광물리 및 전기적 특성을 제어 할 수 있는 독특한 특성을 가지고 있기 때문이다. 본 연구에서는 전자 주계 물질로서 푸시-풀 구조 단분자와 나노복합체 특성을 기반으로 유기태양전지 및 유기광검출기와 같은 유기 광전지 효율을 향상시키는 다양한 방법을 고찰하였다. 그리고 새로운 유형의 이온 전도체인 탄소 양자점-금속 양이온 화합물을 이용하여 전기변색소자의 에너지 수확에 대해 논의하였다.

1 장에서는 유기 반도체 및 유기광전지에 대한 특징을 간략히 요약하였다. 광 흡수 및 방출과 관련된 전자 전이와 여기자 (운반체)의 생성 및 수송을 위한 메커니즘이 설명되었다. 유기 반도체의 이러한 특성을 이해하는 것은 무기 반도체와는 다른 특성을 구별하는데 필수적이다. 마지막으로 유기태양전지 및 유기광검출기 특성 및 개발에 대한 개요를 기술하였다. 이 내용은 유기광전지 작동 원리를 포함하며, 지금까지 개발된 전자 주계용 단분자와 소자 구조에 대해 요약되었다.

2 장에서는 푸시-풀 구조 단분자, 탄소 양자점@PEDOT:PSS 그리고 콜로이드 양자점-실리카 복합체 특성과 이를 사용한 유기태양전지 특성에 대해 고찰하였다. 첫번째 부분에서는 전자 주게 물질로서 푸시-풀 구조 단분자에서 파이-연결체가 전기화학적, 열적 그리고 형태학적 특성과 유기태양전지 성능에 미치는 연구를 수행하였다. 트라이싸이오펜 파이-연결체를 갖는 **3T** 는 보다 빠른 전극 반응 속도와 높은 전기화학적 안정성을 보였다. **3T:PC₇₁BM** 광활성층을 기반으로 하는 용액공정방법으로 제작된 벌크 이종접합 유기태양전지는 **3T** 의 우수한 전기화학적 특성으로 인해 다이싸이엔오싸이오펜 기반 유기태양전지보다 높은 광-전류 전환효율을 보여주었다. 이러한 결과는 고효율 유기태양전지를 구현하기 위해서는 푸시-풀 구조체에 있어 파이-연결체 특성이 고려되어야 한다는 것을 의미한다. 두번째 부분에서는 3 개의 푸시-풀 구조 단분자를 전자 주게 물질로 제시하고 이를 이용한 유기광검출기 특성에 대해 고찰하였다. 단분자에서 파이-연결체는 광물리, 열적 그리고 형태학적 특성에 영향을 미쳤다. 이러한 분자 특성에 기반한 유기광검출기 성능을 체계적으로 연구하였다. 박막 상태에서, 다른 분자보다 분자간 상호 작용이 적고 파이-파이 패킹 밀도가 낮은 **H3** 분자가 이종접합 뿐만 아니라 벌크 이종접합을 갖는 소자에서 보다 높은 감도 및 광대역 외부 양자 효율을 보여 주었다. 이 연구결과는 푸시-풀 구조체에 있어 파이-연결체 구조가 박막상에서 분자의 결정성에 영향을 줄 수 있으며, 비정질 도메인을 갖는 광활성층 구조가 다결정 도메인 시스템에 비해 유기광검출기에서 더 높은 성능을 유도 할 수 있음을 시사한다. 그리고 더 나아가, 효과적인 전자 주게용 분자 설계와 고성능

유기광검출기를 달성하기 위해 암전류 밀도를 감소시키는 방법에 대해 도움을 주리라 기대한다. *세번째* 부분에서는 유기태양전지에서 정공 수송층을 위한 광 가교 올리고싸이오펜 (5T-p)에 대해 고찰하였다. 스핀 캐스팅 방법에 의해 제조된 5T-p 박막은 254 nm 자외선 조사에 의해 광중합 되었다. 이 결과로 박막의 특성화는 박막 내의 적절한 분자간 패킹 네트워크가 유기태양전지 성능에 유의미한 영향을 미친다는 것을 확인하였다. *네번째* 부분에서는 탄소양자점@PEDOT:PSS 나노 복합체의 자기 조립체에 대해 고찰하였다. 탄소 양자점은 정전기적 상호 작용을 통해 PEDOT 사슬 사이의 물리적인 연결체 역할을 하며, 코어-셸 나노 구조를 형성하였다. 이 나노 구조는 서로 연결되어 최종적으로 유기 겔화 되었다. 따라서, 탄소 양자점은 PEDOT 사슬의 재배향과 박막내 PEDOT 도메인의 상호 연결성에 영향을 주어 박막의 전기 전도도를 향상시켰다. 탄소 양자점이 첨가된 PEDOT:PSS 박막을 P3HT:PC₆₁BM 활성층 기반 벌크 이종접합 유기태양전지의 정공 수송층으로 응용하여 광-전류 전환효율을 26% 상승시켰다. *다섯번째* 부분에서는 콜로이드 양자점-실리카 복합체를 발광 하향 변환 물질로 사용한 유기태양전지의 광 수확 향상에 대해 고찰하였다. 양자점은 응집 및 상 분리 없이 실리카 매트릭스에 균일하게 분산되었다. 발광 하향 변환 층은 가시광선의 입사광 투과율 향상과 자외선 영역의 광 수확을 증가시켜 유기태양전지의 광-전류 전환효율을 8.9% 상승시켰다.

3 장에서는 전기변색소자의 에너지 수확 시스템에 관하여 고찰하였다. 이를 위해서, 전기변색소자 특성 및 전기변색물질 개발에 대한 개략적인

설명을 요약하였다. 이러한 내용은 색 변화 메커니즘을 이해하고 더 나아가 새로운 전기변색물질 및 전해질을 고안하는데 도움이 될 것이다. *첫번째 부분*에서는 탄소 양자점을 기반으로 한 새로운 유형의 지지 전해질 특성과 이를 응용한 전기변색소자 성능에 대해 고찰하였다. 높은 분극력을 지닌 나노 크기의 탄소 양자점은 정전기적 상호 작용과 파이-양이온 상호 작용에 의해 금속 상대 양이온과 이온 화합물을 형성하였다. 탄소 양자점-금속 양이온 화합물에 대해 다양한 분석방법을 이용하여 특성을 평가하였다. 탄소 양자점-금속 양이온 전해질은 높은 열적 ($T_d = 655\text{ }^\circ\text{C}$), 화학적 안정성, 높은 양이온 수 ($n \geq 24$), 그리고 높은 이온 전도도 특성을 보였다. 또한 독성이 없고 환경친화적인 이온 화합물이다. 탄소 양자점-금속 양이온 화합물을 전해질로 사용한 전기변색소자는 향상된 변색효율 (η , $103.0\text{ cm}^2\text{C}^{-1}$)과 광학밀도 (ΔOD , 0.89) 그리고 소자 안정성이 개선되었다. 이러한 연구결과는 탄소 양자점-금속 양이온 화합물이 이차이온전지, 슈퍼캐패시터 및 전기화학 트랜지스터와 같은 전기화학셀에 적합한 전해질로 사용될 수 있음을 의미한다.

주요단어: 유기 반도체, 푸쉬-풀형 유기 단분자, 파이-연결체, 탄소 양자점, 나노복합체, 지지 전해질, 에너지 수확, 유기태양전지, 유기광검출기, 전기변색소자

학번: 2012-30879